Master's thesis in physics

Resonant Slepton Production in the Two Muon + Jets Final State at $\sqrt{s} = 8\,\text{TeV}$

Written by

Markus Radziej

Submitted to the
Faculty of Mathematics, Computer Science and Natural Sciences

Created at the
III. Phys. Inst. A

of the
RWTH Aachen university

Supervised by
Prof. Dr. Thomas Hebbeker

Second reviewer
Prof. Dr. Christopher Wiebusch

April 7, 2014

I assure that I have created this document independently, have not used any sources or aids other than the ones I have listed and have labeled quotes as such.

Aachen the Signature

Abstract

Presented is the search for resonant production of second generation sleptons in R-parity violating supersymmetry. It is performed using the integrated luminosity of $\mathcal{L} = 19.7\,\mathrm{fb}^{-1}$ of proton-proton collisions recorded by the CMS experiment at the LHC, CERN during 2012. The centre-of-mass energy during this period was set to $\sqrt{s} = 8\,\mathrm{TeV}$.

The theoretical basis of this analysis is the cMSSM model, which limits the amount of free supersymmetric parameters to a manageable amount. As the commonly assumed R-parity is replaced by another discrete symmetry called "baryon triality", additional parameters are available. To investigate the new lepton number violating Yukawa coupling λ'_{211}, single coupling dominance for this parameter is assumed. As a consequence, production of a single second generation slepton through two first generation quarks becomes possible. The decay signature of the slepton includes two muons and two jets, of which the lepton charges have the distinct possibility to be of the same sign. This sets the final state apart from almost all Standard Model processes. Additionally, the amount of missing transverse energy is quite low, as all particles of the final state can be fully reconstructed. Several analysis requirements are designed around exploiting these attributes, which results in the background being of the same order of magnitude as the signal. A portion of the remaining background samples is replaced by a data-driven estimate to avoid dealing with difficult to simulate multi-jet processes in the final state. No significant deviation of the data from the background prediction can be observed and limits are set on λ'_{211} over a wide range of the m_0-$m_{1/2}$ phase space. They both expand the parameter coverage and improve the limits with respect to the 2011 analysis predecessor by roughly a factor of 2. A smuon mass of 1200 GeV is typical for the examined phase space and corresponds to a 95 % CL limit of $\lambda'_{211} \leq 8 \cdot 10^{-3}$.

Kurzdarstellung

Präsentiert wird die Suche nach resonanter Produktion von Sleptonen der zweiten Generation in R-Paritäts-verletztender Supersymmetrie. Es wurden Daten mit einer integrierte Luminosität von $\mathcal{L} = 19.7\,\mathrm{fb}^{-1}$ der Proton-Proton Kollisionen die vom CMS Experiment am LHC, CERN während 2012 aufgezeichnet wurden verwendet. In diesem Zeitraum betrug die Schwerpunktsenergie $\sqrt{s} = 8\,\mathrm{TeV}$.

Die theoretische Grundlage dieser Arbeit ist das cMSSM, was die Anzahl der freien supersymmetrischen Parameter auf eine überschaubare Größe limitiert. Die oftmals vorausgesetzte R-Parität ist durch eine andere diskrete Syemmtrie namens "Baryon Trialität" ersetzt, wodurch weitere Parameter hinzukommen. Um die neue Leptonenzahl-verletzende Yukawa Kopplung λ'_{211} zu untersuchen, wird angenommen dass diese die einzig relevante der neuen Kopplungen ist. Dadurch ist die Produktion eines Sleptons der zweiten Generation durch zwei Quarks der ersten Generation möglich. Die Zerfallssignatur des Sleptons schließt zwei Myonen und Jets mit ein, wobei die Ladungen der Leptonen die charakteristische Möglichkeit haben das selbe Vorzeichen zu tragen. Dies hebt den Endzustand von fast allen Standardmodell Prozessen ab. Zusätzlich dazu liegt nur wenig fehlende transversale Energie vor, da alle Teilchen des Endzustands vollständig rekonstruiert werden können. Um diese Eigenschaften auszunutzen werden mehrere Bedingungen erstellt, welche dazu führen, dass der Untergrund und das Signal von der selben Größenordnung sind. Ein Teil der verbleibenden Untergründe ist durch eine datengestütze Vorhersage ersetzt, damit man es vermeidet mit schwierig zu simulierenden Multi-Jet Prozessen im Endzustand zu arbeiten. Keine signifikante Abweichung der Daten von der Untergrundvorhersage wird beobachtet und es werden Ausschlußgrenzen auf λ'_{211} in einen großen Bereich des m_0-$m_{1/2}$ Phasenraums gesetzt. Diese erweitern die abgedeckten Parameterbereiche und verbessern die Grenzen in Hinsicht auf die Vorgängeranalyse der Daten des Jahres 2011 um etwa einen Faktor 2. Eine Smyonmasse von 1200 GeV ist typisch für den untersuchten Phasenraum und entspricht einer 95 % CL Ausschlußgrenze von $\lambda'_{211} \leq 8 \cdot 10^{-3}$.

Contents

Chapter 1

Theoretical Background

1.1. Standard Model of Particle Physics

Unless cited otherwise, this section is mostly based on the book "Introduction to elementary particle physics" by David Griffiths [1].

1.1.1. General Overview

The "Standard Model of particle physics" that has mostly been developed throughout the last century serves as the basis for almost all analyses in high energy particle physics. It achieves to describe and predict all electromagnetic, strong and weak force processes that have been observed with very high precision. The particles, although by themselves very tiny in size, if any size at all ($< 10^{-18}$ m), are what our entire (visible) universe consists of.

As one is looking for new physics beyond the Standard Model, it is essential to understand said model very well to differentiate between what one perceives as a known process and what goes beyond.
The current "particle-zoo", as people liked to call the collection of the Standard Model's components, divides all particles into two groups by sorting them based on their spin attribute. The ones with half integer spin, responsible for creating matter, are called fermions. Integer spin particles, mediators of the respective forces, are called bosons. The fermion subgroup is once again divided into leptons and quarks, which are grouped into three families each.

Each **lepton** family is a doublet consisting of a charged ($l, Q_e = -1$) and a neutral particle ($\nu_l, Q_e = 0$). The doublets have the following particle content:

$$\begin{pmatrix} \nu_e \\ e \end{pmatrix} \quad , \quad \begin{pmatrix} \nu_\mu \\ \mu \end{pmatrix} \quad , \quad \begin{pmatrix} \nu_\tau \\ \tau \end{pmatrix}$$

The first family is home to the electron e, which is accompanied by the electron neutrino ν_e. Every subsequent family consists of members with the same properties, except for their higher mass. They are named muons μ and muon neutrinos ν_μ, as well as taus τ and tau neutrinos ν_τ. Due to the mass hierarchy, particles from the higher families usually decay into one of the lower ones, for example $\mu \to e + \bar{\nu}_e + \nu_\mu$. The main difference between the partner particles of every family, aside from their charge, is the frequency with which they interact with matter. While interactions are common for electrons, neutrinos are barely noticeable due to the scarcity of interactions and have gone undetected for more than 20 years after their existence has been proposed.

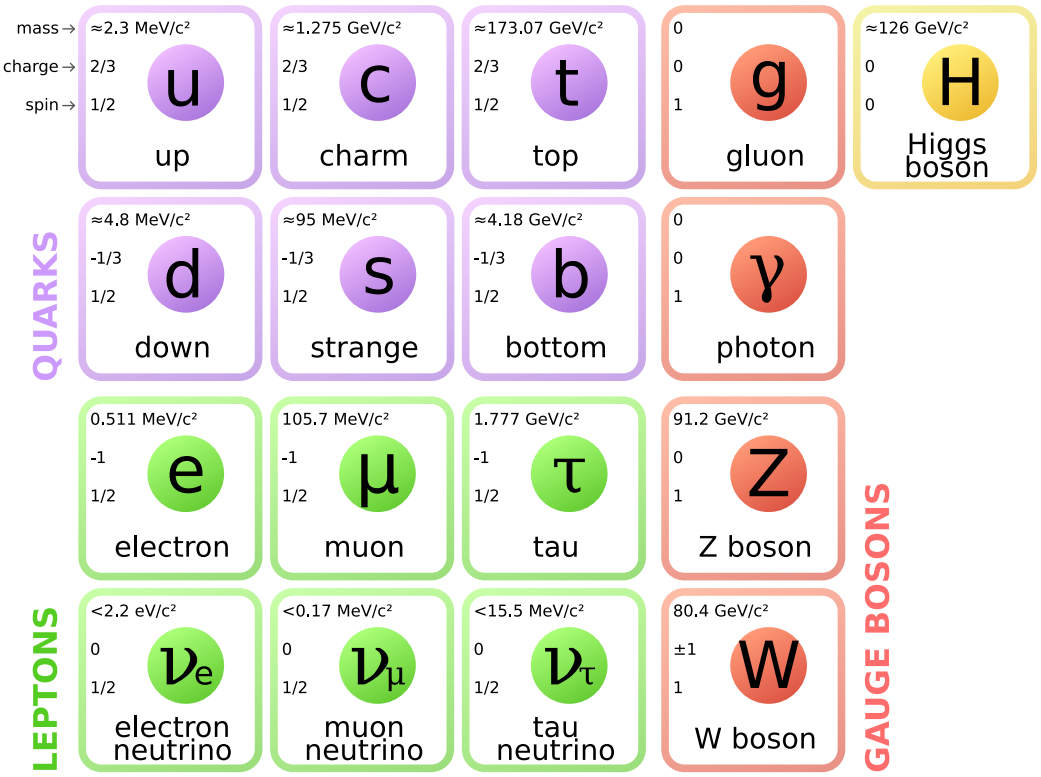

Figure 1.1.: The Standard Model's particle content [2, 3].

Quarks do not harbour such fundamental differences between each other. Each family consists of an up-type ($q_u, Q_e = +\frac{2}{3}$) and a down-type ($q_d, Q_e = -\frac{1}{3}$) particle.

$$\begin{pmatrix} u \\ d \end{pmatrix} \quad , \quad \begin{pmatrix} s \\ c \end{pmatrix} \quad , \quad \begin{pmatrix} t \\ b \end{pmatrix}$$

The first family has the up- and down-flavoured quarks u and d, respectively. Similarly to the lepton families, every subsequent family differs only by their increasing mass. Their names are strange s and charm c, as well as top t and bottom b. Quarks, as opposed to leptons, are found in bound states[1]. They consist of two or three quarks, which are named mesons and baryons. While the two-quark states are unstable, certain baryons such as the proton (uud) and neutron (udd) are stable over longer periods of time.

While baryons and leptons can join to create atoms and therefore matter, **bosons** are necessary for the interactions between said particles. Each of the five bosons is responsible for mediating one type of force.

For electromagnetic interactions, such as electron pair production and annihilation $e^+e^- \rightarrow \gamma \rightarrow e^+e^-$, the photon γ is the mediator. The strong force's gluons g mediate interactions between quarks. They are able to bind quarks (e.g. of a proton) despite the electromagnetic repulsion, due to it being a 100 times stronger at and below femtometer length scales. The weak force is mediated by the two vector bosons W and Z. Unlike the other forces, the weak one is able to change the flavour of quarks (even violating the otherwise conserved family

[1] The quark-gluon-plasma, a state of extremely high energy and/or density, is an exception to that. It is assumed to allow for asymptotically free quarks and gluons.

Force	Mediator	Relative Strength	Range [m]
Strong	Gluons g	1	10^{-15}
Electromagnetic	Photons γ	10^{-2}	∞
Weak	W & Z bosons	10^{-6}	10^{-18}
Gravitation	Graviton G	10^{-38}	∞

Figure 1.2.: The four fundamental forces and their attributes. "Strength" is to be taken as a rough estimate, as it ultimately is an ambiguous quantity. It depends on the nature of the source and what it is applied on.

number) and leptons. Gravitons G have been predicted, but not yet observed. As there are no negative masses which would lead to repulsion, Gravitation dominates on large, cosmic scales. It is responsible for the formation of galaxies and their substructures. Since there is no quantized formulation of the gravitational force, it is not part of the Standard Model.

For almost all particles in the SM, there is also a corresponding antiparticle. Antiparticles have the same properties as their normal counterparts, except for their charge-like properties[2] For example a negatively charged electron ($Q_e = -1$) has a positively charged ($Q_e = +1$) antiparticle called the positron. For uncharged particles, this means that they are their own antiparticle. Collisions between a particle and its counterpart usually leads to "annihilation". As the name suggests, this leads to both objects being destroyed. Particles produced in this annihilation carry the energy and momentum, which is set free in the process. Taking the electron-positron annihilation as an example, the resulting photon can also produce matter once again, supposed it has enough energy. At least the rest mass of both particles in terms of energy is necessary. This means for the aforementioned example that an electron-positron production ("pair production") is possible, but not necessarily the only option. Similarly muons, taus or quarks could have been the result as long as the charge-like properties are being conserved in the process.

1.1.2. Gauge Symmetry

The Standard Model of particle physics is a relativistic gauge theory, which is invariant under local gauge transformations. Relativistic field theories are formulated using a Lagrangian (density) $\mathcal{L}(\phi_i, \partial_\mu \phi_i)$, which is a function of time and spatial coordinates as well as its derivatives. The most basic Lagrangian for a spin $\frac{1}{2}$ particle is called a "Dirac Lagrangian".

$$\mathcal{L} = i(\hbar c)\bar{\psi}\gamma^\mu \partial_\mu \psi - (mc^2)\bar{\psi}\psi \tag{1.1}$$

It describes a free particle with no external fields. Here, ψ represent "Spinors", which are the most basic description of a particle.

1.1.3. Quantum Electro Dynamics

Requiring local gauge invariance for the Lagrangian (1.1) yields additional terms, which are being compensated for by introducing the covariant derivative:

[2] It has not yet been determined whether neutrinos are Dirac or Majorana particles. Hence, this statement does not apply to them.

$$\mathcal{D}_\mu = \partial_\mu + i\frac{q}{\hbar c}A_\mu \tag{1.2}$$

By using the covariant derivate (1.2), the invariance of the Lagrangian is restored. However, a spin-1 vector field A_μ is also added. To conserve the invariance, the mediator of the field to be massless $m_A = 0$. This yields the Lagrangian for quantum electro dynamics

$$\mathcal{L}_{\text{QED}} = i(\hbar c)\bar{\psi}\gamma^\mu\partial_\mu\psi - (mc^2)\bar{\psi}\psi - \frac{1}{16\pi}F^{\mu\nu}F_{\mu\nu} - \frac{1}{c}\underbrace{(q\bar{\psi}\gamma^\mu\psi)}_{\text{Source}J^\mu}A_\mu. \tag{1.3}$$

So by requiring local gauge invariance under a transformation $\psi \to U\psi$ with a unitary 1×1 matrix U, here $U = e^{i\theta}$, the photon as the mediator of the electromagnetic force is introduced to the free Lagrangian. It is massless, has a spin of 1 and since its transformation does commutate, it does not interact with other photons. The latter aspect is also coherent with the photon not carrying any electric charge. The group of all such transformations is called $U(1)$. Using the same principle but different groups of transformations, the remaining interactions will be introduced as well.

1.1.4. Quantum Chromo Dynamics

By expanding local gauge invariance from unitary 1×1 transformations $U(1)$ to the special unitary group $SU(3)$ for the flavour space, one adds the strong interaction to the Lagrangian. The previously single component spinors ψ now carry the colour charge and are extended as follows:

$$\psi \to \psi = \begin{pmatrix} \psi_{\text{red}} \\ \psi_{\text{green}} \\ \psi_{\text{blue}} \end{pmatrix} \tag{1.4}$$

Due to $\dim SU(3) = 8$, eight new fields are introduced, which represent the massless mediators: Gluons. Since the transformation is not abelian, these mediators self-couple. Therefore the gluons have to carry the colour charge. They are bi-colour objects containing one colour and one anti-colour. The reason for the naming scheme being borrowed from chromatics, is due to the way particles couple. One can only observe neutrally coloured states. This means that a quark, which are the only fermions to carry a colour charge in the Standard Model, has two options. Either couple to a quark of its anticolour or two other quarks, who carry the remaining two colour charges of the r, g, b triplet. As mentioned in section 1.1.1, those are called mesons and baryons respectively.

Another important aspect of QCD that stems from the self-coupling of gluons, is the behaviour of the strong coupling constant $\alpha_s(Q^2)$. Since it decreases as function of rising momentum transfer Q^2, the particles become less constrained the higher the energy scale of the interaction. This is called "asymptotic freedom" and can be described pertubatively. On the other end of the scale, around $\sqrt{Q^2} \sim 200\,\text{MeV}$, $\alpha_s(Q^2)$ becomes very large and this freedom turns into "confinement". Here the pertubation theory diverges and quarks as well as gluons do not appear as free particles anymore.

1.1.5. Electro Weak Theory

Unlike both the electromagnetic and strong interactions, the weak force has two different "types" of interactions. There are neutral current (NC) and charged current (CC) interactions. To describe the latter as a gauge theory, the symmetry group $SU(2)_L$ is being used. The index "L" indicates that these types of currents only couple to left-handed particles and therefore violate parity conservation maximally. In reference to the spin and isospin attributes, the charge of this interaction is called "weak isospin" I^3. Using the weak isospin, left-handed particles can be sorted into doublets with e_L^- and u_L having $I = \frac{1}{2}, I^3 = -\frac{1}{2}$, as well as ν_L and d_L having $I = \frac{1}{2}, I^3 = +\frac{1}{2}$. Since right-handed particles do not partake in the charged current interaction, they are sorted into singlets with $I = 0, I^3 = 0$.

Using the $SU(2)_L$ symmetry group yields a third weak interaction. As this only couples to left-handed particles, it cannot be the weak neutral current which couples to both types. Instead a generator called "hypercharge" Y is introduced and defined by:

$$Q_e = I^3 + \frac{Y}{2} \tag{1.5}$$

$$\Leftrightarrow Y = 2\left(Q_e - I^3\right) \tag{1.6}$$

This extends the symmetry group by a $U(1)_Y$, thus being $SU(2)_L \otimes U(1)_Y$. The resulting gauge fields are called $W_\mu^i, i = 1, 2, 3$ for the $SU(2)_L$ and B_μ for the $U(1)_Y$. These gauge fields mix into two charged and two neutral bosons:

$$W_\mu^\pm = \sqrt{\frac{1}{2}}\left(W_\mu^1 \mp W_\mu^2\right) \tag{1.7}$$

$$A_\mu = \; B_\mu \cos\theta_W + W_\mu^3 \sin\theta_W \tag{1.8}$$

$$Z_\mu = -B_\mu \sin\theta_W + W_\mu^3 \cos\theta_W \tag{1.9}$$

The mixing-angle θ_W is a free parameter of the Standard Model, meaning that it cannot be predicted from its theoretical construct and has to be measured instead.

The aforementioned NCs are mediated by the Z-boson and behave very similarly to the ones based on an exchange of photons γ. Charged current (CC) interactions have the $W^\pm$-boson as their gauge mediator, which, contrary to all other types of interactions, allows for changes of flavour. While the $W^\pm$ and Z bosons are represented by their respective fields, A_μ can be recognized as the photon introduced by QED (Sec. 1.1.3). The electroweak theory therefore describes the combination of both the electromagnetic and weak interaction by unifying them into a single gauge theory [4–6].

The Standard Model of particle physics describes Nature very well. While the agreement between theory and experiment can be as good as multiple orders of magnitude, there are still certain discrepancies between theory and experiment. One of them will be addressed in the following section.

1.1.6. The Higgs Mechanism

While the initial two mediators of the respective gauge theories were massless, the W and Z bosons are not. In fact, they are quite heavy with roughly 80.4 GeV for the W and 90.2 GeV for the Z. This means that the mass terms for both bosons do not vanish and therefore the

local gauge invariance, as described in the QED section (Sec. 1.1.3), is violated. To alleviate this issue, the concept of "spontaneous symmetry breaking" can be used. For this purpose a new field is introduced to the Lagrangian:

$$\mathcal{L} = \frac{1}{2}(\partial_\mu \phi)^*(\partial^\mu \phi) + \frac{1}{2}\mu^2(\phi^*\phi) - \frac{1}{4}\lambda(\phi^*\phi)^2 \tag{1.10}$$

Unlike the spinors used in the previous equations, the field ϕ is imaginary and scalar. While spatial symmetry $\phi \to -\phi$ is maintained, the same cannot be said for the ground state anymore. As shown in figure 1.3, a unique, non-symmetrical ground state can be attained through spontaneous symmetry breaking.

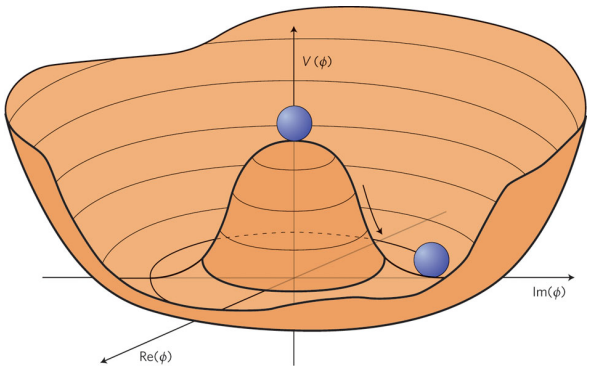

Figure 1.3.: The potential of the Higgs-Lagrangian. It is shown how through spontaneous symmetry breaking a non-symmetric ground state can be chosen [7].

Particle masses are generated by coupling to the Higgs field. While the mass generation terms are different for fermions and bosons, higher coupling strengths lead to higher masses in both cases. This extension to the theory described by the Lagrangian was suggested by F. Englert, R. Brout [8] and P. Higgs [9], who also lends his name to the new "Higgs-boson". This boson is the mediator of the Higgs coupling.

The search for the Higgs boson by the CMS collaboration at the Large Hadron Collider has found statistically significant evidence for the existence of a new boson (which resembles the proposed Higgs boson very closely). While previous publications have already shown a 5σ excess around the invariant mass of $m_X = 125\,\text{GeV}$ [10], further studies have been performed on the $H \to ZZ$ decay mode. One can see the invariant mass of four selected leptons m_{4l} in figure 1.4.

Combining the results from the $H \to ZZ$ decay channel with the $H \to \gamma\gamma$ one, which are the two channels with the best mass resolution, yields the current best mass estimate of $125.8 \pm 0.4\,(\text{stat}) \pm 0.4\,(\text{syst})\,\text{GeV}$ [11].

1.2. Supersymmetry

With a well understood background, discussed in the previous section, one can progress on to physics beyond the Standard Model. One of the most popular and thoroughly investigated extensions is "supersymmetry", often abbreviated as "SUSY". This section is based upon the "Supersymmetry Primer" by Stephen P. Martin [12] and for the particular topic of R-parity violation, the work of Herbi Dreiner [13, 14] as well.

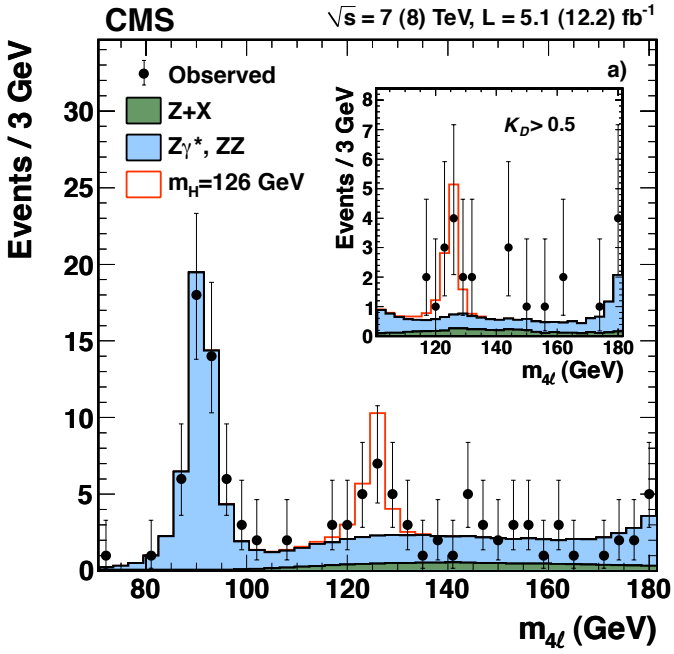

Figure 1.4.: Invariant mass of 4 leptons around the 125 GeV area, where an excess was observed beforehand [11].

1.2.1. Motivation

While the Standard Model describes a multitude of phenomena, there are still certain discrepancies and questions left unanswered. One of the reasons why supersymmetry has gotten as much attention as it has, is because it addresses some of these issues. Three of them will be outlined in the following sections.

Dark Matter

Observation of the universe has lead to the conclusion, that matter as we know it only contributes about 5 % to the entire energy content. The amount of dark matter and dark energy have been measured to be about 27 % and 68 %, respectively [15]. Several different methods have independently discovered phenomena that require a new type of matter. Figure 1.5 is showing the "Bullet Cluster", which is a prime example of dark matter observation through its gravitational lensing.
Measuring the rotation velocities of stars or gas as a function of their distance to the galaxy's core, also hints at a different type of matter. This is due to the fact, that visible matter itself would not be able to gravitationally bind objects of such high velocities at the observed distances to the galaxy. However adding an additional halo of (*invisible*) matter could provide the necessary additional gravitational force.

As this new type of matter has only been observed indirectly through its effect on nearby structures, it cannot be emitting photons (hence the name *dark* matter) or have a strong impact on cosmic rays. This leads to the assumption that only gravity and possibly the weak force may couple to it. Other interactions[3] are also within the realms of possibility, but would

[3] "Other interactions" do not include the electromagnetic one, as this would lead to direct optical observation.

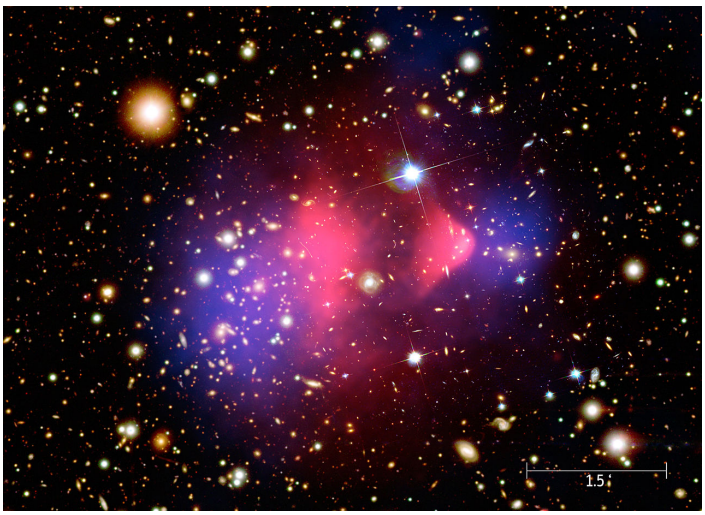

Figure 1.5.: Overlay of various images of the Bullet Cluster [16]. The background is an optical picture, while the baryonic gas, marked in red, is measured in the x-ray spectrum. Calculations based on gravitational lensing yield the dark matter marked in blue. Two galaxy clusters collided, with the baryonic gas being slowed down, while the dark matter passed through.

also necessitate a coupling not stronger than the weak one. These requirements seem to fit the description of the neutrino, but as dark matter tends to cluster, its particles have to be massive, cold dark matter.

One possible solution to the question what dark matter consists of are "Weakly Interacting Massive Particles". Often abbreviated as "WIMPs". The naming is self-explanatory. And while there are no candidates for this role in the Standard Model, supersymmetry does provide suitable particles. The most popular option amongst those, is the lightest supersymmetric particle or LSP, in case it is stable. As the mass hierarchy of supersymmetric particles can change depending on the parameters one chooses, there is not a set LSP. And while not all possible LSPs are considered WIMP candidates, some fit surprisingly well. Should supersymmetry be realized in nature and provide such an explanation for dark matter, it could solve one of the biggest mysteries in cosmology.

The Hierarchy Problem

Looking at the large differences in scales between the strengths of the gravitational and the weak forces (Tab. 1.2), one expects to see new physics when approaching the point where gravity becomes non-negligible on a quantum level. Considering that the mass of the Higgs boson is of the order $\mathcal{O}(100\,\mathrm{GeV})$ and couples to every massive particle, comparatively huge quantum corrections from heavy particles should contribute to its bare mass μ (Eq. 1.10). The Yukawa coupling to the Higgs field of a fermion is given by

$$\mathcal{L}_{\mathrm{Yukawa}} = -\lambda_f \bar{\psi} H \psi. \tag{1.11}$$

Here, λ_f denotes the coupling strength. The quantum loop correction of a fermion to the Higgs boson mass is depicted in figure 1.6a.

However, possible interactions that have yet to be discovered are an option as well.

(a) (b)

Figure 1.6.: Higgs boson with loop quantum corrections from a fermion 1.6a and a scalar 1.6b

Calculating this Feynman diagram yields

$$\Delta\mu = -\frac{|\lambda_f|^2}{8\pi^2}\left[\Lambda_{\mathrm{UV}}^2 + ...\right], \tag{1.12}$$

where Λ_{UV}^2 is the ultraviolet momentum cut-off that is used to stop the loop integral from diverging. It can be interpreted as the scale at which one no longer expects the Standard Model to provide an accurate description of nature any more, meaning that new physics will enter the equation. Assuming this cut-off to be of a much larger scale, e.g. the Planck scale $M_{\mathrm{P}} = 2.4 \cdot 10^{18}\,\mathrm{GeV}$, this would result in corrections that go beyond 30 orders of magnitude when compared to the $\mathcal{O}(100\,\mathrm{GeV})$ we expect for the Higgs' mass. The degree of fine-tuning necessary for this sort of parameter appears to be "unnatural".

However, in supersymmetry a scalar partner particle is introduced for every fermion, as well as a fermionic partner for every scalar particle. Assuming the couplings remain symmetrical, $\lambda_S = |\lambda_f|^2$, both loop corrections (Fig. 1.6a & 1.6b) would cancel each other out, because fermions and bosons have opposite sign contributions.

$$\Delta\mu = \frac{1}{8\pi^2}(\lambda_S - |\lambda_f|^2)\left[\Lambda_{\mathrm{UV}}^2 + ...\right] \tag{1.13}$$

This would provide a "natural" solution to the hierarchy problem for sparticle masses around the TeV scale, as the λ_S coupling correlates to said masses. The discovery of a light 125 GeV SM Higgs boson poses an upper limit on the sparticle masses in certain SUSY models.

Gauge Coupling Unification

Similarly to how the electromagnetic and weak force has been unified, the physics community has been looking to combine all four fundamental forces into one theory. As the individual forces show different behaviours at lower energy scales, a unification is only possible for high energy scales. Since the coupling strength parameters $\alpha_i(Q)$, $i = 1, 2, 3$ a function of the momentum transfer of the interaction, they intersect at certain energies. Figure 1.7 shows the evolution of $\alpha_i(Q)$ in both the Standard Model, as well as the minimal supersymmetric extension to it.

As one can see, there is no possibility for unification of all three couplings within the Standard Model, while in the extension the points of intersection are in close proximity of each other. Taking the uncertainties of an extrapolation far beyond the reach of current experiments such as this into account, this could hint at an underlying "grand unified theory" (**GUT**). This GUT is, as the name suggests, the previously mentioned effort to unify all the fundamental forces and would be realized around an energy scale of roughly $\sim 10^{16}\,\mathrm{GeV}$.

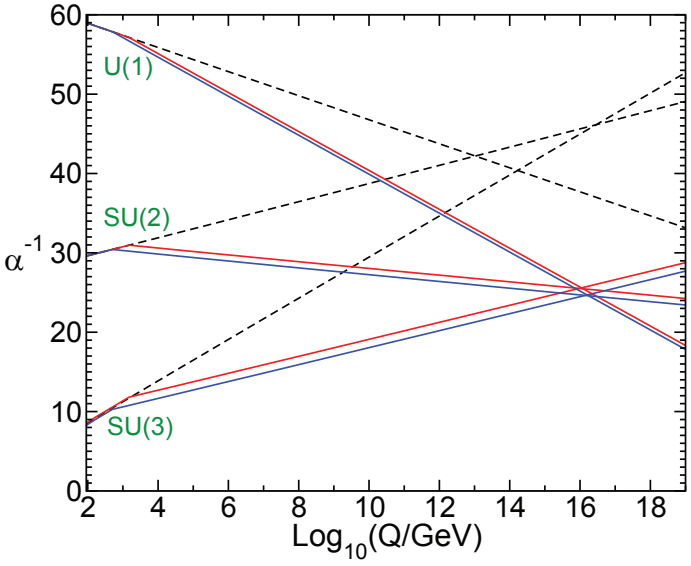

Figure 1.7.: Exemplary evolutions of the inverse gauge couplings $\alpha_i^{-1}(Q)$ through renormalization group equations [12]. The dashed lines show the Standard Model's prediction, while the coloured lines show the one of the Minimal Supersymmetric Standard Model.

1.2.2. The Minimal Supersymmetric Standard Model

In supersymmetry, the quantum property of integer and half-integer spin is being considered as a symmetry. This means relating a fermion to a boson and vice versa. Mathematically speaking an operator that transforms a fermionic state into a bosonic one and back, has to be introduced.

$$Q\,|Fermion\rangle = |Boson\rangle\,; \quad Q\,|Boson\rangle = |Fermion\rangle \tag{1.14}$$

The new states, which relate to Standard Model particles, are called superpartners. As a naming scheme for the partner-particles, the following rules apply. Adding *s-* as a prefix to a fermionic particle's name, yields the title for the scalar superpartner. Using the electron as an example, one gets the selectron. Likewise for scalar particles and their superpartners, the name has to be extended by the suffix *-ino*. The Higgs boson's counterpart would be the Higgsino.

The "MSSM", short for "Minimal Supersymmetric Standard Model", is the most commonly used and widely studied implementation of supersymmetry. The "minimal" expresses itself in the amount of superpartners added to the Lagrangian, which has been kept to the necessary minimum of two sets of doublets. Usually this means one superpartner for every left-handed and another one for every right-handed particle, which are then sorted into supermultiplets. The Standard Model's Higgs boson is insufficient for the MSSM, as adding just its superpartner would lead to an anomaly in the electroweak gauge symmetry. Thus the number of Higgs eigenstates, as well their supersymmetric counterparts, are extended to five. The supermultiplets of the MSSM are shown in table 1.1.

Similarly to how the gauge eigenstates W_μ^i and B_μ^0 mix to their respective mass eigenstates, the mass eigenstates for the MSSM particles also don't always coincide with a single gauge eigenstate. For the first two families of both the sleptons and squarks the mixing is assumed

Names		Spin 0	Spin 1/2
(s)quarks ×3 families	Q $\bar{U}$ $\bar{D}$	$\left(\tilde{u}_L\ \tilde{d}_L\right)$ $\tilde{u}_R$ $\tilde{d}_R$	$(u_L\ d_L)$ u_L d_R
(s)leptons ×3 families	L $\bar{E}$	$(\tilde{\nu}_e\ \tilde{e}_L)$ $\tilde{e}_R$	$(\nu_e\ e_L)$ e_R
Higgs (-inos)	H_u H_d	$\left(H_u^+\ H_u^0\right)$ $\left(H_d^0\ H_d^-\right)$	$\left(\tilde{H}_u^+\ \tilde{H}_u^0\right)$ $\left(\tilde{H}_d^0\ \tilde{H}_d^-\right)$
		Spin 1/2	Spin 1
gluino, gluon W (-ino) B (-ino)		$\tilde{g}$ $\tilde{W}^{\pm}, W^0$ $\tilde{B}^0$	g $W^{\pm}, W^0$ B^0

Table 1.1.: Supermultiplets of the Minimal Supersymmetric Standard Model [12]. Left-handed particles are sorted into doublets and right-handed ones into singlets.

to be negligible. The charged components of the third family however, do have different mass and gauge eigenstates:

$$\tilde{t}_L\tilde{t}_R \xrightarrow{\text{Mixing}} \tilde{t}_1\tilde{t}_2 \tag{1.15}$$

$$\tilde{b}_L\tilde{b}_R \xrightarrow{\text{Mixing}} \tilde{b}_1\tilde{b}_2 \tag{1.16}$$

$$\tilde{\tau}_L\tilde{\tau}_R \xrightarrow{\text{Mixing}} \tilde{\tau}_1\tilde{\tau}_2 \tag{1.17}$$

While in this case the amount of particles remains identical, the electroweak and Higgs gauge bosinos' mass eigenstates can only be sorted by their mass and charge:

$$\tilde{B}^0\tilde{W}^0\tilde{H}_u^0\tilde{H}_d^0 \xrightarrow{\text{Mixing}} \tilde{\chi}_i^0 \quad \text{with} \quad i = 1,2,3,4 \tag{1.18}$$

$$\tilde{W}^{\pm}\tilde{H}_u^+\tilde{H}_d^- \xrightarrow{\text{Mixing}} \tilde{\chi}_i^{\pm} \quad \text{with} \quad i = 1,2 \tag{1.19}$$

As the MSSM also requires new "Standard Model" Higgs bosons, these also mix[4]:

$$H_u^0 H_d^0 H_u^+ H_d^- \xrightarrow{\text{Mixing}} h^0 H^0 A^0 H^{\pm} \tag{1.20}$$

The h^0 resembles the Standard Model's Higgs closely and therefore the potential Higgs discovery from section 1.1.6 does not stand in conflict with the MSSM. Gluons and gluinos do not mix.

With the given particle content, the final step of the implementation is modifying the Lagrangian. Integration of the supersymmetric extension into it, requires the superpotential with the respective superfields from table 1.1 to be added.

$$W_{\text{MSSM}} = \bar{U}\mathbf{y_u}QH_u - \bar{D}\mathbf{y_d}QH_d - \bar{E}\mathbf{y_e}LH_d + \mu H_u H_d \tag{1.21}$$

[4]Note that Higgs fields are imaginary and out of the 8 degrees of freedom, 3 are used for the generation of the $W^{\pm}$ and Z bosons. The remaining 5 are the ones that mix to the given Higgs eigenstates.

The $\mathbf{y_i}$ with $i = u, d, e$ are the Yukawa coupling parameters. They are 3×3 matrices in flavour space and determine the mass spectrum. The μ-term is the supersymmetric version of the μ-term in the Higgs mechanism's superpotential (Eq. 1.10).

1.2.3. Soft SUSY Breaking

If supersymmetry were an exact symmetry, sparticle masses would be identical to their Standard Model counterpart. However, the lack of discoveries of at least the low mass components (e.g. the selectron) necessitates it to be a spontaneously broken symmetry. Should supersymmetry provide a solution to the fine-tuning problem, the resulting supersymmetric masses are expected to be within the reach of current experiments. One also has to keep in mind, that the "naturalness" of the solution to the hierarchy problem (Sec. 1.2.1) depends on the coupling strengths being equal. To allow the symmetry to be broken while keeping the cancellation of the loop contributions to the Higgs mass, requires the symmetry breaking to be *soft*. This means that the Lagrangian can be written like

$$\mathcal{L} = \mathcal{L}_{\text{SUSY}} + \mathcal{L}_{\text{soft}}, \tag{1.22}$$

to split the gauge and Yukawa couplings (SUSY) from the mass terms (soft).

To achieve this distinct form of the Lagrangian, a new interaction is necessary for which various models have been suggested. Out of the three most studied mechanisms, namely *Gauge mediated supersymmetry breaking*, *Anomaly mediated supersymmetry breaking* and *Gravity mediated supersymmetry breaking*, the latter, also known as *Planck-scale supersymmetry breaking*, is the most popular one. Its general idea is that, through the new physics that enter once gravity becomes relevant on a quantum scale, new gauge bosons mediate the masses of the supersymmetric particles. By requiring supersymmetry to be a local gauge symmetry, similarly to how the electroweak and strong force are implemented, one receives both a graviton (Spin 2) and a gravitino (Spin 3/2). It also yields an additional term for the goldstino, which is absorbed by the gravitino. The latter acquires mass due to the absorption. This theory is called supergravity.

Constrained Minimal Supersymmetric Standard Model

The simplest version of supergravity with the least amount of additional particles is called *minimal supergravity* (**mSUGRA**) or *constrained Minimal Supersymmetric Standard Model* (**cMSSM**). One of the reasons why this particular realization is popular, is the massive reduction of free parameters it achieves. While there are 105 of them in the MSSM, the scale dependency of the sparticle masses allows for a unification of multiple parameters at the grand unified theory (**GUT**) scale. Figure 1.8 displays how the individual scalar and fermionic masses are made to converge at the respective points of intersection.
Through the renormalization group equations, it is possible to extrapolate from these points. The remaining 5 parameters are:

- m_0 - Universal mass of scalar sparticles at the GUT scale
- $m_{1/2}$ - Universal mass of fermionic sparticles at the GUT scale
- A_0 - Trilinear Higgs coupling strength at the GUT scale
- $\tan\beta$ - Ratio of the vacuum expectation values of H_u^0 & H_d^0

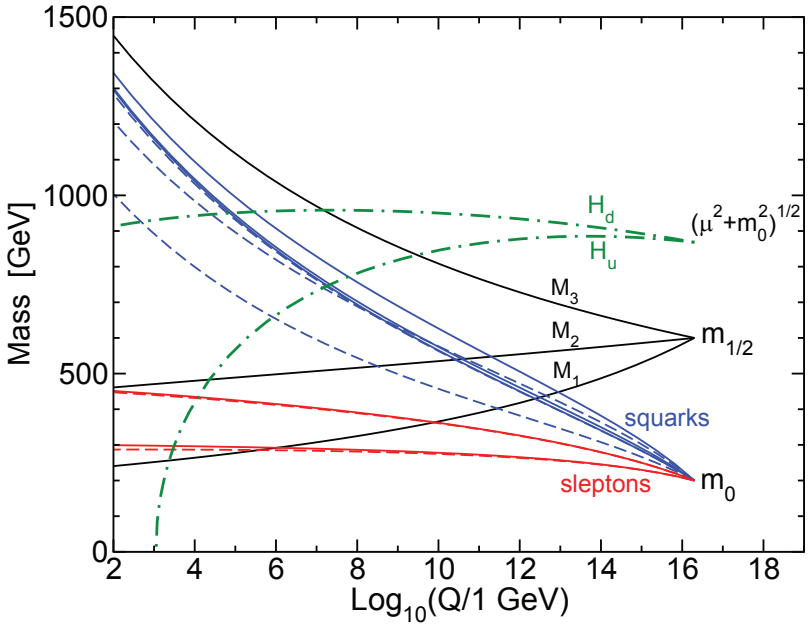

Figure 1.8.: Unification of sparticle masses at the GUT scale in the cMSSM [12], thus allowing for a significantly smaller amount of free parameters.

- $\operatorname{sgn}\mu$ - The sign of the bilinear Higgsino mixing parameter

1.2.4. R-Parity

When adding the most general superpotential for the MSSM to the Lagrangian, the theory appears to be self-consistent at first. However, certain phenomenological discrepancies would be left unaddressed. There are lepton number violating (**LNV**), as well as baryon number violating (**BNV**) terms:

$$W_{\mathrm{LNV}} = \frac{1}{2}\lambda_{ijk}L_iL_j\bar{E}_k + \lambda'_{ijk}L_iQ_j\bar{D}_k + \kappa^i L_iH_u \tag{1.23}$$

$$W_{\mathrm{BNV}} = \frac{1}{2}\lambda''_{ijk}\bar{U}_i\bar{D}_j\bar{D}_k \tag{1.24}$$

Here λ, λ', λ'' and κ denote the coupling strengths of the the respective interactions between the superfields (see tab. 1.1). The indices i, j, and k represent family numbers. Combinations of λ' and λ'' terms can, for example, lead to rapid proton decay. The latter has an experimental limit at 90% confidence level of $6.6 \cdot 10^{33}$ years, given by the Super-Kamiokande experiment in Japan [17].

To prevent this inconsistency, both types of terms could be suppressed by simply assuming the coupling parameters to be equal to zero. However in the MSSM, instead of simply forcing the theory to adhere to the observation through demanding certain parameters to be set, a new symmetry is introduced. The so called "R-parity" P_R is a discrete Z_2 symmetry and assigns a quantum number to every particle, which can be calculated from:

$$P_R = (-1)^{3(B-L)+2S} \tag{1.25}$$

One can easily confirm that every particle has an even R-parity ($P_R = +1$), while the supersymmetric counterparts have an odd R-parity ($P_R = -1$). Assuming R-parity is conserved, supersymmetric particles can only be produced in even numbers (usually pairs). This is due to it being a multiplicative quantum number, which calculates as follows for a vertex. With two particles entering one gets $P_R = (+1) \cdot (+1) = +1$. If they annihilate and produce two sparticles the calculation yields $P_R = (-1) \cdot (-1) = +1$. Obviously under R-parity conservation, this could not have produced one sparticle alongside one particle. This also forbids both the lepton and baryon number violating processes (Eq. 1.23 & 1.24) and has another major phenomenological consequence. The lightest supersymmetric particle (**LSP**) has to be stable, as any further decay would require an additional, even lighter supersymmetric particle. Should this LSP be neutral, it would only interact very weakly with baryonic matter. Under these circumstances, supersymmetry could provide a suitable candidate for a WIMP (compare to section 1.2.1).

The Violation of R-Parity

While most supersymmetric models do make use of R-parity, there is no intrinsic motivation for choosing this symmetry over others who can provide the same phenomenology. It can be shown that there are other, gauge anomaly free Z_N symmetries that can prevent the proton from decaying [14]. Baryon-triality B_3 is one of these models. The discrete symmetry for this scenario is given by [13]

$$\psi_j \to e^{\alpha_j 2\pi i/3} \psi_j. \tag{1.26}$$

The values of α_j for the respective superfields are given in table 1.2 below.

	Q_i	$\bar{U}_i$	$\bar{D}_i$	L_i	$\bar{E}_i$	H_d	H_u
α_j	0	2	1	2	2	2	1

Table 1.2.: Values of α_j for the respective superfields in the baryon-triality model.

Baryon-triality allows for the lepton number violating terms (Eq. 1.23), but forbids baryon number violating ones (Eq. 1.24). As a result the proton remains stable, while the LSP is able to decay. Due to the instability of the LSP in RPV supersymmetry, the idea of an LSP being a dark matter candidate has to be abandoned. However, resonant production of sleptons is possible, which can lead to very distinct decay chains (without "invisible" particles). The baryon-triality model is used as motivation for narrowing down the possible R-parity violating couplings.

1.2.5. Analysis Model

In the present analysis, the resonant production of sleptons through a single R-parity violating coupling is studied (cf. sec. 1.2.4). Strict limits on the combination of multiple couplings ($\mathcal{O}(10^{-5})$ and beyond) discourage searches anything other than assuming single coupling dominance [18]. To determine the viable couplings through which sleptons (Eq. 1.23) can be produced, one has to keep the initial state in mind. For proton-proton collisions this strongly favours the LQD term with λ'_{ijk}, as it is able to convert two quarks directly into a slepton. With the valence quarks of a proton being of the first generation, their contribution to the coupling will be dominant. While this sets $j = k = 1$, the remaining index determines the generation of the sleptons.

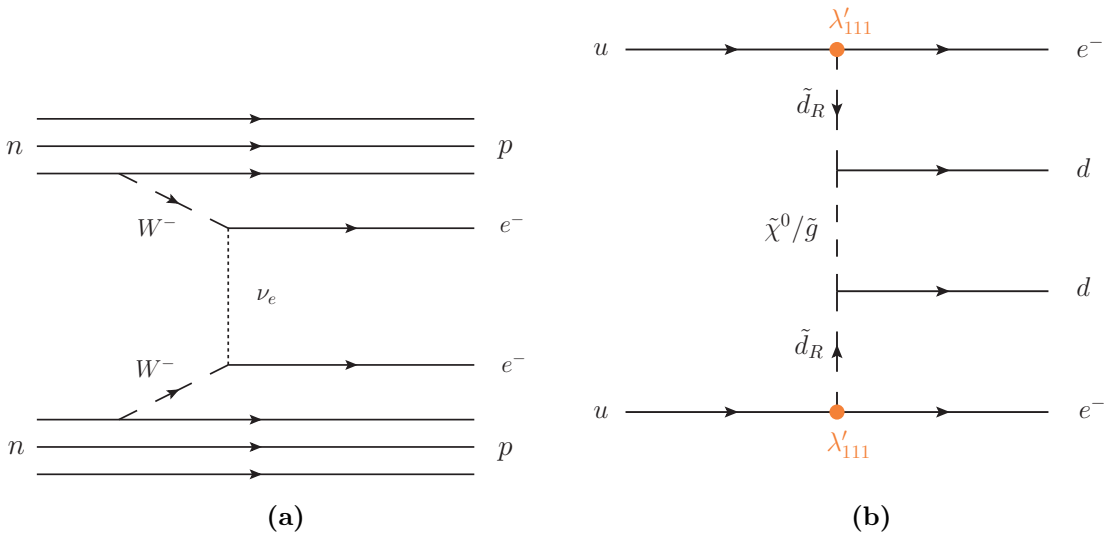

Figure 1.9.: Feynman diagrams of neutrinoless double beta decays. Via W bosons (1.9a) and the R-parity violating coupling λ'_{111}.

Neutrinoless double beta decay experiments investigate final states with two same sign charge electrons (Fig. 1.9), hence they puts bounds on the coupling for the first generation λ'_{111}. The order of magnitude of the limit is $\lambda'_{111} < 10^{-4}$ [18]. This strict limit favours a search for the production of second generation sleptons through λ'_{211}. With the assumption of an unstable LSP, there exists a lower limit of $\mathcal{O}(10^{-12})$ on all coupling parameters λ, λ' and λ''. Cosmological studies of the Big-Bang nucleosynthesis predict a certain abundance of light elements. For values below the lower limit, the decay of LSPs would modify these [18]. In line with the single coupling dominance assumption, any contributions from couplings other than λ'_{211} are being neglected.

Current Limits

While R-parity conserving scenarios are more popular and therefore more thoroughly investigated, there have also been searches for R-parity violating supersymmetry, with which this analysis concerns itself with. As none of these searches lead to any discoveries, their main results are limits on the value of λ'_{211}. Pion decays can be mediated by the λ'_{211} coupling as depicted in figure 1.10.
Measuring the branching fractions of pion decay modes yielded limits on the coupling parameter group $\lambda'_{21i}, i = 1, 2, 3$. They are given by $\lambda'_{21i} < 0.059 \cdot m_{\tilde{d}_{k,R}}/100\,\text{GeV}$ [18] and show a dependence on the mass parameters.

Even stricter limits have been determined with a direct search, using the $D0$ experiment at the Tevatron [19, 21], and are given in figure 1.11a. These 95 % confidence level exclusion limits are the most stringent limits from a collider experiment prior to the LHC.

Due to the technically more advanced combination of the LHC and CMS experiments, the results could be expanded upon. Figure 1.11b shows the extended, more strict limits, which were obtained using the data recorded during 2011 [20]. These exclusion ranges are the basis for this analysis.

The ATLAS experiment has not published any comparable results. However, their search for long-lived, heavy particles in final states with a muon and a displaced vertex [22] is

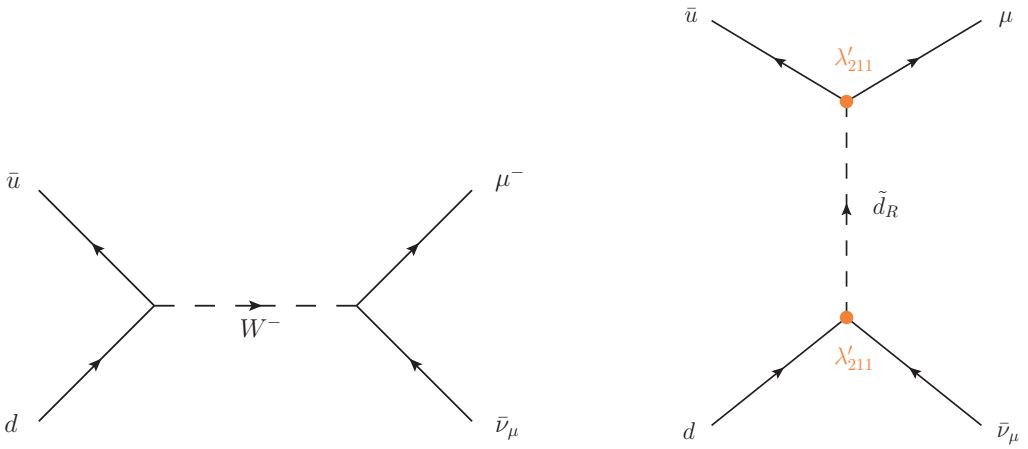

Figure 1.10.: Feynman diagrams of a pion decays. Via the W boson (1.10a) and the R-parity violating coupling λ'_{211} (1.10b).

sensitive to lower values of λ'_{2ij}. They focus on the possibility of a non-prompt decay of the neutralino LSP, where the values of λ'_{2ij} are below 10^{-6}, as opposed to this analysis. Due to this circumstance, the decay of the LSP is delayed and leads to a displaced vertex. Since their results are limits on the lifetime of the neutralino and are given as a simplified model interpretation, they are difficult to interpret for the model of this analysis.

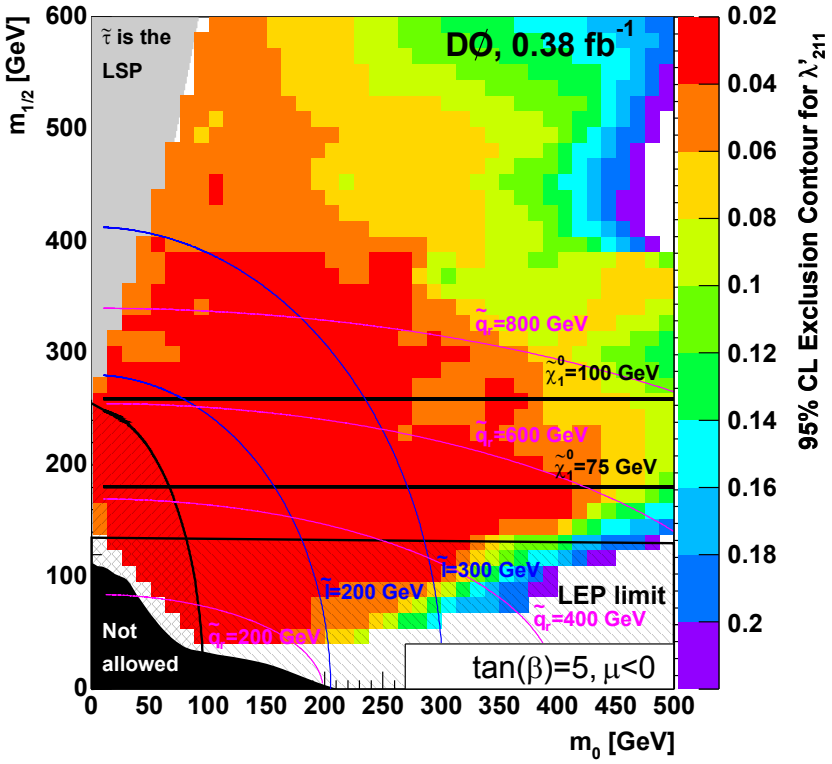

(a)

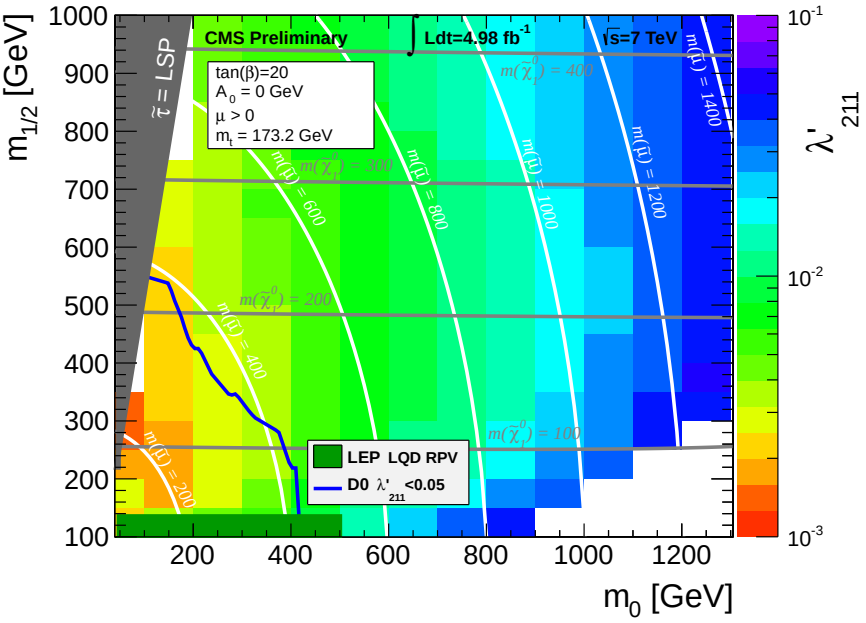

(b)

Figure 1.11.: 95 % C.L. exclusion limits for resonant slepton production through the λ'_{211} coupling. They have been calculated using the data measured by the D0 experiment (1.11a) [19] at the Tevatron in $p\bar{p}$ collisions at $\sqrt{s} = 2\,\text{TeV}$ and the measurements of CMS experiment at the LHC during 2011, which was operating at a centre-of-mass energy of $\sqrt{s} = 7\,\text{TeV}$ 1.11b [20].

Chapter 2

The Experiment

The analysis is based upon LHC proton-proton collisions at a centre-of-mass energy of $\sqrt{s} = 8\,\text{TeV}$, which have been recorded by CMS during 2012. This chapter will provide an overview over both the LHC, as well as the CMS experiment.

2.1. Large Hadron Collider

To study the structure of nature at the smallest scales, various particle accelerators with increasingly higher centre-of-mass energy have been built. The Large Hadron Collider (**LHC**) [23], built at CERN the European laboratory for particle physics, is the machine which currently provides the highest beam energies. It resides in a 27.6 km long, circular tunnel roughly 100 m underground, near Geneva, Switzerland. As opposed to the Large Electron-Positron collider (**LEP**) which previously operated in said tunnel, the LHC is designed to work with both protons and heavy ions, such as lead. This effectively allows for much higher centre-of-mass energies, as the synchrotron radiation decreases with increasing masses of the accelerated particles. To stay in line with the analysis' focus, the following sections will only concern themselves with proton-proton collisions.

Since most of the interesting interactions are very rare compared to the ones that have already been studied, it is essential for the LHC to produce a sufficient amount of collisions. The instantaneous luminosity $\mathcal{L}$ is a measurement of said rate of production. The expected number of events per second for a certain process is then given by

$$N_{\text{Process}} = \mathcal{L}\,\sigma_{\text{Process}}. \tag{2.1}$$

Here σ_{Process} denotes the cross-section, which can be interpreted as the probability of the considered process to occur. The design value for the instantaneous luminosity of the LHC is $\mathcal{L} = 10^{34}\,\text{cm}^{-2}\,\text{s}^{-1}$. At the end of the 2012 data taking period, the peak instantaneous stable luminosity recorded by CMS was $7.7 \cdot 10^{33}\,\text{cm}^{-2}\,\text{s}^{-1}$ [24], which is already very close to the design goal.

The LHC has been constructed for a centre-of-mass energy of $\sqrt{s} = 14\,\text{TeV}$, although reaching this design energy has been postponed. With each of the two beams carrying half the energy, 3.5 TeV per beam have been reached during 2011. It has been increased to 4.0 TeV in 2012. This slow start is mostly due to an accident during the start-up of the machine in 2008, which requires (still ongoing) extensive repairs and has lead to redesigning certain components.

The injector chain (Fig. 2.1) is responsible for supplying the LHC with protons. After extracting the particles from Hydrogen gas using an electrical field, the 90 keV protons are boosted to 750 keV by a radio frequency quadropole (**RFQ**) before entering a linear accelerator (**LINAC 2**). With 50 MeV they are sent to the Proton Synchrotron Booster (**PSB**), which feeds the Proton Synchrotron (**PS**) protons with 1.4 GeV kinetic energy. After being accelerated to 25 GeV the particles pass through the last pre-accelerator, which is the Super Proton Synchrotron (**SPS**). As they reach 450 GeV the trains of bunches are separated into two halves before being injected into the LHC.

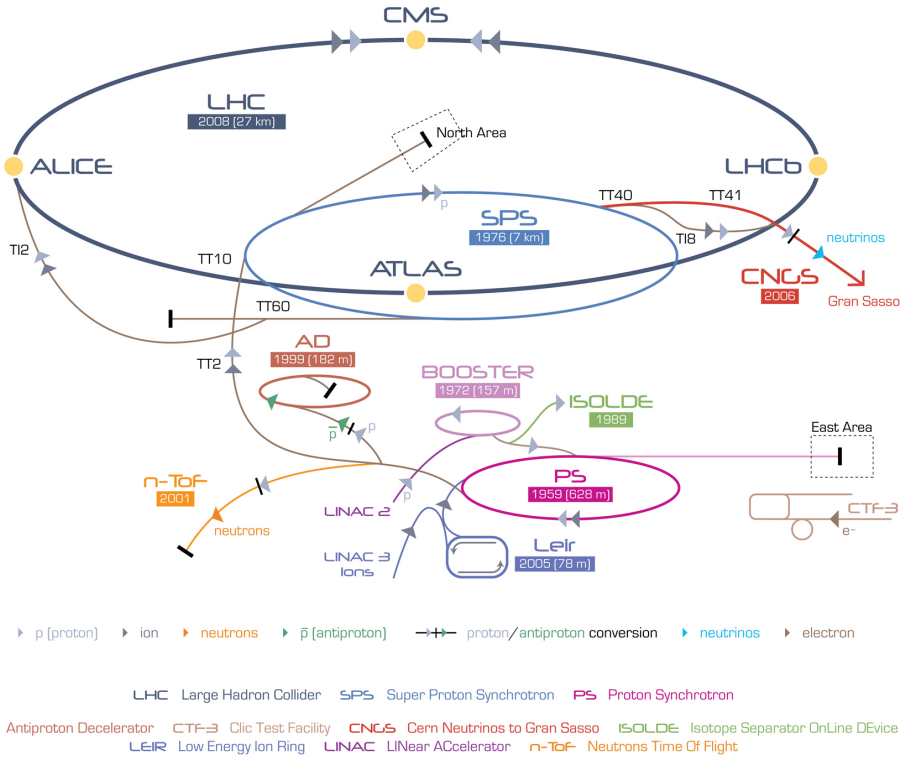

Figure 2.1.: Schematic picture of the injector chain for the LHC [25].

The LHC uses superconducting radio frequency cavities made of niobium to boost the protons to their final energy. Superconducting dipole magnets made of niobium-titanium are used to guide the proton's trajectory. Their B-field can reach up to 8 T. Quadrupole, sextupole and octopole magnets are used to clean and focus the beam. The four major experiments are located in caverns, where the two beams are crossing their paths. The ATLAS [26] and CMS [27] experiments are multi-purpose detectors, while ALICE [28] is focusing on heavy ions and LHCb [29] concentrates on b-quark physics.

2.2. Compact Muon Solenoid

Roughly 100 m below Cessy (France), at the fifth interaction point (**IP5**) of the LHC, the Compact Muon Solenoid (**CMS**) [27] is installed (Fig. 2.2). The cylindrical shape measures 21.6 m in length and has a diameter of 14.6 m, with an overall weight of 14 kT. It is composed of a large solenoid magnet and a wide variety of sub-detectors, with a *barrel* and an *endcap* region. In combination, they are designed to measure the energy, momentum and trajectory

of the particles. The individual components will be discussed in the upcoming sections.

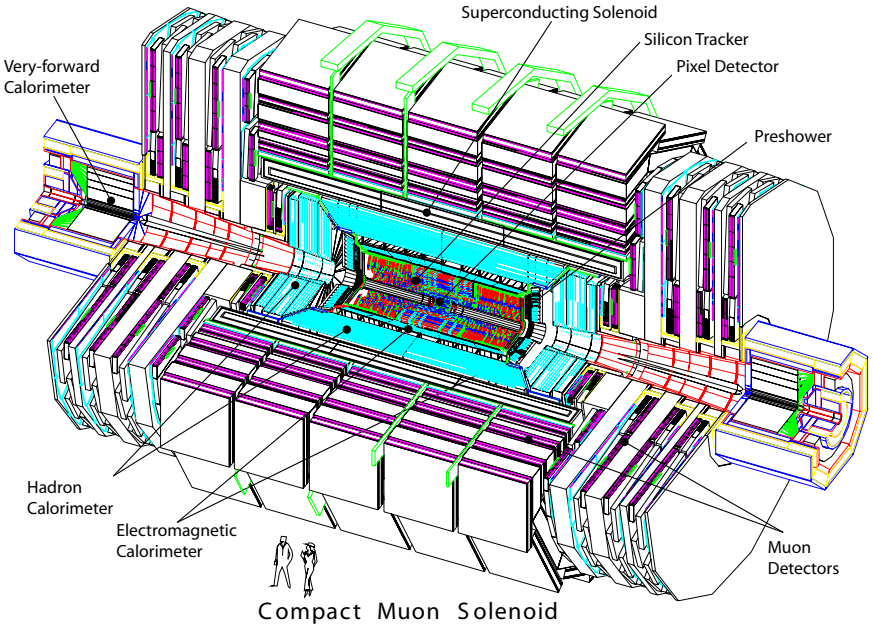

Figure 2.2.: Overview of the CMS experiment at the LHC [27]. For a size comparison, two experimentalists are shown.

The coordinate system chosen by the CMS collaboration places the origin at the nominal collision point of the two proton beams. The z-axis is along the path of the proton beams, while the x-axis points inward to the center of the LHC ring. That leaves only the vertical, upward direction for the y-axis. The radial coordinate r is measured with respect to the nominal interaction point and the azimuth angle ϕ is measured in the x-y plane. Instead of the polar angle θ, a quantity called "pseudorapiditiy" η is being used. It is given by $\eta = -\ln\tan\left(\frac{\theta}{2}\right)$, resulting in differences $\Delta\eta$ being invariant under longitudinal Lorentz boosts. Using the pseudorapidity, the spatial distance between two objects is defined as

$$\Delta R = \sqrt{(\Delta\phi)^2 + (\Delta\eta)^2}. \tag{2.2}$$

2.2.1. Magnet

The shape of the magnet is one of the main choices for an experiment. One has to weigh the trajectory bending power against the area density, where the former is essential to measure particle charge and momenta, while the latter can lead to losing or altering particle information due to various effects. The CMS collaboration chose a solenoid shape and thus having a magnetic field parallel to the beam line. One of the distinct features is the superconducting niobium titanium material organized in a 4-layer structure. With the cold mass of the magnet itself being "only" 220 tons, the 10 000 ton iron yoke surrounding the magnet from the outside is the main contribution to the overall weight. The iron yoke is necessary to return the magnetic flux to the solenoid. With the 3.8 Tesla the magnet is designed to operate at, it provides excellent bending power in the inner detector. In the muon chambers, only about 2 T remain.

2.2.2. Inner Tracker

The inner tracker (Fig. 2.3) is the detector component closest to the collision point. As such, it is faced with the biggest challenges. With about 20 proton-proton collisions up to every 25 ns, not only an extremely fast response time, but also an excellent spatial resolution is necessary. The radiation damage from said interactions also had to be considered. As a result, a detector based on silicon has been chosen and constructed. It has an expect lifetime of 10 years, after which it has to be replaced. The layout of the inner tracker has two components which will be discussed in the next sections.

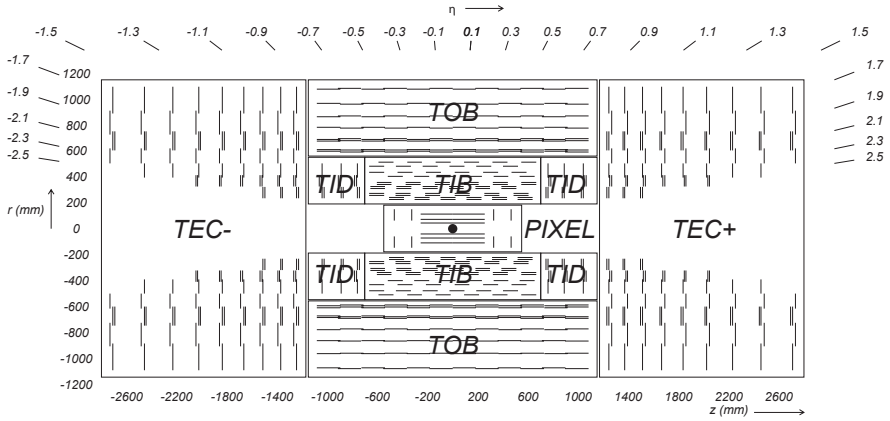

Figure 2.3.: Layout of the inner tracker of the CMS experiment. Every line represents a silicon detector, whereas the double lines have a secondary micro-strip detector to measure the respective second coordinate [27].

The **pixel detector** has its three layers at radii of 4.4, 7.3 and 10.2 cm in the barrel region. Two additional discs are positioned on each side. With an overall amount of 66 million pixels, it covers an area of roughly $1\,\mathrm{m}^2$. The $100 \times 150\,\mu\mathrm{m}^2$ pixel size provides an excellent track resolution of roughly $15 - 20\,\mu\mathrm{m}$. This allows for an accurate reconstruction of secondary vertices, giving valuable insight into the decay chains.

Outside of the pixel detector, the **silicon strip tracker** is extending from 20 to 116 cm. It has three different subcomponents. The Tracker Inner Barrel (**TIB**) with its 4 layers and the complementing 3 Tracker Inner Disks (**TID**) on each side, are positioned parallel and radial to the beam line, respectively. After reaching a radius of 55 cm the Tracker Outer Barrel (**TOB**) occupies the remainder of the barrel space with its 6 layers. Following the same structure as the TIB and TID, the endcaps are covered by the Tracker End Caps (**TEC**), which add another 9 layers of silicon strips. The width and pitch of each strip determine the spatial resolution. It varies between 23, 35 and 53 μm, with a tendency towards a better resolution the closer the strip is to the collision spot. Additional micro-strip detector modules are attached to the first two layers of the TIB, TID and TOB. Those are used for measuring the second coordinate (z for the barrel region and r in the disks) with a stereo angle of 100 mrad. Overall, the silicon strip tracker has a total of 9.3 million strips with a surface area of $198\,\mathrm{m}^2$.

Combining both components of the inner tracker, it is possible to measure the transverse momentum of highly energetic tracks ($\sim 100\,\mathrm{GeV}$) with a resolution of $1 - 2\,\%$. The geometrical range of $|\eta| < 2.5$ is being covered.

2.2.3. Electromagnetic Calorimeter

As the name suggests, the electromagnetic calorimeter (**ECAL**) is responsible for measuring electrons and photons. This also includes the electromagnetic component of jets, which is mostly given by $\pi^0 \to \gamma\gamma$. To simultaneously ensure good response times and a fine granularity[1], while still being resistant to radiation damage, lead tungstate crystals $PbWO_4$ have been chosen.

The barrel region covered by the calorimeter (**EB**) spans over $|\eta| < 1.479$. A total of 61200 crystals with a cross section of $22 \times 22\,\mathrm{mm}^2$ near the collision point and $26 \times 26\,\mathrm{mm}^2$ furthest from it, have been mounted. It should be noted that with these dimensions, the Molière radius is able to be contained within a cell, resulting in a good spatial resolution. The length of a cell corresponds to $25.8X_0$, ensuring the capture of most showers induced by electrons and photons. Avalanche photo diodes (**APD**) are installed on the outer surface of each cell and are used to measure the scintillation light, which translates to the deposited energy.

In the endcap calorimeters (**EE**) there are 7324 crystals split into one disk each on both sides. Their coverage extends from $|\eta| < 1.479$ to $|\eta| < 3.0$. However, due to the larger amount of radiation in these directions, the APDs have been replaced by the less efficient, but more resistant vacuum phototriodes (**VPT**).

To prevent neutral pions from being misidentified as single photons, a preshower detector is installed in front of the crystals in the range of $1.653 < |\eta| < 2.6$. The total thickness of 20 cm is composed of two layers of lead radiators, which are used to force electromagnetic showering and silicon strip sensors to measure them.

The energy resolution provided by the ECAL for particles below 500 GeV is given by

$$\left(\frac{\sigma_E}{E}\right)^2 = \left(\frac{2.8\%}{\sqrt{E/\mathrm{GeV}}}\right)^2 + \left(\frac{12\%}{E/\mathrm{GeV}}\right)^2 + (0.3\%)^2, \tag{2.3}$$

with the first term being the stochastic contribution, followed by the one from noise and the constant term being added last.

2.2.4. Hadronic Calorimeter

While most electrons and photons can be fully stopped using the ECAL, the nuclear interaction length (λ_I) of hadrons is much longer, thus allowing them to pass through. The hadronic calorimeter's (**HCAL**) main priority is the measurement of hadronic jets and other hadronic fragments from proton-proton collisions. The apparent missing transverse energy (**MET** or $\mathbf{E}_\mathrm{T}^\mathrm{miss}$) stemming from neutrinos or possibly new particles, can also be estimated by summing up all calorimetric measurements. Overall the HCAL has four sub-components.

The hadron barrel (**HB**) fills the space between the ECAL ($r = 1.77\,\mathrm{m}$) and the solenoid magnet ($r = 2.95\,\mathrm{m}$) for $|\eta| < 1.3$. It consists of 36 wedges with an individual width of 858 mm. While the top and bottom plate are made of steel, the rest of the absorber material is brass. Depending on the angle η, one layer of absorber material corresponds to an effective thickness of 5.82 to 10.6 interaction lengths λ_I (The ECAL provides an additional $1.1\,\lambda_I$). The absorber is followed by plastic scintillators, whose scintillation light is captured by wavelength-shifting fibres and subsequently read out by a hybrid photodiode (**HPD**).

In the $1.3 < |\eta| < 3.0$ region the hadron endcap (**HE**) is positioned. It is structured the same way as the HB, with the layers being orthogonal to the beam line, instead of parallel.

[1] High density: $8.28\,\mathrm{g/cm}^3$; Short radiation length: 0.89 cm; Small Molière radius: 2.2 cm

Since the HB is very restricted in terms of space, the hadron outer (**HO**) is added outside of the solenoid magnet. The latter then acts as absorber material. This sub-detector is meant to measure the remainder of hadronic activity, which did not deposit all of its energy in the HB. The wheels in the iron yoke behind the solenoid are equipped with a single layer of HO scintillators, with the exception of the $\eta = 0$ wheel. Due to the absorption material being at its minimum here, an additional 19.5 cm of iron and a second layer of scintillators is added. Overall the minimal interaction length is increased to 11.8 in the $|\eta| < 1.3$ region.

The final component, the hadron forward (**HF**), provides additional coverage for $|\eta| < 5.2$. Due to the exposition to massive amounts of radiation, it is based on grooved steel absorber plates with quartz fibers as an active medium. Although rarely used directly in analyses, the HF provides valuable information for the $E_{\mathrm{T}}^{\mathrm{miss}}$ calculation.

Combining both the ECAL and HCAL, the energy resolution for hadronic showers between 30 GeV and 1 TeV is designed to reach [30]

$$\left(\frac{\sigma_E}{E}\right)^2 = (100\%)^2 \cdot \frac{\mathrm{GeV}}{E} + (4.5\%)^2. \tag{2.4}$$

2.2.5. Muon System

One of the central aspects of the CMS experiment, as stated by the second part of the name already, is the detection of muons. With their distinct trajectories muons are very attractive particles to look for. As a result they are part of many signatures, for example the $H \to ZZ$ decay mode shown in figure 1.4. Due to the minimal ionizing nature of muons, most of them pass through the detector, including the calorimeters. This enables one to differentiate between them and other particles, but also implies that it is impossible to measure the energy through deposition in the calorimeters. As a result, the momentum measurement, which depends on the precise track reconstruction, gains that much more importance. This motivates the addition of muon chambers as they can aid in particle identification, provide additional trajectory measurements and can also be used for triggering.

The chambers are organized as wheels in the barrel region and disks in the endcap region. The three different types of gas based detectors cover an area of 25 000 m^2. A wide angle coverage is also ensured by extending up to $|\eta| < 2.4$.

Drift Tubes

Drift Tubes (**DT**) are installed in the barrel region ($|\eta| < 1.3$) in between the iron return yoke plates. They operate well with a comparatively low muon rate and a fairly uniform magnetic field, which is contained by the iron yoke. The low cost is also beneficial, considering the large area (172 000 tubes) that needs to be covered in this region. Every drift tube chamber consists of three superlayers, which contain four layers of drift cells. An exemplary cell is shown in figure 2.5. Overall there are four sets of muon chambers, usually called "stations".

In the first three stations, the cell in the middle is responsible for measuring the z-coordinate, while the other two measure the r-ϕ-component. The fourth station is only equipped with two superlayers, which focus on the r-ϕ measurement. Each of the 2.4 m long cells has a gold plated steel wire as an anode in the middle of the chamber with aluminium tape on each side of the wall acting as a cathode. As a muon crosses a cell, it ionizes the argon (85%), carbon dioxide (15%) mixture. The resulting electrons (ions) drift towards the anode (cathode), leading to a measurable current. While a single cell has a spatial resolution of 250 μm, one station with 2×4 hits reaches 100, μm.

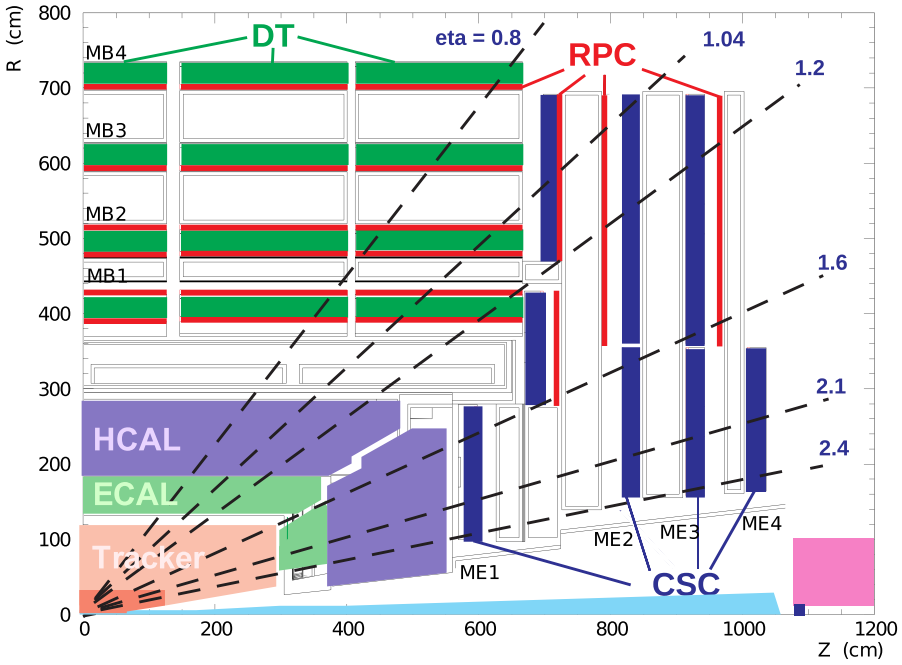

Figure 2.4.: Cross section of the CMS detector along the beam-pipe [31]. The regions marked with DT, CSC and RPC represent the muon system components.

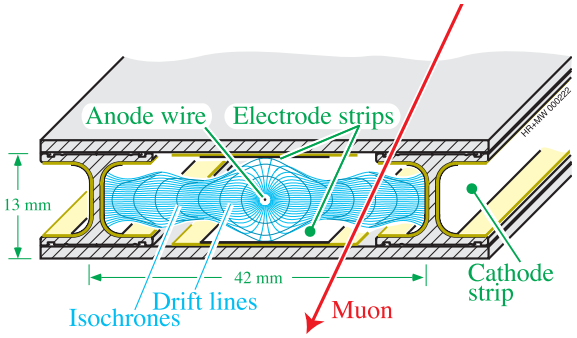

Figure 2.5.: Schematic drift cell of the drift tubes in the muon system of the CMS detector [32]. Both the driftlines and isochrones are shown.

Cathode Strip Chambers

The endcap region is faced with much higher muon and background fluxes, along with an inhomogeneous magnetic field. As a consequence, cathode strip chambers (**CSC**) are the detector of choice instead of DTs. They cover the $|\eta|$ range from 0.9 to 2.4, overlapping slightly with the DTs. The CSCs are trapezoidally shaped and consist of seven layers of radially oriented cathode strips each. Anode wires are placed perpendicularly to the strips inside the gas filled ($40\%\,\mathrm{Ar} + 50\%\,\mathrm{CO_2} + 10\%\,\mathrm{CF_4}$) gaps in between each layer. This layout allows for measuring both the ϕ-component with the strips and the r-component with the wires at the same time. The spatial resolution varies between $75\,\mu$m and $150\,\mu$m.

Resistive Plate Chambers

The third and final detector type are the resistive plate chambers (**RPC**). In comparison to the previous two components, they provide much faster response times due to being operated in avalanche mode. In the barrel region, there are overall six RPCs embedded. On the first two drift tube stations, there is one RPC mounted on each side, while only one is installed on each of the two outer stations. Additionally, there are planes of RPCs in between each of the first three stations of the endcap regions. This results in an overall coverage of $|\eta| < 1.6$, which will be expanded in the next upgrade cycle. The detector works with two parallel plates, where the gap is gas filled and read-out strips are placed in the middle. The usage of avalanche mode allows for response times comparable to scintillators, while the geometry yields adequate spatial resolution.

By combining the information from both the inner tracker, as well as the muon chambers, an overall transverse momentum resolution of 5% for highly energetic muons ($\sim 1\,\text{TeV}$) can be reached.

2.2.6. Triggering and Data Aquisition

Upon reaching the design luminosity, there are collisions every 25 ns corresponding to a rate of proton-proton interactions of about 10^9 Hz. However, the amount of data that is possible to be stored is a few 10^2 Hz. Therefore a preselection, specifically choosing events that potentially contain relevant physics, has to be made. The amount of data to be stored per event is reduced to about 1 MB in the process. The CMS experiment uses a two-level *trigger* system to perform said reduction.

The **Level-1** (**L1**) trigger is mostly based upon programmable electronics, which make use of the information provided by the different sub-detectors. Figure 2.6 shows the information chain of the L1 trigger system. Local triggers collect the basic information from the detector components, which are then combined in regional triggers and are eventually transferred to the global trigger. The latter decides whether or not to discard the event, by performing a preliminary reconstruction. The maximal latency between a bunch crossing and distributing the conclusion to read out the electronics is $3.2\,\mu$s. Overall, the L1 rate is designed to be about 100 kHz (typically ran at 98 kHz during 2012).

If an event is selected by the L1, the front-end buffers of all the sub-detectors are read out and the data is forwarded to the **data aquisition** (**DAQ**) system. Here the **high level trigger** (**HLT**) performs a much more sophisticated analysis on the collected data. It is able to do so, because it can access all digitized information. This provides an additional reduction to about 2 kHz (original design rate was 300 Hz).

Distributing the analysed data is the next step. The processed datasets are transferred from the Tier-0 at CERN to the Tier-1 locations, where further analyses are run. Next, it is distributed to the final destination in regards to central storage, the Tier-2 data centers. All CMS workgroups can access the datasets at this stage. It should be noted that the Tier-1 grid is also used for large-scale computing, while the Tier-2 resources are used for analyses.

2.2.7. Object Reconstruction

The information provided by the respective sub-detectors, such as a chamber hit or an energy deposit, have to be combined to a physics object for further analysis. Different kinds of

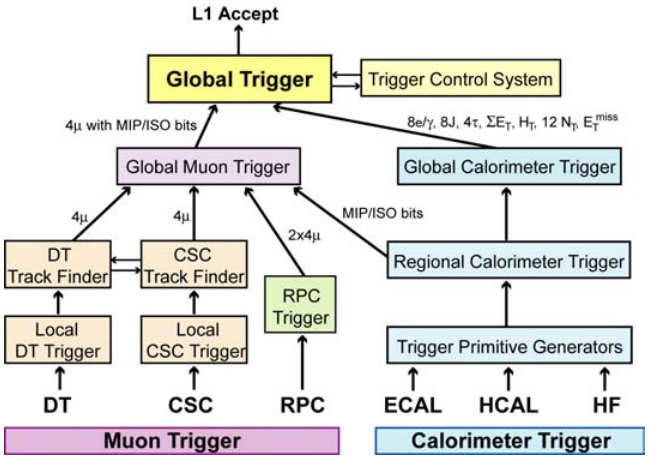

Figure 2.6.: Schematic overview of the architecture of the Level-1 trigger of the CMS experiment [27].

objects have individual algorithms. The ones relevant for the analysis will be covered in the next sections.

The reconstruction of **Muons** is solely based on their trajectory. Initially the tracker and muon system hit information are reconstructed separately. If a muon is reconstructed in the muon system, it is considered a *standalone muon*. The Kalman filtering technique [33] is used to reconstruct the trajectory. Starting with a seed, it considers nearby hits to iteratively build the track. Progressing on from the initial standalone muon track, one can compare it to a tracker trajectory by propagating both their parameters to a common plane. If a matching set of hits can be found, the muon becomes a *global muon* which is the most commonly used quantity. Alternatively the initial track can be taken from the tracker. These muon candidate trajectories are then extrapolated by taking various factors like average energy depositions, multiple scattering, precise magnetic field maps and Bremsstrahlung into account. If matching track segments are found in the muon system, the muon becomes a *tracker muon*. The latter is particularly useful for multiple (usually two) collimated muon tracks, as the spatial resolution of the tracker exceeds the one of the muon system by far.

Jets are a conglomerate of various, mostly hadronic particles. They usually stem from either a gluon or a quark. As jets are reconstructed as a single object, a specific algorithm has to be chosen to perform this task. A popular choice are sequential recombination algorithms such as the Cambridge/Aachen algorithm. In this analysis the **anti-k_T** clustering algorithm [34] will be used. It is both collinear and infrared safe, meaning that the reconstruction is neither significantly affected by splitting in the collinear direction nor the emission of soft particles. Unlike the other sequential recombination algorithms, this method provides a conical shape for which the cone radius parameter will be set to $R = 0.5$.

Both **electrons** and **photons** are mainly measured via the ECAL [35]. While the electron radiates photons as its trajectory is bent by the magnetic field, photons with sufficient energy can lead to pair production under the influence of electromagnetic fields. In combination, this leads to an electromagnetic shower, which covers a cluster of roughly 5×5 ECAL cells for particles of intermediate energies. Measuring this shower allows for estimation of the energy of the initial particle. An additional transverse momentum measurement from the tracker

is also possible for tracks of charged particles. Building these is initiated by superclusters (clusters of clusters) in the pixel detector and uses a Gaussian Sum Filter with a specific energy loss model.

While photons do not carry any charge, they tend to produce electron-positron pairs when under the influence of an atom's electric field. Electrons also radiate photons as they are subject to the Coulomb field of a nucleus, which are then again able to lead to pair production. As such, both types of objects produce a particle track until their energy has decreased sufficiently that they can be absorbed into the detector material.

Missing transverse energy is calculated from the vectorial sum of the transverse energies of all reconstructed objects. As one expects the initial state of a proton-proton collision to only have a negligible amount of transverse energy, the aforementioned sum should be zero. However, certain particles such as neutrinos or possibly new, yet unknown ones can escape the detector. The negative value of the vectorial sum is the collective estimate for all particles that avoided detection.

While most reconstruction algorithms work independently from one another to identify particle candidates, the **particle-flow** algorithm [36] reconstructs entire events. This means, that the tracks of every muon, electron, photon, as well as the charged and neutral hadrons are being taken into account when identifying particles. Consequently it is necessary to consider all sub-detectors and the information they provide. Overall, the expected performance for accurately identifying and reconstructing jets, taus and missing transverse energy is improved. Taking jets as an example, the components each jet consists of are reconstructed individually. Instead of approximating the shape through a cone, even the low energy fragments with diverging tracks can be assigned to the right jets. Taking all the information (that the algorithm considers) about nearby particles into account, an in-depth isolation criterion can be defined. This is particularly useful for muons used in this analysis.

Chapter 3

Signature of the Signal

As discussed in section 1.2.5, the model used in the analysis is R-parity violating supersymmetry. In particular, single coupling dominance for the lepton number violating coupling λ'_{211} is assumed. With a two quark initial state, the production of sleptons inevitably dominates other constellations. Taking into consideration how small the values of λ'_{211} have to be (Cf. fig. 1.11a & 1.11b), the primary decay modes for the slepton will be the R-parity *conserving* $\nu + \tilde{\chi}^{\pm}$ or $\mu + \tilde{\chi}^0$ processes. While the decay width for these modes are independent of λ'_{211} coupling, the competing R-parity *violating* dijet decay channel depends on it. With strict bounds of at least $\lambda'_{211} < 0.01$, the decay width of the R-parity conserving gaugino decay modes are two orders of magnitude larger than the R-parity violating one. As a result, they total decay width is mostly independent of the λ'_{211} parameter. Since the production cross section for smuons $\sigma_{\tilde{\mu}}$ and sneutrinos $\sigma_{\tilde{\nu}}$ scales quadratically with the matrix element, it is proportional to λ'^2_{211}. Consequently, the overall cross sections $\sigma(qq' \to \tilde{\mu} \to \mu\tilde{\chi}^0)$ and $\sigma(qq' \to \tilde{\nu} \to \nu\tilde{\chi}^{\pm})$ also have a quadratic dependence on λ'_{211} for values lower than 0.01.

The lightest neutralino is assumed to be the lightest supersymmetric particle (**LSP**), which is not considered to be stable in this analysis. Production and decay of both the chargino and heavier neutralinos can lead to additional jets or leptons, but will eventually lead to the lightest neutralino through the R-parity conserving modes[1] (Fig. 3.1).

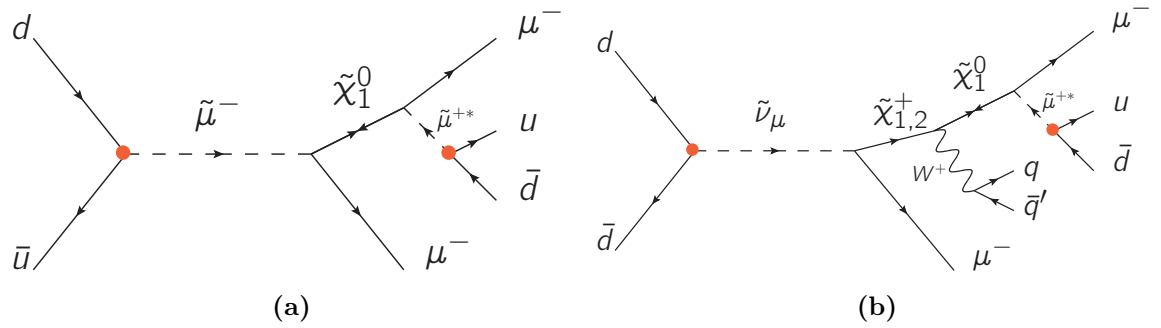

Figure 3.1.: Resonant production of a smuon (3.1a) and a sneutrino (3.1b) in R-parity violating supersymmetry. Shown are the most simple Feynman graphs leading to the two muon, two jets final state. The lepton number violating vertices are marked in red.

Since it is the LSP, it can only decay through the λ'_{211} coupling via a virtual smuon or

[1] The details of the decay modes depend on the mass hierarchy determined by the RPV cMSSM model parameters. The dependence on the universal mass parameters will be studied in the next section.

sneutrino. It should also be noted that the lifetime of the LSP depends on the coupling strength. For values $\lambda'_{211} > 10^{-6}$, the decay will be perceived as "prompt" by the detector. This means that both muons should originate from the same (primary) vertex. The decay of the LSP subsequently adds two jets, as well as either a muon or neutrino. With missing transverse energy from neutrinos being significantly less attractive than muon signatures, these final states are neglected.

This leaves two jets and a number of muons, ranging from zero to two, in every decay. Considering the production rates for the relevant backgrounds, one can see that two compositions are disfavoured. Colliding two hadrons yields a high amount of jets in every event, making the pure dijet channel without any muon the least promising. The very high W + jets background would interfere with a single muon and two jets search, leaving only the two muons, two jets option. Even here there are significant backgrounds to tackle, primarily the Drell-Yan process.

Taking a look at the simplest Feynman graphs for resonant smuon and sneutrino production and decay at the LHC (Fig. 3.1), one will notice a very useful attribute of their decay products. The electric charge of both muons are equally as likely to have the same sign as the opposite sign. This is due to the neutralino being a Majorana particle. Keeping the initial state of two protons in mind, primarily the ratio of u to d-quarks, the likelihood of positively charged muons is roughly twice the one for negatively charged ones. Since most Standard Model backgrounds are able to produce two opposite, but not two same sign muons, this feature of RPV supersymmetry can be exploited to discriminate against them. Major backgrounds, such as the aforementioned Drell-Yan processes or the production of top quark pairs, can be greatly reduced, enabling searches for new physics with low cross sections.

3.1. Monte Carlo Study

As Monte Carlo (**MC**) simulations are used for comparison to the measured data, the simulation of the signal for the 7 TeV CMS data taking period [20] can be used to derive further information about the signature. The production process of such a simulation will be outlined in section 4.3.1. Using the RPV supersymmetry model explained in section 1.2.5, a grid of simulated signal points with 50 k events each has been generated. While the scalar sparticle mass parameter m_0 runs from 100 to 2000 GeV in steps of 100 GeV and the mass parametr of fermionic sparticles $m_{1/2}$ runs from 50 to 1000 GeV in steps of 50 GeV, the remaining model parameters have the following fixed values:

$$A_0 = 0, \quad \tan\beta = 20, \quad \operatorname{sgn}\mu = +1, \quad \lambda'_{211} = 0.01$$

The cMSSM parameter values are inspired by the low mass benchmark points of CMS [37] and are chosen such, that small variations have little impact on the sparticle mass hierarchy and consequently the signature. Quantifying these "small variations" is difficult, as the sparticle masses do not just depend on one parameter. In general, changes of a few 100 GeV for A_0, around 10 for $\tan\beta$ and any sign of μ will result in the same mass hierarchy. The value of the R-parity violating coupling λ'_{211} is based on a rough estimate for the sensitvity of hadron colliders [18]. Because certain regions (low $m_{1/2}$, high m_0) in this parameter space lead to unphysical phenomena such as non-converging renormalization group equations, tachyonic solutions or no electroweak symmetry breaking, they are not being simulated. Excluding these points in the grid leaves an overall amount of 354 simulated phase space points (Cf. fig. 3.2).

Various decay scenarios are being investigated in this grid to determine their respective contribution to the signal signature. Two cases are considered. In the first one at least two muons and two jets are required (**MU2J2**). This yields signal events, but not all of them pass all analysis requirements. Only the second one demands all analysis requirements (from 2011 [20]) to be met (**ANA**). Major differences between the two are the same sign charge requirement and isolation criteria for muons. While it is important to know that the latter is tighter than the first, the details of all the requirements will be discussed in-depth in the event selection[2] (Cha. 6). Comparing both types of cases gives an idea of the effect of the analysis requirements on the signal.

To determine the overall efficiency of selecting signal events, the MU2J2 and ANA cases without any specific decay scenario are shown in figure 3.2.

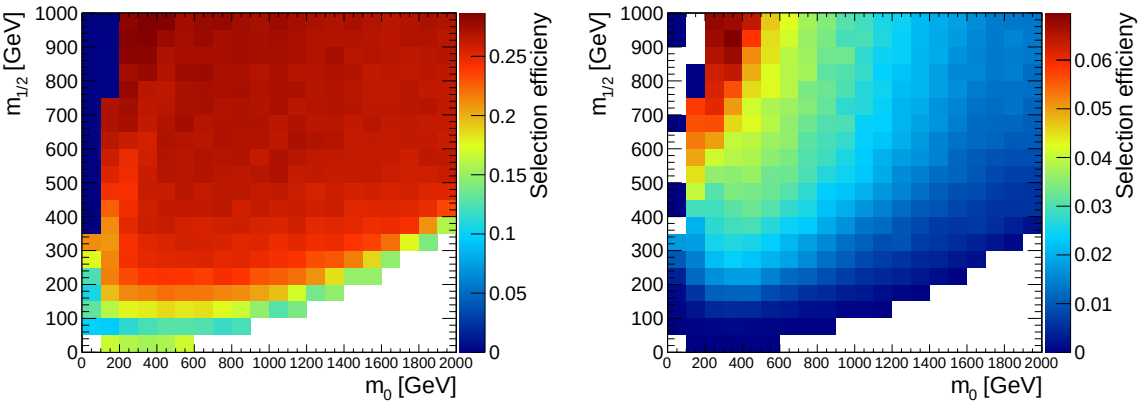

Figure 3.2.: Efficiency of selecting signal events in the MU2J2 (3.2a) and the ANA case (3.2b). Each bin represents a Monte-Carlo simulation of a RPV supersymmetry point normalized to the generated number of events.

Each bin shows the number of events meeting the requirements, normalized to the generated number of events. The white bins contain no events. This is either because no events passed the requirements, or they are within the previously mentioned low $m_{1/2}$, high m_0 parameter region with unphysical results. For high $m_{1/2}$, but low m_0 there are also disproportionally few events. The reason for this disparity lies within the supersymmetric mass spectrum. The lightest supersymmetric particle changes from the lightest neutralino to the stau $\tilde{\tau}$. As a result, the decay chains are altered, therefore rendering the analysis requirements insensitive.

Shifting the focus on the shape of the distribution, one will notice an almost flat efficiency of around 25 % above a certain ratio of $m_{1/2}$ to m_0 in the MU2J2 case. However, adding the ANA requirements leads to an efficiency decline from the $\sim 6\,\%$ high $m_{1/2}$, low m_0 region to either around or below 1 % for increasing m_0 and $m_{1/2}$, respectively. A significant portion of the drop in efficiency is expected when using the ANA case. As discussed in the previous section, the additional same sign charge requirement will half the selected amount of events already. Any further requirements will also have a negative impact on the efficiency, with the isolation criteria for the two muons being the main cause for the decline. If the neutralino masses are much lower than the smuon mass, which is roughly the case for ratios of m_0 to $m_{1/2}$ upwards of 2, it will naturally lead to boosted particles in the decay. Should these

[2] Although the event selection will concern itself with the 2012 requirements, they are comparable to the ones used in 2011.

decay products be too collimated, the isolation criteria will not be met and the event will be discarded. It should be noted that, as a result of different branching ratios in certain phase space regions, different processes can dominate the final state. Consequently the requirements of the ANA case cannot impact the entire phase space equally. Therefore the origin of the decline is always a combination of multiple quantities.

By demanding certain amounts of specific particles in a decay chain, it is possible to reconstruct the process of a selected event. This type of requirement will be referred to as an *effective branching ratio* (**EBR**)[3] To get an overview of the composition of processes leading to the signal signature, the particle count has been varied systematically. To reduce redundancy, only the primary produced sparticle as well as its supersymmetric decay products are used for process identification. Upon reaching the neutralino LSP in the cascade, the decay through the λ'_{211} coupling is always identical.

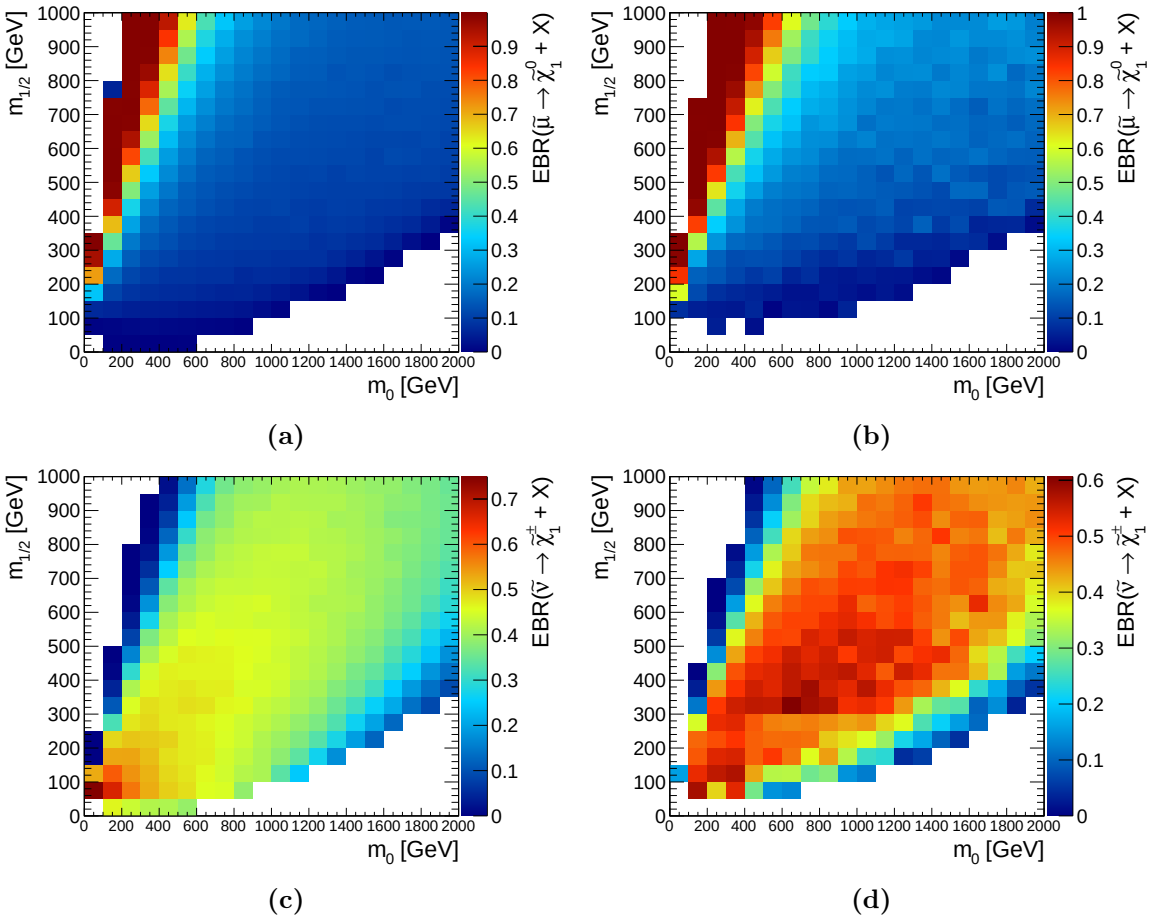

Figure 3.3.: Effective branching ratios of the $\tilde{\mu} \rightarrow \tilde{\chi}_1^0 + X$ (3.3a & 3.3b) and $\tilde{\nu} \rightarrow \tilde{\chi}_1^{\pm} + X$ (3.3c & 3.3d) processes. The EBRs are given by $N_{\text{evt}}(\text{Events including decay products of process})/N_{\text{evt}}(\text{All events for that bin})$ for each bin of the distribution in figure 3.2. On the left the MU2J2 case is shown, while one can see the ANA case on the right.

[3]Strictly speaking, these are not branching ratios, as it is a combination of multiple bra nching ratios and also depends on the production cross section.

As an example, figure 3.3 displays the contributions to the overall selection efficiency from figure 3.2 of the $\tilde{\mu} \to \tilde{\chi}_1^0 + X$ and $\tilde{\nu} \to \tilde{\chi}_1^\pm + X$ processes. The effective branching ratio is given by $N_{\text{evt}}(\text{Events including decay products of process})/N_{\text{evt}}(\text{All events for that bin})$ for the individual bins of the overall selection efficiency.

Combining the ERBs for these two processes already covers roughly 50% for most of the parameter space. An efficient way to compare all relevant processes at once, is a one dimensional distribution with either of the two universal mass parameters set to a fixed value. Since a larger variation can be observed over the simulated m_0 range (Cf. fig. 3.2 & 3.3), $m_{1/2}$ is kept constant.

Taking the empty bins into account (Cf. 3.2), 550 GeV as a value for $m_{1/2}$ provides a reasonable overview shown in figures 3.4c and 3.4d. To ensure a similar behaviour over the entire $m_{1/2}$ range, two variations with a 200 GeV difference in the value of $m_{1/2}$ are used for confirmation (Fig. 3.4a, 3.4b, 3.4e and 3.4f). With the grey colour marking the remaining contribution, only a negligible part of the total EBR is not covered by the listed processes. Initially, this statement would contradict the first bin of the MU2J2 case. However, since a *ratio* is being shown, this can be explained by the very low number of selected events in this region (Cf. 3.2). The ANA case supports this explanation, as none of the events pass its requirements.

As one would expect, for higher sfermion masses the contribution from processes with heavier sparticles increases. However the conclusion that can be drawn from these distributions, is that three processes dominate the signature of this analysis' signal. This is only enhanced by transitioning from the MU2J2, to the ANA case. The corresponding Feynman graphs for the three processes are given in figure 3.5.
As mentioned beforehand, after reaching the LSP through the cascade, the decay through the λ'_{211} leading to two jets and one muon is identical for every process. The simplest graph (Fig. 3.5a) has its biggest contribution of up to almost 100% in the low m_0 region. It then quickly loses importance and remains at a constant level around 20%. Both the other processes gain importance as the simple one loses it. Their contribution levels around 25% for the $\tilde{\mu} \to \tilde{\chi}_2^0$ and 45% for the $\tilde{\nu} \to \tilde{\chi}_1^\pm$ process for $500\,\text{GeV} < m_0 < 1600\,\text{GeV}$. Afterwards they decrease slowly.

This information can be used to allow for different interpretations of the results of this analysis. In addition to using the supersymmetric model, simplified models for the three Feynman graphs are an option. Since these types of models only focus on the physical parameters such as the particle mass and coupling strengths, it is easier to interpret these results for other models.

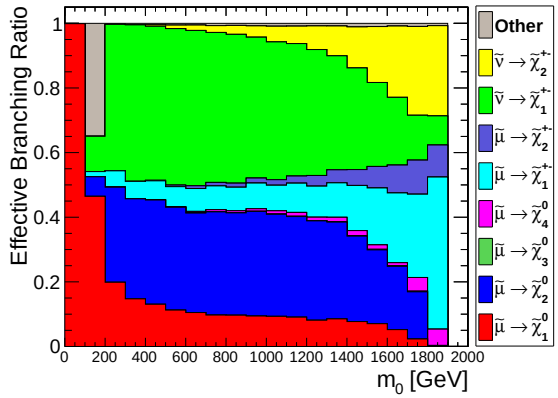

(a) $m_{1/2} = 350\,\mathrm{GeV}$

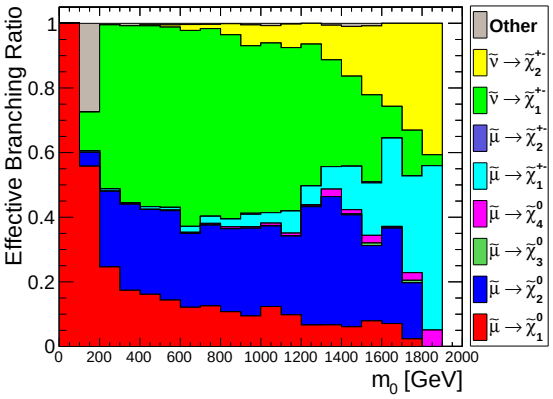

(b) $m_{1/2} = 350\,\mathrm{GeV}$

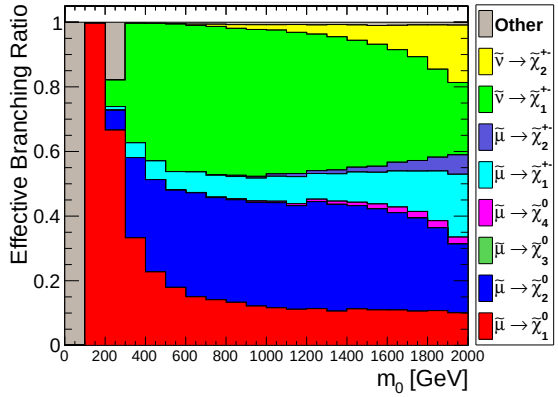

(c) $m_{1/2} = 550\,\mathrm{GeV}$

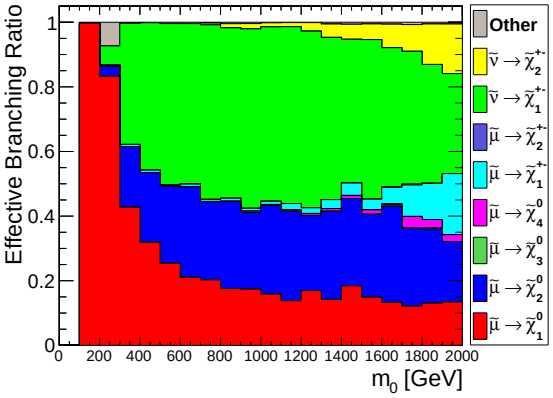

(d) $m_{1/2} = 550\,\mathrm{GeV}$

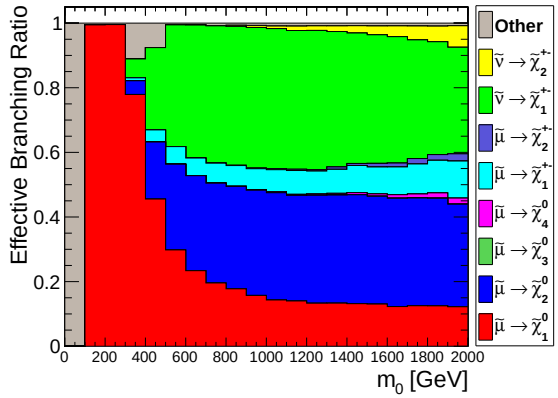

(e) $m_{1/2} = 750\,\mathrm{GeV}$

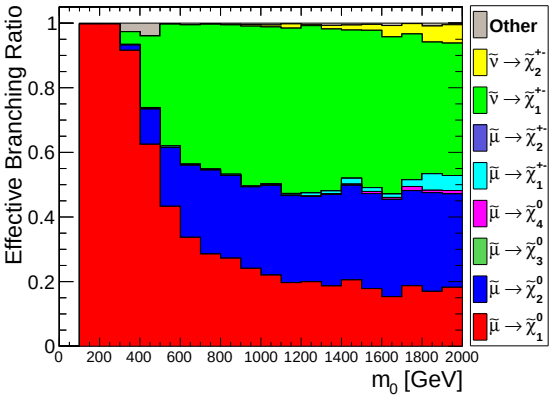

(f) $m_{1/2} = 750\,\mathrm{GeV}$

Figure 3.4.: Sum of all ERBs for the events from figure 3.2 for fixed values of $m_{1/2}$. All distributions on the left show the MU2J2 case, while the ANA case is given on the right side. Each color represents the ERB from a different process.

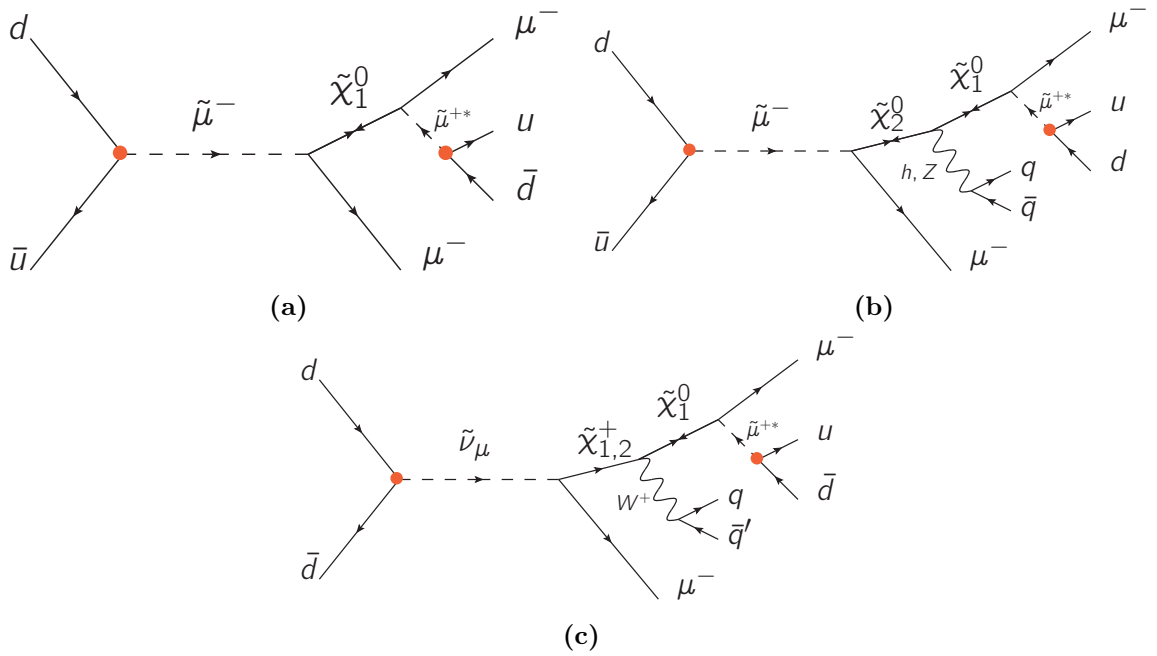

Figure 3.5.: Feynman graphs of the three dominant processes that lead to the signal signature. Each of the cascades leads to the neutralino LSP, which then decays through the λ'_{211} coupling, adding two jets and one muon to the final state.

Chapter 4

Software & Datasets

4.1. Analysis Software

With the signature of the signal determined, the necessary datasets for the analysis can be chosen. To access and work with these the CMSSW application framework [38] is used. Aside from providing the analysis tools, the collection of software also contributes to tasks like simulation, calibration, alignment and the event reconstruction. Due to a steady improvement in understanding the detector's and overall experiment's performance, an analysis is also dependent on the version of the CMSSW application framework. This analysis was performed using `CMSSW_5_3_9_patch1`.

Both the simulated and recorded data are stored in the following three data tiers:

- RAW - This particular format stores the digital information provided by the detector and its system of triggers.
- RECO - Derived from the RAW-format, the basic event reconstruction has been executed and its results are stored in this format.
- AOD - Building upon the basic reconstruction, the contents of this format are high level physics objects. This provides most conventional physics analyses, including this one, with the necessary information to base their work upon.

By selecting the desired dataset content, the overall size of files can be reduced. For this purpose the ACSUSYAnalysis framework and its skimmer [39] are used. This allows for local storage in the form of a tree structure provided by ROOT [40]. For further analyses and visualization a combination of ROOT version 5.32.00 and FindSusyB3 [41] are employed.

4.2. Data

The four data taking periods from 2012 will be subject of this analysis. The centre-of-mass energy for all of them is $\sqrt{s} = 8\,\text{TeV}$. Since two muons per event are a major part of the signature, the "DoubleMu" datasets are the most suitable ones, as they only contain events which activated at least one dimuon trigger. Table 4.1 lists the chosen datasets.

Dissecting the full name of a dataset gives different information about its contents. The first part, here DoubleMuParked, hints at the selected particle content. In this case, the *Parked* version superseded the usual DoubleMu datasets by adding an additional offline

Datasets	Run Range	$\int \mathcal{L} dt$ [pb^{-1}]
/DoubleMu/Run2012A-22Jan2013-v1/AOD[1]	190645 – 193621	876
/DoubleMuParked/Run2012B-22Jan2013-v1/AOD	193834 – 196531	4409
/DoubleMuParked/Run2012C-22Jan2013-v1/AOD	198049 – 203002	7017
/DoubleMuParked/Run2012D-22Jan2013-v1/AOD	203777 – 208686	7369
Σ	190645 – 208686	19671

Table 4.1.: Overview of the data recorded by the CMS experiment, which is used in this analysis.

trigger with a lower transverse momentum threshold. The second part of the name denotes the data taking period and the third one the date at which it was processed. Unless the latter contains "PromptReco", the data has since been reprocessed with improved knowledge of the detector, leading to more precise measurements. The datasets which are subject of this analysis are part of the Winter13 "ReReco", short for re-reconstruction. The data format, here "AOD", is given at the end.

In the second column, the run ranges are listed. Each run is composed of several lumi-sections with roughly equal duration. In the third column, the integrated luminosity for the individual run ranges is given. It is estimated from the average number $\langle n \rangle$ of pixel clusters occurring in the silicon pixel detector (Sec. 2.2.2) during an inelastic collision [42].

$$\mathcal{L} = \frac{\nu \langle n \rangle}{\sigma} \tag{4.1}$$

The frequency of bunch crossings is given by ν and σ denotes the visible cross section.

In general, only events from the certified list of properly reconstructed events Cert_190456-208686_8TeV_PromptReco_Collisions12_JSON.txt[2] are used. The integrated luminosity $\mathcal{L}$ of this list is 19712 pb^{-1}. Comparing it to the sum of all used DoubleMuParked datasets, only a minuscule amount of events ($\sim 0.2\%$) is not included in this analysis.

4.3. Simulation

As a general concept to differentiate between potential new physics and the standard model processes, this analysis compares the recorded data to simulation. By comparing simulated and measured distributions of observables, more accurately their expected number of events, the probability of a discovery or at least exclusion ranges can be given. Due to the nature of this method, having a precise prediction from the simulation is essential. There is a strong dependence on the knowledge of the relevant standard model processes.

To take the probabilities for the occurrence of the various processes into account, a Monte-Carlo method is used for the simulation. While they describe particle collision physics, the detector simulation is performed with GEANT4 [43, 44]. After simulating the triggers, the events can be reconstructed using the CMSSW application framework.

All Standard Model samples that can produce two muons and two jets are considered as

[1] The DoubleMuParked dataset from the 2012A period is not a superset of the DoubleMu dataset. As such, the DoubleMu dataset is being used, which yields an additional 3% events in the chosen final state.
[2] It is often called the "golden JSON" as it is saved in the java script object notation.
[3] $\hat{p}_T$ refers transverse momentum of the hard interaction.
[4] Pythia6 does not include W and Z bosons in the showering process, which is why additional $t\bar{t}+V$ samples are required. This also applies to the $\gamma \to \mu\mu$ decay in the W + jets $\to l\nu$ process.

Monte Carlo Sample	σ[pb^{-1}]	Weight
$Z/\gamma^* \to ll$ ($10\,\text{GeV} < m_{ll} < 50\,\text{GeV}$)	762	$1.25 \cdot 2.10$
$Z/\gamma^* \to ll$ ($50\,\text{GeV} < m_{ll}$)	$3.50 \cdot 10^3$ $\star\star$	$0.96 \cdot 2.26$
QCD $\mu_{p_T>5\,\text{GeV}}$-enr. ($15\,\text{GeV} < \hat{p}_T < 20\,\text{GeV}$)	$2.74 \cdot 10^6$	$31.3 \cdot 10^3$
QCD $\mu_{p_T>5\,\text{GeV}}$-enr. ($20\,\text{GeV} < \hat{p}_T{}^3 < 30\,\text{GeV}$)	$1.87 \cdot 10^6$	$4.32 \cdot 10^3$
QCD $\mu_{p_T>5\,\text{GeV}}$-enr. ($30\,\text{GeV} < \hat{p}_T < 50\,\text{GeV}$)	$8.06 \cdot 10^5$	$1.66 \cdot 10^3$
QCD $\mu_{p_T>5\,\text{GeV}}$-enr. ($50\,\text{GeV} < \hat{p}_T < 80\,\text{GeV}$)	$1.76 \cdot 10^5$	334
QCD $\mu_{p_T>5\,\text{GeV}}$-enr. ($80\,\text{GeV} < \hat{p}_T < 120\,\text{GeV}$)	$4.04 \cdot 10^4$	86.1
QCD $\mu_{p_T>5\,\text{GeV}}$-enr. ($120\,\text{GeV} < \hat{p}_T < 170\,\text{GeV}$)	$7.46 \cdot 10^3$	17.3
QCD $\mu_{p_T>5\,\text{GeV}}$-enr. ($170\,\text{GeV} < \hat{p}_T < 300\,\text{GeV}$)	$2.23 \cdot 10^3$	5.90
QCD $\mu_{p_T>5\,\text{GeV}}$-enr. ($300\,\text{GeV} < \hat{p}_T < 470\,\text{GeV}$)	151	0.381
QCD $\mu_{p_T>5\,\text{GeV}}$-enr. ($470\,\text{GeV} < \hat{p}_T < 600\,\text{GeV}$)	11.8	0.0613
QCD $\mu_{p_T>5\,\text{GeV}}$-enr. ($600\,\text{GeV} < \hat{p}_T < 800\,\text{GeV}$)	2.69	0.0128
QCD $\mu_{p_T>5\,\text{GeV}}$-enr. ($800\,\text{GeV} < \hat{p}_T < 1000\,\text{GeV}$)	0.369	0.0018
QCD $\mu_{p_T>5\,\text{GeV}}$-enr. ($1000\,\text{GeV} < \hat{p}_T$)	0.0849	0.0004
t^+ (s-channel)	3.79 ± 0.7 $\star\star\star$ [45]	0.532
t^- (s-channel)	1.76 ± 0.01 $\star\star\star$ [45]	0.133
t^+ (t-channel)	$56.4^{+2.1}_{-0.3}$ $\star\star\star$ [45]	0.573
t^- (t-channel)	30.7 ± 0.7 $\star\star\star$ [45]	6.05
t^+ (tW-channel)	11.1 ± 0.3 $\star\star\star$ [45]	0.555
t^- (tW-channel)	11.1 ± 0.3 $\star\star\star$ [45]	0.439
$t\bar{t}$ [4]	234^{+10}_{-9} $\star\star\star$	0.212
$t\bar{t} + W$	0.232 ± 0.067 $\star$	0.0210
$t\bar{t} + WW$	0.002037	0.0002
$t\bar{t} + Z$	$0.2057^{+0.019}_{-0.024}$	0.0193
$W + \text{jets} \to l + \nu$	$3.75 \cdot 10^4$ $\star\star$	12.8
$W + \gamma \to l + \nu + 2\mu$ [4]	1.91	0.126
$WW + \text{jets} \to 2l + 2\nu$	5.885 ± 0.396 $\star$	0.0599
$WZ + \text{jets} \to 2l + 2q$	2.293 ± 0.126 $\star$	0.0140
$WZ + \text{jets} \to 2q + l\nu$	7.495 ± 0.455 $\star$	0.0507
$WZ + \text{jets} \to 3l + \nu$	1.105 ± 0.066 $\star$	0.0108
$ZZ + \text{jets} \to 2l + 2\nu$	0.358 ± 0.019 $\star$	0.0074
$ZZ + \text{jets} \to 2l + 2q$	1.251 ± 0.065 $\star$	0.0127
$ZZ + \text{jets} \to 4l$	0.181 ± 0.009 $\star$	0.0007
WWW	$0.08068^{+4.7\,\%}_{-3.9\,\%}$ $\star$	0.0072
WWZ	$0.0580^{+5.6\,\%}_{-4.6\,\%}$ $\star$	0.0051
WZZ	$0.0197^{+6.0\,\%}_{-4.9\,\%}$ $\star$	0.0018
ZZZ	$0.00553^{+2.7\,\%}_{-2.4\,\%}$ $\star$	0.0005
W^-W^-	0.0889	0.0181
W^+W^+	0.248	0.0488
WW-DoubleParton	0.588	0.0139

Table 4.2.: List of all Monte Carlo samples that are considered as backgrounds for this analysis. Leading order cross sections are unmarked, while the stars indicate NLO ($\star$), NNLO($\star\star$) and approx. NNLO($\star\star\star$) calculations. Unless noted otherwise, the LO cross sections are taken from the generator output and the higher order ones including their scale uncertainties (if given) are from [46].

backgrounds for this analysis are given in table 4.2. The samples were generated during the "Summer12" period using PYTHIA6 [47] for QCD, POWHEG [48–50] for single and pair production of top-quarks and MADGRAPH [51] for most others. Details can be extracted from the sample paths, which are given in appendix A. In columns two and three, the cross section and weight of the specific processes are given. The latter is necessary to adjust the generated number of events for each sample to the expected amount for a given luminosity. Producing Monte Carlos samples individually for each analysis would not only be inefficient, but also very resource intensive. Instead most samples are produced centrally, which is also the reason why the generated and expected number of events cannot be matched. The formula for calculating the weight is

$$w = f \cdot \frac{\sigma \cdot \mathcal{L}_{\text{int}}}{N}. \tag{4.2}$$

The variable parameters are the cross section σ and the number of generated events N. The value for the integrated luminosity $\mathcal{L}_{\text{int}}$ is given by the $19.7\,\text{fb}^{-1}$ that is being used. An additional scaling factor f can be introduced to account for effects like higher order corrections to a cross section. It is only employed for the Drell-Yan processes and is listed in the weights column of table 4.2. The first factor of the product is f. The way these scaling factors are determined is described in an upcoming section (Sec. 6.5).

In all following distributions, groups of backgrounds are summarized under a single title to avoid cluttering. Table 4.3 lists the names which will be used.

Title	Monte Carlo Samples
Drell-Yan	Both $Z/\gamma^* \to ll$
QCD	All QCD samples
Single-top	$t^{\pm}$ s-, t- and tW-channels
$t\bar{t}$	$t\bar{t}$
$t\bar{t}+V$	$t\bar{t}+W$, $t\bar{t}+WW$ and $t\bar{t}+Z$
$W \to l\nu$	$W+\text{jets} \to l+\nu$
DiBoson	$W\gamma$ and all WW, WZ, ZZ decay modes
VVV	WWW, WWZ, WZZ and ZZZ
Rare Samples	W^-W^-, W^+W^+ and WW-DoubleParton

Table 4.3.: Arrangement of Monte Carlo titles in the distributions. Under each name on the left, the corresponding samples on the right are summarized.

The two Feynman graphs in figure 4.1 show the dominant background processes. Drell-Yan processes with two muons (Fig. 4.1a) are the prevalent background before applying the same sign charge requirement. The two lepton final state can provide two muons, although the charge cannot have the same sign. An additional amount of two jets can be produced through radiation of additional bosons or pileup interactions being misinterpreted. After applying the same sign charge requirement, top pair production (Fig. 4.1b) becomes the leading Standard Model process. Each top-quark is able to decay via the weak interaction, opening up the possibility of two prompt leptons. However, their charge cannot be equal. Since this analysis requires two prompt, well isolated muons, the ones passing the same sign charge requirement have to have misidentified or mismeasured muon. The likelihood for a muon to be a fake rises with the amount of hadronic activity. All Monte Carlo samples which contribute to the final state due to being dominated by QCD multijet events, will be used to estimate the amount of these contributions.

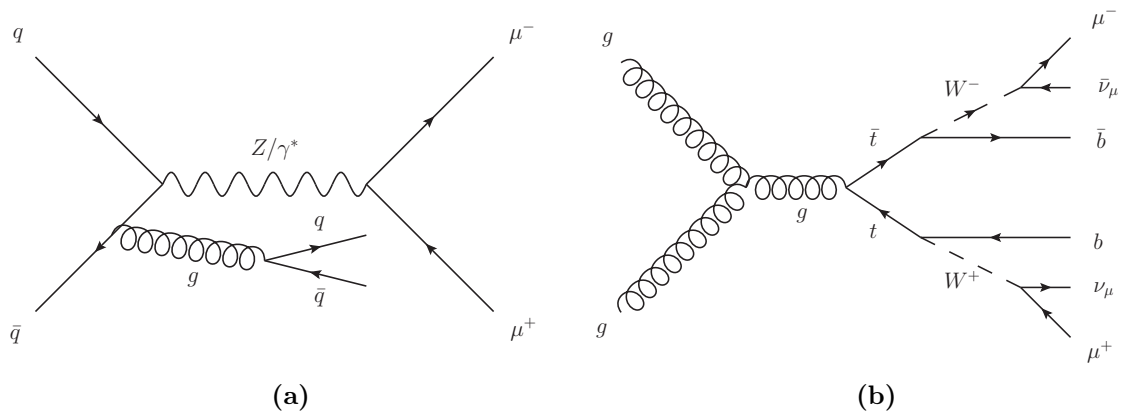

(a) **(b)**

Figure 4.1.: Drell-Yan (4.1a) and a $t\bar{t}$ (4.1b) feynman graph, which lead to a two muon and two jet signature. With their high cross sections, these two processes prove to be dominant Standard Model backgrounds for this analysis. However, they cannot produce two prompt, same sign charge muons.

4.3.1. Signal Simulation

While the previous section covers the simulation of the standard model background, it is also necessary to generate the supersymmetric model including the signal. In addition to the backgrounds, the simulation of the signal is used to estimate the likelihood of the measurement being described by supersymmetric processes.

To cover a variety of R-parity violating constrained MSSM scenarios, the m_0-$m_{1/2}$-phase space is subdivided into a grid. The SUSY mass spectra for each point in said grid are generated with SoftSusy 3.3.5 [52, 53] using the following parameters. The universal mass of scalar particles m_0 is increased from 100 GeV to 2500 GeV and the universal mass of fermonic ones $m_{1/2}$ from 100 GeV to 1500 GeV. The size of each step is 100 GeV for both variables. All remaining parameters are constant throughout the entire grid and are chosen to be

$$A_0 = 0, \quad \tan\beta = 20, \quad \operatorname{sgn}\mu = +1, \quad \lambda'_{211} = 0.01. \tag{4.3}$$

As previously discussed (Cha. 3), certain points in the parameter space do not favour the chosen signal signature while others do yield unphysical results. The former is strictly due the $\tilde{\tau}$-LSP configuration in the high $m_{1/2}$, low m_0 region, while the latter has three different reasons. Low values for $m_{1/2}$ and high ones m_0 can lead to no electroweak symmetry breaking, non-converging renormalization group equations or the production of tachyons. When generating the mass spectra, all of these scenarios are being excluded before the production. Overall, this leaves 287 valid points.

To actually produce the events, the leading order matrix element generator CalcHep 3.4 [54] is being employed. Generated events are processed with the *full* CMS detector simulation using the `CMSSW_5_3_9_patch1` framework. The path to the batch file containing all signal samples is also given in appendix A. Running the full simulation on the entire grid of parameter points with sufficient statistics for each sample is resource intensive. Therefore a filter is applied at generator level (i.e. before parton showering and simulation) removing events that do not contain at least two muons. They have to pass a transverse momentum threshold of 10 GeV for the leading muon and 5 GeV for the sub leading one. These require-

ments are chosen such that they are well below the `HLT_Mu17_TkMu8` trigger threshold of 17 GeV and 8 GeV for the leading and sub-leading muon, respectively. This filter does not necessitate two muons after the simulation and reconstruction.

In order to increase the accuracy of the CalcHep simulation, k-factors are determined as the ratio of a next-to leading order to a leading order cross section calculation. The source code for the NLO calculation is documented in reference [55]. They are then applied to the value provided by CalcHep. The branching fractions for the production of the smuon and sneutrino have to be kept in mind. Both the evolution of the smuon's cross section as well as the of k-factor are shown in figure 4.2.

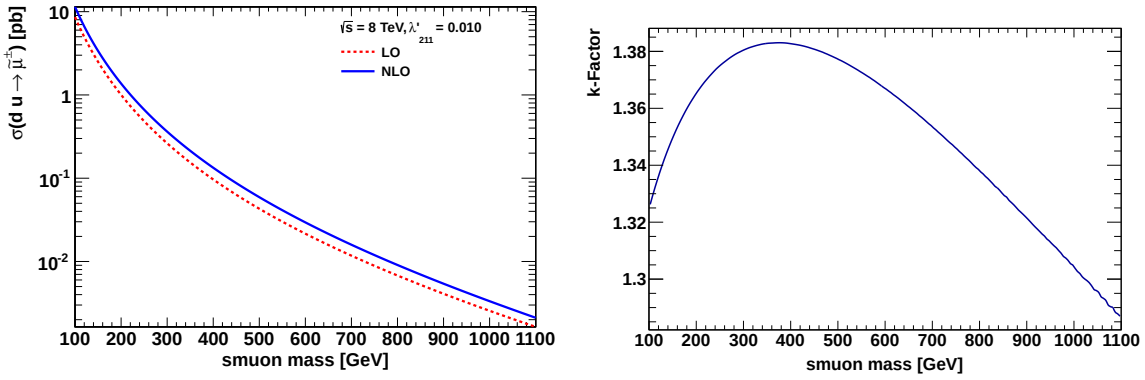

(a) (b)

Figure 4.2.: Cross section for the production of smuons via λ'_{211} (4.2a) and the k-factor for their cross section (4.2b). The latter is the ratio of the LO and NLO cross section with respect to the smuons production rate.

Applying the k-factors to the CalcHep output, with respect to the production rate of the smuon and sneutrino, yields the map of next-to leading orders cross sections used in the analysis. This map is shown in figure 4.3.

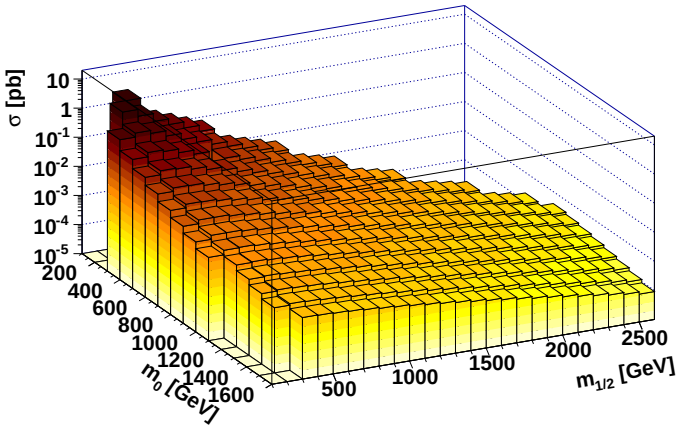

Figure 4.3.: NLO cross section map for the production of second generation sleptons used in the analysis. The *production* branching fractions of both the smuon and sneutrino have been taking into account for the calculation.

For comparison, three points of the cMSSM parameter phase space will be shown in most

of the upcoming distributions. The $m_0 = 300\,\text{GeV}$, $m_{1/2} = 300\,\text{GeV}$ and $m_0 = 1000\,\text{GeV}$, $m_{1/2} = 200\,\text{GeV}$, as well as the $m_0 = 1000\,\text{GeV}$, $m_0 = 1200\,\text{GeV}$ scenario. While the first two are within the range of existing limits (Sec. 1.2.5), the latter is not. As the corresponding cross sections scale with λ'^2_{211}, the cross section of the first two scenarios are adjusted to match existing limits. Exemplary distributions displaying the different properties of the signal points are shown in figure 4.4. Large differences between the distributions of the generated points in phase space can be seen. This is especially apparent in the two muon mass resonances for the smuon and sneutrino While this is expected, it leads to differing efficiencies with regards to certain requirements that are going to be applied in chapter 6.

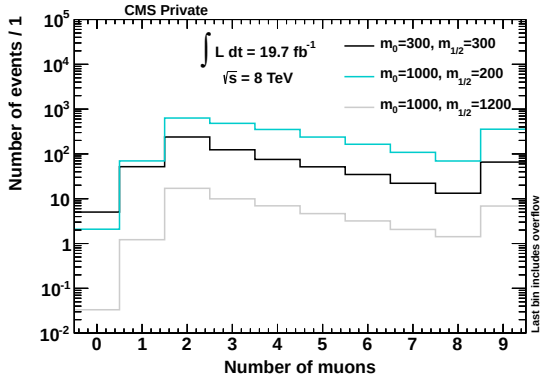

(a) Number of *reconstructed* muons. $p_{\text{T,1st}\mu} > 10\,\text{GeV}$, $p_{\text{T,st}\mu} > 5\,\text{GeV}$. No further requirements applied.

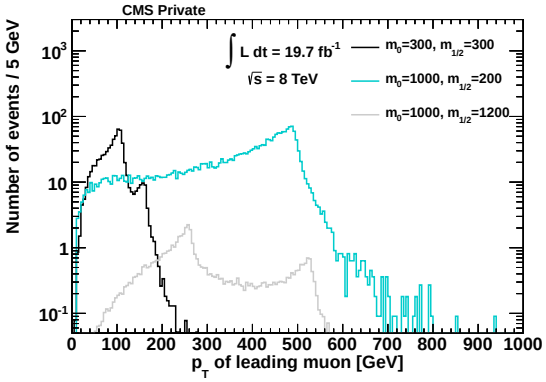

(b) Transverse momentum of leading muon, $p_{\text{T,1st}\mu} > 10\,\text{GeV}$. Structures are caused by the smuon and sneutrino[3].

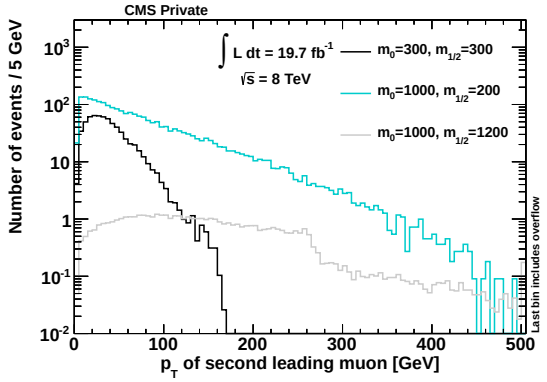

(c) Transverse momentum of sub-leading muon, $p_{\text{T,st}\mu} > 5\,\text{GeV}$.

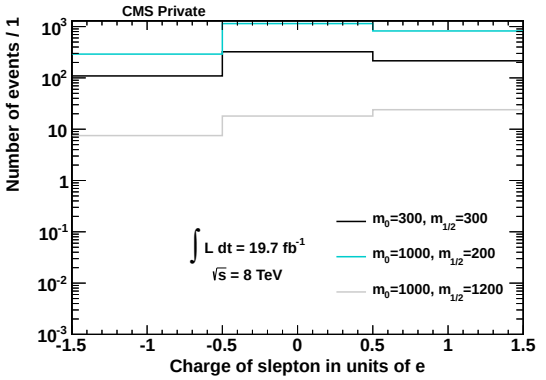

(d) Charge of slepton.

Figure 4.4.: Selected properties of the signal Monte Carlo after simulation and reconstruction. For 4.4a all events passing the generator level filter are included, while for the remaining distributions at least 2 muons and 2 jets per event are required.

[3] In the $m_0 = 1000\,\text{GeV}$, $m_0 = 1200\,\text{GeV}$ case, the smuon and sneutrino mass coincide at $m_{\tilde{\nu}} \approx m_{\tilde{\mu}} = 1272\,\text{GeV}$.

4.4. Pileup Reweighting

During 2012 the average number of proton-proton collisions that occured for a single bunch-crossing is 21 [24]. The distribution for said data taking period is shown in figure 4.5a. However, for the generated Monte Carlo samples the shape differs. Accommodating for that fact is an important step to allow for an accurate simulation of the experiment's conditions.

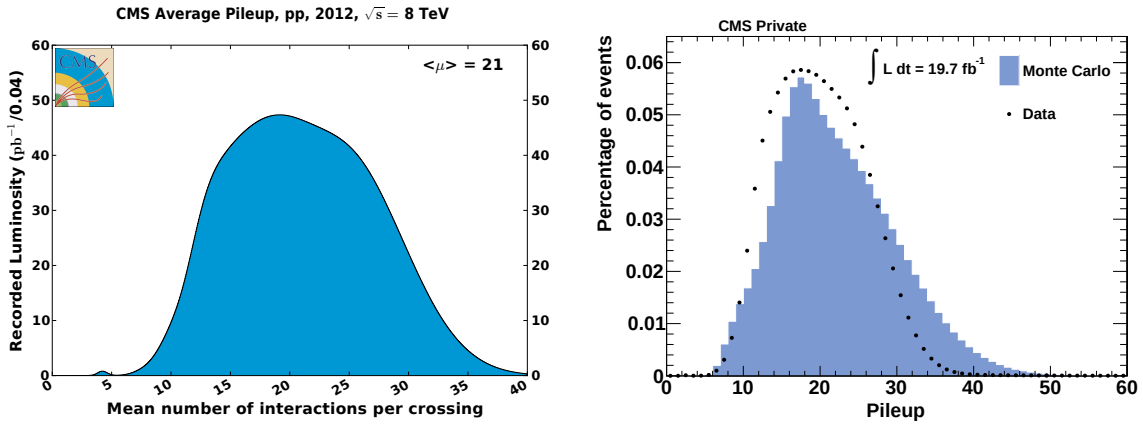

(a) (b)

Figure 4.5.: Pileup distribution for the 2012 data taking period (4.5a) [24] and normalized pileup reweighting distribution (4.5b).

To obtain the (true) number of interactions for each crossing, the instantaneous bunch-by-bunch luminosities are used as input. Combined with the total inelastic cross section, which amounts to 69400 μb at 8 TeV [56], they can be used to calculate the aforementioned expected number of interactions for each lumisection. While said cross section is entered manually into the script, the luminosities are extracted from a centrally maintained pileup file. In this analysis `pileup_JSON_DCSONLY_190389-208686_All_2012_pixelcorr.txt` has been used, which already includes corrections from the information provided by the pixel detector. Figure 4.5a shows the histogram filled with the expected number of interactions for the 2012 data taking period. Complementary, figure 4.5b shows the normalized distribution with the corresponding Monte Carlo entries. These bin contents for the simulated samples have also been gathered centrally and are taken from the dedicated TWiki website [57]. All samples in question have been produced with the Summer12 S10 scenario (c.f. app. A).

From the ratio of each bin a weight can be calculated and applied to the MC samples on an event by event basis for the analysis. Figure 4.6 provides a visualization of the effect of the reweighting.

The distributions are from an early stage of the analysis, where nothing but the correct trigger (Sec. 5.1) and two muons with $p_{\mathrm{T},\,1\mathrm{st}\,\mu} > 10\,\mathrm{GeV}$ are required. They show the number of vertices before (Fig. 4.6a) and after (Fig. 4.6b) the introduction of the weights. With such low requirements and consequently high statistics, the demonstrated improvement is displayed at its greatest impact. Additionally, this is also where the weights are introduced in the analysis. It is important to note that data and simulation are not expected to be in good agreement yet, as showcased by the discrepancies for large numbers of vertices. Nonetheless the histograms display the necessity of this procedure.

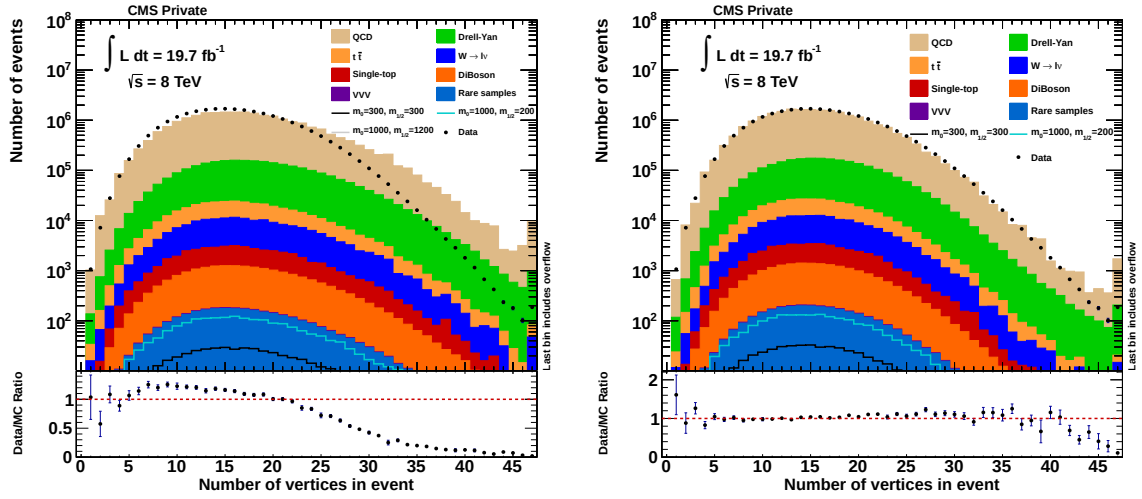

(a) (b)

Figure 4.6.: Number of vertices with (4.6b) and without (4.6a) pile-up corrections applied to the MC. At this stage of the analysis nothing but the correct trigger (Sec. 5.1) and two muons with $p_{\mathrm{T},\ 1\mathrm{st}\ \mu} > 10\,\mathrm{GeV}$ are required.

4.5. Jet Energy Resolution

With two jets and no missing transverse energy in the final state, the hadronic calorimeter contributes vital information. However, similarly to the pileup situation, the conditions of the simulation differ from the actual measurement. The energy resolution of the calorimeter is known to be estimated to be too good in the detector simulation [58]. To gain access to the resolution, the objects after the simulation stage can be compared to the generator-level ones. Based on this information and the set of measurements the necessary scale factor can be determined.

Every reconstructed particle flow jet above 15 GeV transverse momentum is considered relevant for the analysis. The algorithm searches for generator-level (**gen-**) jets in a cone of $\Delta R = \sqrt{\Delta\phi^2 + \Delta\eta^2} = 0.5$ in spatial distance around each reconstructed (**reco-**) jet. Depending on whether or not any matching objects are found, one of the following two recipes for adjusting the reconstructed jet energy resolution (**JER**) are used.

Matched gen-jets: In case there are matching gen-jets, the formula used to smear the jet energy is given by:

$$p'_{\mathrm{T}} = p_{\mathrm{T,GEN}} + c \cdot (p_{\mathrm{T}} - p_{\mathrm{T,GEN}}) \tag{4.4}$$

The transverse momentum p_{T} is replaced by a new value p'_{T}, based on the generator information for the transverse momentum $p_{\mathrm{T},\ \mathrm{GEN}}$. Here c denotes the core resolution scaling factors. To determine those, $0.8\,\mathrm{fb}^{-1}$ of 2011 dijet data[4] have been used [58]. The values are given in table 4.4.

No matched gen-jets: Without a gen-jet match, the jet energy resolution cannot be estimated. Following the official recommendations [58], one can instead randomly smear the *reconstructed* transverse momentum of the jet. The values are assumed to follow a Gaussian distribution with a width of $\sigma = \sqrt{c^2 - 1} \cdot \sigma_{\mathrm{MC}}$. The core resolution scaling factors c remain

[4] No significant deviations have been observed with more statistics and 2012 data

η-Range	Ratio of data/MC $\pm$ stat. $\pm$ sys.
$0.0 < \|\eta\| < 0.5$	$1.052 \pm 0.012^{+0.062}_{-0.061}$
$0.5 < \|\eta\| < 1.1$	$1.057 \pm 0.012^{+0.056}_{-0.055}$
$1.1 < \|\eta\| < 1.7$	$1.096 \pm 0.017^{+0.063}_{-0.062}$
$1.7 < \|\eta\| < 2.3$	$1.134 \pm 0.035^{+0.087}_{-0.085}$
$2.3 < \|\eta\| < 5.0$	$1.288 \pm 0.127^{+0.155}_{-0.153}$

Table 4.4.: Core resolution scaling factors c as used for jet energy smearing. They are taken from the JER TWiki [58].

the same, but the energy resolution of jets σ_{MC} has to be derived from the Monte Carlo samples. In figure 4.7 the difference between the transverse momentum of matched reco- and gen-jets is shown.

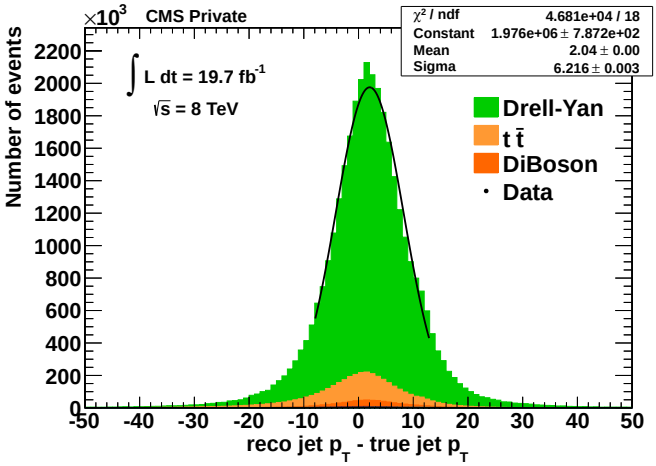

Figure 4.7.: Difference of transverse momenta from matched reco- and gen-jets in a $\Delta R = 0.5$ cone. This is used to determine the jet energy resolution in the Monte Carlo samples. This histogram is generated after applying the muon quality criteria (Sec. 6.4), with the analysis being re-run with its result.

Determining the width of this distribution yields the energy resolution. The entire distribution cannot be accurately modeled with a Gaussian function, however the width of the peak is reasonably well described. It yields $\sigma_{\mathrm{MC}} = 6.2\,\mathrm{GeV}$ a negligible statistical error. While this distribution does depend slighty on the transverse momentum and η of the jet, the resolution of the majority of jets is well described by this value. Variations of σ_{MC} have shown an impact of less than 1 % on the final distribution. The p_{T} and η dependence, as well the systematic uncertainty of the fit due to the shape are taken into account in the dedicated systematics section (Sec. 8.1.1).

The correction to the transverse momenta is propagated to the x and y momenta, energy and the missing transverse energy measurements. In figure 4.8 the particle flow missing transverse energy is shown with and without the correction. Due to the adjustment being expected to be comparatively small, the histogram has been filled before the missing transverse energy requirement (Sec. 6.7) of the analysis. This ensures a reasonable agreement between data and simulation prior to examining the effect of the jet energy resolution.

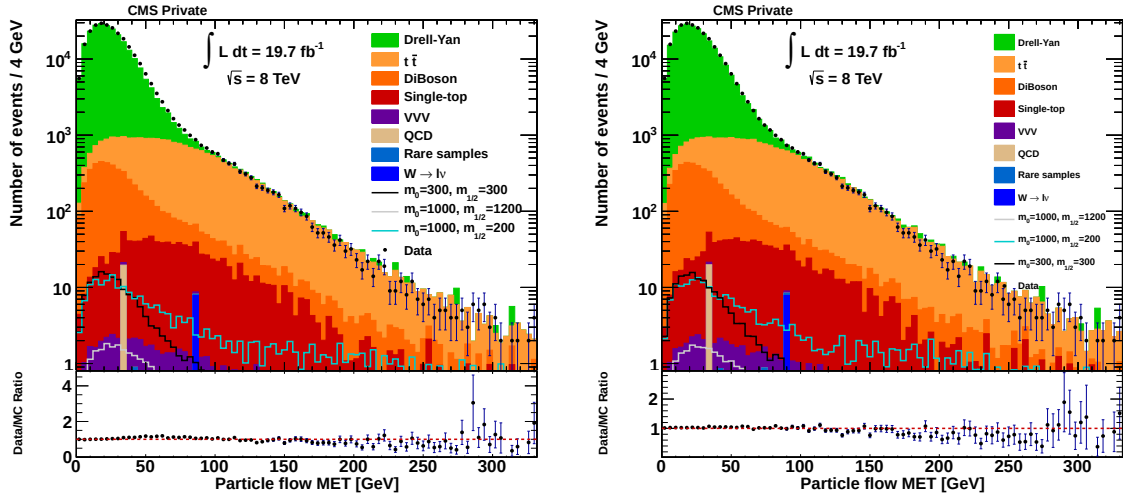

(a) (b)

Figure 4.8.: Particle flow missing transverse energy with (4.8b) and without jet energy corrections (4.8a). Both distributions are composed before the missing transverse energy requirement (Sec. 6.7).

One can observe a small, but still noticeable improvement due to the correction. This is best visible on the right flank of the distribution, where the Drell-Yan process still dominates and the size of the MET is dominated by its resolution rather than by true MET due to undetected neutrinos.

Chapter 5

Object Selection

Choosing recipes for selecting well reconstructed physics objects is necessary before one is able to apply analysis requirements. Their general task is to reduce the number of false reconstructions. For example a hadron can "punch through" the HCAL and leave a track in the muon system. This might then be falsely identified as a muon and interfere with the signal. These recipes for object identification (**ID**) have been developed by the respective physics object groups (**POG**) of the CMS collaboration. In this chapter, the various steps in the decision of deeming an object valid or invalid will be given.

5.1. Triggers

Before selecting physics objects, a trigger has to be chosen. Although DoubleMu datasets already necessitate dimuon triggers, only a selected few are well suited for the specified signature. A primary concern is a low trigger prescale. Prescaling means that the amount of events passing the trigger is suppressed by a certain factor to control its rate (and the amount of data manageable). To be able to allow for a low prescale factor, the requirements for each trigger have to be strict enough. Usually the transverse momentum threshold for the object can be raised to ensure an acceptable rate of events, but keeping the essentially prompt decay in mind, another option is available. Various triggers have a $|\Delta z_{\mu\mu}| < 0.2\,\text{cm}$ requirement, filtering out events with a large distance in the z-direction between the muon-pair. This effectively enables the inclusion of the low momentum regions in the search. The remaining options for high level triggers are:

- `HLT_Mu17_Mu8`
- `HLT_Mu17_TkMu8`

Both have an HLT prescale of 1 and are the triggers with the lowest available transverse momentum threshold of 17 GeV and 8 GeV for the leading and sub-leading muon, respectively. With an identical requirement for the primary muon, the major difference is the reconstruction of the second muon. The first trigger path requires both muons to be global ones, while in the other path the second muon only needs to be a tracker muon. As already discussed in the object reconstruction (Sec. 2.2.7), the latter can allow events with two collimated muons to pass which would otherwise be discarded.

To quantify the difference between both triggers, the number of selected events can be compared. In figure 5.1 the number of data events passing various combinations of the two triggers are shown.

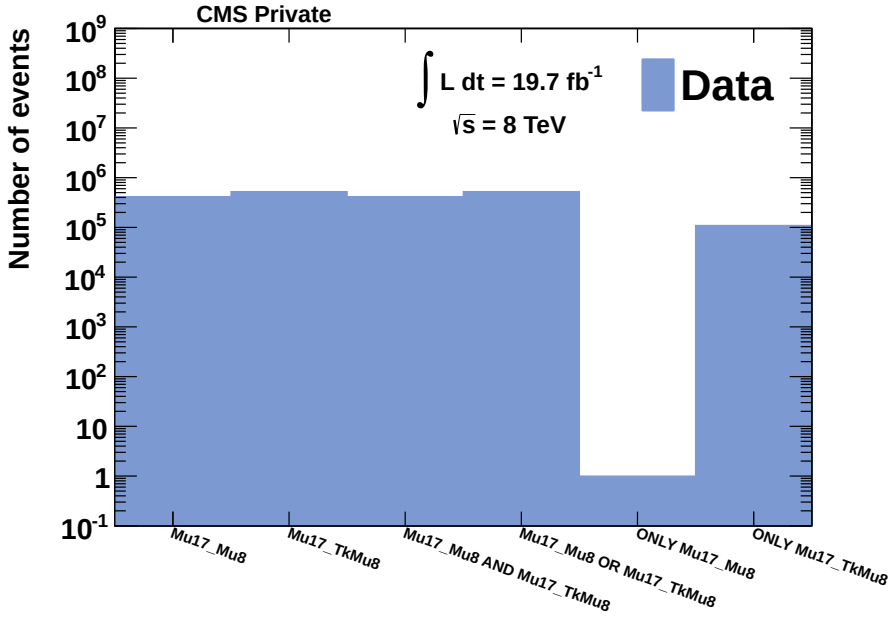

Figure 5.1.: Each bin represents the number of data events passing the various trigger combinations given on the x-axis. All four runs of 2012 (Tab. 4.1) are included in this distribution. The histogram is generated after the invariant dimuon mass requirement (Sec. 6.6).

The first two bins of the distribution show the results for each individual trigger. By raw numbers, `HLT_Mu17_TkMu8` is in the lead in terms of overall efficiency. To get en estimate of the overlap, the third bin shows the case when both triggers are required at once. With the number of events being quite similar to the one for `HLT_Mu17_Mu8`, one can conclude that almost all events in the first bin are contained in the second one as well. Complementary, the fourth bin displays the case where either of the two triggers was active. The number of events appears to be roughly equal to the one of the second bin, which supports the previous conclusion. To further quantify this statement, the fifth and sixth bin display the event count of *only* one out of the two being triggered. Comparing the contents of these bins with the previous ones, the additional efficiency yielded by using `HLT_Mu17_Mu8` in addition to `HLT_Mu17_TkMu8` can be estimated. With it being only of the order of $\mathcal{O}(10^{-5})$, this analysis uses the latter trigger exclusively.

5.2. Muon Identification

The recipe employed for muon identification has been developed by the Muon POG. The current recommendations can be found on the respective TWiki Website [59]. Its main purpose is to differentiate between prompt and non-prompt muons.

Since the analysis expects a low amount of statistics in the final distributions, the tight muon ID [31, 60] has been chosen. This is the most strict criterion given by the physics object group, thus being the best choice to prevent misidentification, but it comes at the cost of having the lowest selection efficiency. The requirements are given below and apply to all muons within the intermediate energy range.

- **Global Muon** - The object is required to be identified as global muon. As discussed in the object reconstruction (Sec. 2.2.7), this means that a set of hits in the muon system

has to be matched to a compatible set in the tracker. Since the majority of particles do not leave many hits in the muon system or are stopped before even reaching it, this is an efficient tool to distinguish muons from them.

- **Particle Flow Muon** - As outlined in the object reconstruction, the particle flow algorithm considers the measurements from all sub-detectors. By combining the information of an entire event, the accuracy of particle identification is improved.
- **Muon Track $\chi^2/N_{dof} < 10$** - The fit of the trajectory has to describe the hits reasonably well. This is meant to protect against muons stemming from a decay in flight, as well as hadrons passing the HCAL [61]. In both cases the trajectory is likely not to have a good match in the tracker region.
- **$N_{\text{Matched Stations}} > 1$** - Requiring at least two muon stations to have a muon segment hit provides consistency with the trigger[1]. Once again, this aids against punch-through particles and also against general mismatches of tracks.
- **$|d_{xy}| < 2\,\text{mm}$** - The impact parameter in the transverse plane, in respect to the primary vertex[2], has to be small. Both decays in flight and cosmic muons are unlikely to meet this criterion [61].
- **$|d_z| < 5\,\text{mm}$** - The longitudinal distance towards the primary vertex also has to be low for the same reasons.
- **$N_{\text{Pixel Hits}} > 0$** - Since in flight decays may not have hits in the pixel detector, this requirement provides further suppression and association to a single vertex.
- **$N_{\text{Tracker Layers}} > 5$** - A certain amount of tracker CSC layers needs to be hit for a precise transverse momentum measurement. Additionally, the same logic as for the hits in the pixel detector applies.

The detector coverage only ensures a consistent momentum resolution for muons in the η-region up to 2.1 (Cf. cha. 2), with respect to the nominal cross. Hence the analysis limits itself to this region, which also avoids the additional noise for increasing values of η. Together with a minimum transverse momentum set by the trigger, these are the basic criteria for object selection with regards to muons. They will be used and expanded upon in the event selection (Sec. 6).

Additional distributions displaying the effects of the individual ID criteria can be seen in figure 5.2. To be able to visualize the individual impact of a requirement from a given recipe, the histogram is only filled with events passing all of the recipe's requirements excluding the one to be examined. These so-called "N−1 plots" show the parameter regions which are *only* excluded because of the requirement in question.

5.3. Jet & Missing Transverse Energy Identification

For selecting jets and missing transverse energy, this analysis relies on the work of the JetMET POG [62]. Jets are reconstructed using the anti-k_T ($R < 0.5$) and particle flow algorithm.

[1] A reasonable estimate for the transverse momentum requires a minimum of three hits. Without a well reconstructed transverse momentum, the trigger threshold becomes meaningless as it is based upon that.

[2] The primary vertex is defined as the vertex with the largest sum of squared transverse track momenta in an event.

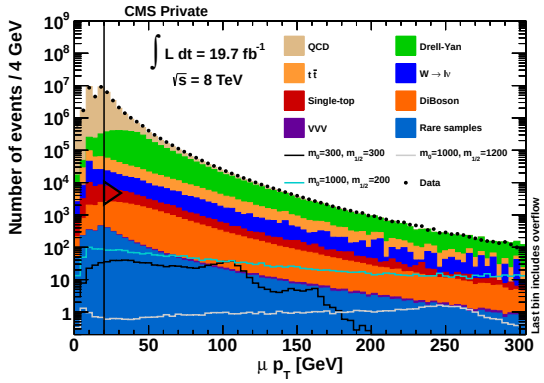

(a) Transverse momentum of muons.

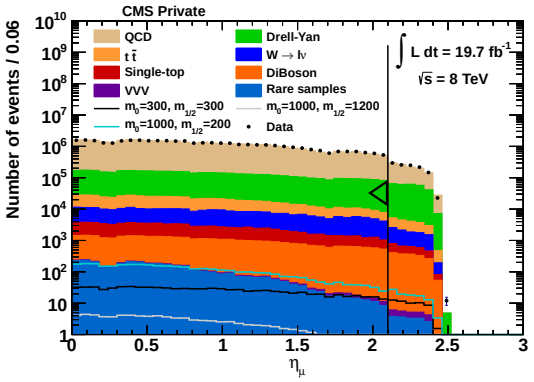

(b) η of muons.

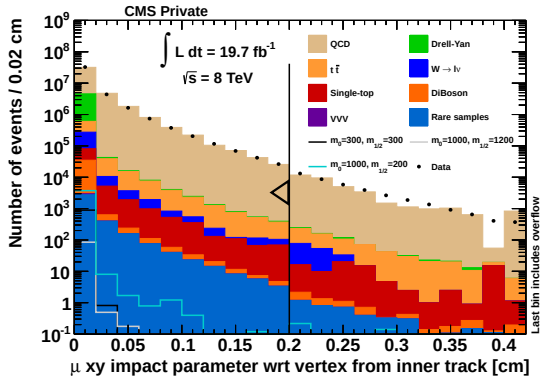

(c) Transverse impact parameter of muons.

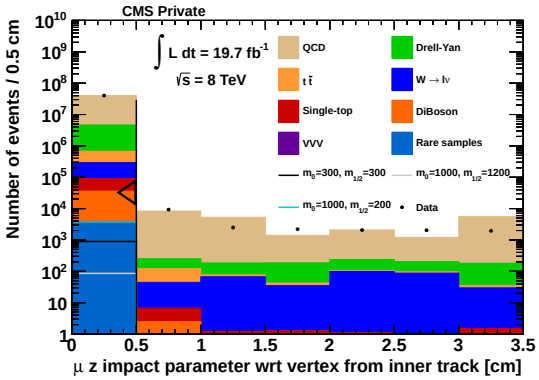

(d) Longitudinal impact parameter of muons.

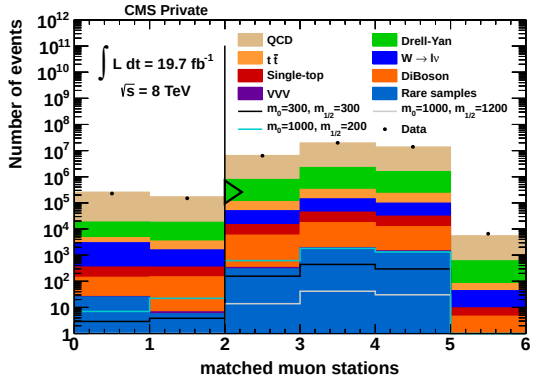

(e) Number of muon stations matched by each muon.

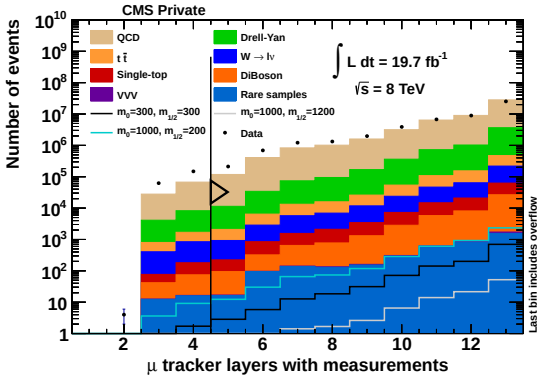

(f) Number of muon tracker layers matched by each muon.

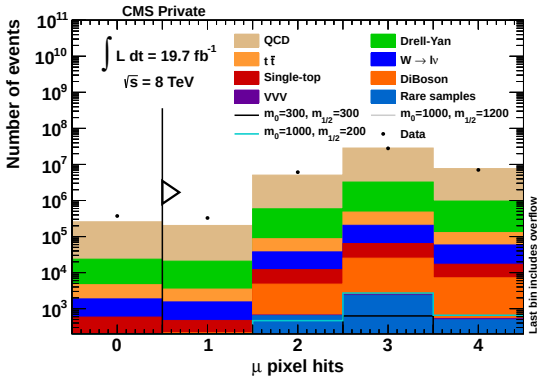

(g) Number of valid hits in the pixel detector by muons.

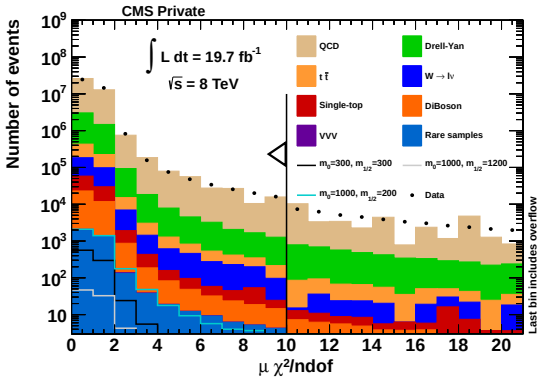

(h) χ^2 value of the track fitting procedure for muons.

Figure 5.2.: $n-1$ distributions of the muon object selection, where only the right trigger is required. Requirements are indicated by arrows.

The latter is also responsible for the calculation of the missing transverse energy. The recommended loose working point [63, 64] has been chosen with regards to jet requirements. The idea is to support the event selection which uses muons as its basis, while giving confidence for the final state selection. The values are given below.

- **Number Of Constitutents > 1** - Amount of particle components of the jet.
- **Neutral Hadron Fraction < 0.99** - Fraction of the energy deposited in the HCAL by neutral particles.
- **Charged Hadron Fraction > 0** - Fraction of the energy deposited in the HCAL by charged particles.
- **Neutral EM Fraction < 0.99** - Fraction of the energy deposited in the ECAL by neutral particles.
- **Charged EM Fraction < 0.99** - Fraction of the energy deposited in the ECAL by charged particles.
- **Charged Multiplicity > 0** - Number of charged jet components.

For the transverse momentum threshold and spatial coverage 15 GeV and $|\eta| < 2.4$ are required. A spatial distance of at least $\Delta R > 0.05$ to a selected muon is being ensured as well. This is meant to prevent valid muons from being misreconstructed as particle flow jets.

5.4. Electron Identification

For selecting electrons, the Egamma POG recommendations are employed. These are taken from and can be found on yet another TWiki Website [65]. Since electron identification is only used for vetoing against potentially misreconstructed events, they are of lower importance compared to the previously discussed physics objects. As a single electron can lead to multiple entries in the calorimeter, superclusters (**SC**) are used to describe an η-region of ECAL entries triggered by an electron. Due to the electron's trajectory being bent, the electron

emits photons resulting in these additional hits in the adjacent ECAL cells. If an electron hits the border of adjacent cells, it also yields multiple entries. The chosen medium working point has the following requirements for the barrel (encaps) region.

- $\mathbf{\Delta\eta_{SC} < 0.004(0.007)}$ - η-distance of extrapolated track to supercluster.
- $\mathbf{\Delta\phi_{SC} < 0.06(0.03)}$ - ϕ-distance of extrapolated track to supercluster.
- $\sigma_{\eta\text{Energy spread}} < \mathbf{0.01(0.03)}$ - Size of the energy spread of the supercluster. It is calculated from the distance $\Delta\eta$ of the adjacent $5times5$ ECAL cells around the seeding crystal. Each distance is weighted with the energy deposited in the respective cell. This quantity is also known as $\sigma_{I\eta I\eta}$.
- $\mathbf{H/E < 0.12(0.10)}$ - Ratio of ECAL and HCAL energy measurements. Electrons are expected to deposit most of their energy in the ECAL, hence this ratio is expected to be low.
- $\mathbf{|d_{0,vtx}| < 0.02}$ - Transverse distance to primary vertex.
- $\mathbf{|d_{z,vtx}| < 0.1}$ - Longitudinal distance to primary vertex.
- $\mathbf{|1/E - 1/p| < 0.05}$ - Absolute difference of the inverse energy and momentum. Due to the electron being light, both the energy and momentum are expected to be very close, which is exploited here.
- $\mathbf{\text{Combined } I_{rel,\ PF} < 0.15}$ - Isolation criterion determined by the particle flow algorithm. It is given by the amount of energy around the particle in a cone with $R = 0.3$, divided by the particle's energy.

The following requirements ensure that one does not misidentify a conversion of a prompt photon as an electron.

- $\mathbf{N}_{\text{Missing Tracker Hits}} \leq \mathbf{1}$ - Number of tracker hits that are missing. A prompt photon most likely converts after passing through the first layers of the ECAL, thus the extrapolated track will not have any hits in these layers.
- $\mathbf{\text{Vertex Fit Probability} < 10^{-6}}$ - Likelihood of the electron being matched to a conversion vertex.

Isolation describes the amount of energy in close vicinity $\Delta R = 0.3$ to the particle's trajectory. To match the electron trigger's settings, the individual tracker and calorimeter entries[3] are also required to have an isolation less than 0.2, respectively.

[3]This also takes into account possible HCAL entries, for cases where an electron was able to pass through the ECAL.

Chapter 6

Event Selection

After establishing the signature, datasets, Monte Carlo samples and object selection recipes, one can select the relevant events. To be able to evaluate possible signal contributions, this procedure is also meant to improve the signal to background ratio. The motivation behind that is the large difference in cross sections between the signal and all two muon, two jets processes. The same sign charge requirement is expected to have the biggest impact in that regard. Prior to that, the steps mainly concentrate on reducing *one* dominant background process at a time.

It should also be noted that this analysis was performed "blindly". Therefore control regions are used to estimate the agreement before one inspects the final CMS data distribution.

6.1. Event Cleaning

As a first step, a list of noise filters needs to be applied to the triggered events. Their purpose is to prevent a variety of detector specific effects to be misinterpreted as particles. It is maintained by the JetMET physics object group [62]. The recommended list [66] of noise cleaning filters encompasses the following entries.

- **CSC tight beam halo filter** - Uses information of the cathode strip muon chambers to identify anomalous MET created by the beam halo.
- **HBHE noise filter with isolated noise rejection** - Detects isolated noise of instrumental origin. In particular the one from hybrid photodiodes and readout boxes of the HB and HE hadron calorimeters.
- **HCAL laser filter** - Picks events where the HCAL laser fired at incorrect times. This leads to numerous entries throughout the entire HCAL.
- **ECAL dead cell trigger primitive filter** - Suppresses events where the trigger primitive energy lies above a certain threshold. These mismeasurements are due to the $\sim 1\%$ of dead ECAL cells.
- **Tracking failure filter** - Wards against two issues. Large clusters of hits can lead to less iterations of the tracking algorithm. Displaced primary vertices can also pose problems.

- **Bad EE Supercrystal filter** - Two of the 5×5 crystal regions appear to provide anomalous information in the electromagnetic endcaps EE. Removing these events is this filter's task.
- **ECAL laser correction filter** - The ECAL crystals are calibrated using a laser. This calibration lead to some crystals appearing to be highly energetic. To prevent a MET mismeasurement, the respective events are removed.
- **Tracking odd event filters** - Filters two types of issues. Events with (partially) aborted track reconstruction and events influenced by strip tracker noise.

This first stage of the analysis combines event cleaning with the **electron veto**. Since the chosen signature does not contain any electrons, the number of electrons selected by the previously defined recipe (Sec. 5.4) is required to be zero.

6.2. Basic Muon Selection

At this stage of the analysis, a first subset of muons is selected. Using the object selection recipe (Sec. 5.2) as a basis, the requirements are slightly tightened. Events with less than two muons passing the object identification are rejected immediately.

The `HLT_Mu17_TkMu8` trigger requires more than 17 GeV and 8 GeV transverse momentum for the respective muon. To avoid the trigger "turn on" [67] in the region close to that cut-off, the leading muon is required to have a transverse momentum of at least $p_{\mathrm{T}} > 20\,\mathrm{GeV}$. The value for the sub-leading muon has to exceed $p_{\mathrm{T}} > 15\,\mathrm{GeV}$, which is also well above the trigger requirement. Lower thresholds of around 10 GeV were tested, but mostly yield additional background, not signal events.

6.3. Jet Quality Criteria

The jet selection recipe for identification (Sec. 5.3) is not altered significantly. Thus their selection ensures the two muon, two jet signature, but does not exclude potentially good events by placing unusually high demands on jets.

To satisfy the final state of the signal, the number of jets cannot be lower than two. In addition to that, both the leading and sub-leading jets in terms of transverse momentum, need to pass the 30 GeV threshold. This is meant to help against clustered tracks or pileup contamination that may be identified as jets. Both the distributions of the number of jets (Fig. 6.1a) and the leading jet transverse momentum (Fig. 6.1b) show that these requirements mainly suppresses the Drell-Yan background.
Although the thresholds remove a sizeable portion of the jet content for certain signal simulations, there is a sufficient number of events remaining. Thinking back to the selection efficiencies for the signal in section 3.1, this distribution displays how variable the impact of requirements can be.

6.4. Muon Quality Criteria

To satisfy the signal signature of two *prompt* muons and provide the candidates for further selection requirements, events containing exactly two "good" muons are selected. For this

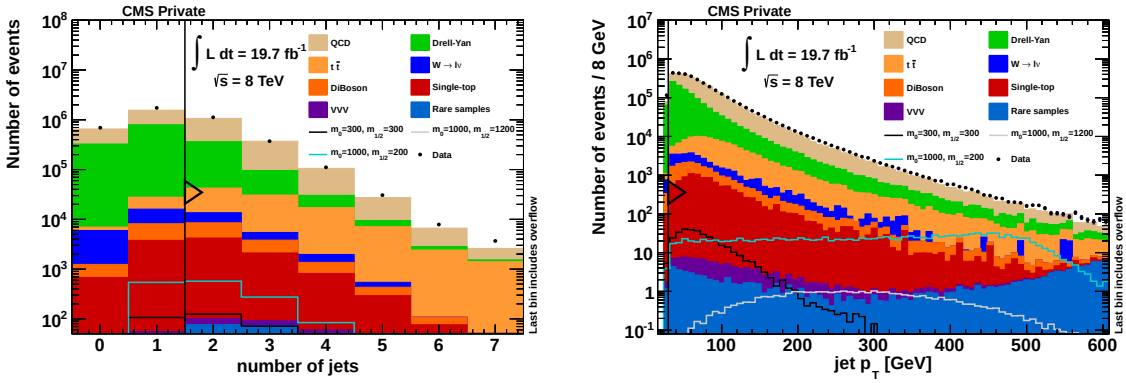

(a) (b)

Figure 6.1.: Number of jets (6.1a) and leading jet transverse momentum (6.1b) after the basic muon selection, before applying the jet quality criteria. The jet quality criteria require at least two jets and $p_{\mathrm{T},j_i} > 30\,\mathrm{GeV}$.

purpose, the basic muon subset is refined through trigger-matching as well as isolation and impact parameter thresholds. It should be noted that the actual process of evaluating the events has been performed before the event cleaning. For the impact parameter, this was meant to prevent any bias. And with regards to the remaining parameters it was unavoidable, due to the structure of this analysis (see chapter 7).

Every *event* examined at this stage is already required to pass the selected trigger (Sec. 5.1). Building upon that, the trigger-path for the *muon* content of each event is also compared to the one of `HLT_Mu17_TkMu8` for every single particle. Only particles that fulfil this match are considered as candidates to ensure a minimum reconstruction quality and equal conditions throughout the entire subset.

In addition to that, there are two different types of isolation criteria implemented. For the first one all calorimeter and tracker information are taken into account, thus naming the combined relative isolation I_{rel}. For its calculation, the following formula is suggested for all 2012 analyses.

$$I_{\mathrm{rel}} = \frac{\sum p_{\mathrm{T,\ charged\ had.}} + \max\left(0, \sum E_{\mathrm{T,\ neutral\ had.}} + \sum E_{\mathrm{T},\gamma} - \Delta\beta \sum p_{\mathrm{T,\ PU}}\right)}{p_{\mathrm{T},\mu}} \tag{6.1}$$

Each sum is determined by the particle flow algorithm. When adding them up, the $\Delta\beta$ corrections are applied to the neutral energy deposit. The corrections are based on the energies of charged particles not stemming from the primary vertex. These are determined by splitting particle flow candidates by whether or not they are considered to be pileup contributions. The factor of $\Delta\beta = 0.5$ has been determined from jets as an average of neutral to charged particles [68].

The sum of the four components represents the energy/transverse momentum around the muon candidates in a cone with a radius of $R = 0.4$. Division by the particle's transverse momentum reduces the dependence on the centre-of-mass energy of 8 TeV. With higher energies in the initial state, the absolute amount of energy carried by all the products is expected to rise as well. However, the relative distribution of said energy is expected to remain similar. With highly energetic muons and a relative isolation criterion, pileup contamination

also becomes less of a problem for the same reason. Figure 6.2 shows the distribution of the combined relative isolation.

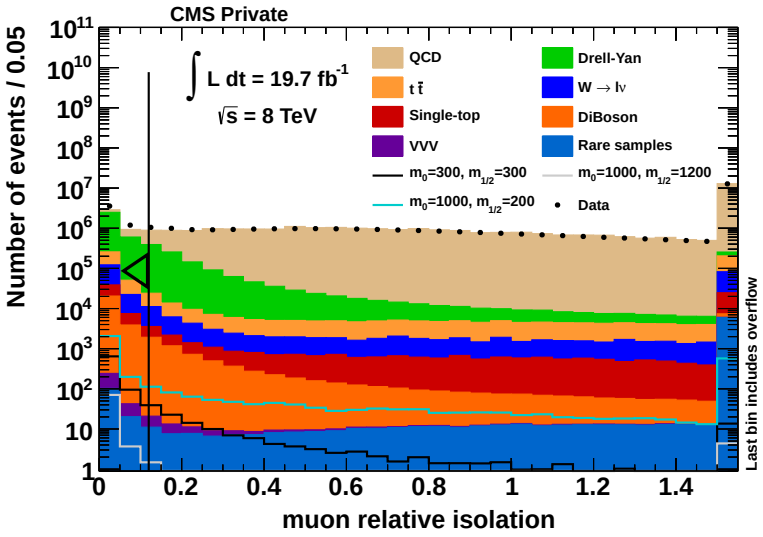

Figure 6.2.: Combined relative isolation I_{rel} (Eq. 6.1) of muons. In the large overflow bin, the almost constant continuation of the distribution is contained. For this analysis, it is not of relevance. This histogram is generated after the choosing the trigger, but before performing any other event selection.

For tight muons the recommended threshold value is $I_{\text{rel}} < 0.12$ [59]. As one can see, the majority of QCD events (Roughly 95 %) are rejected by this. Naturally, muons stemming from hadronic interactions, whether they are real or faked, are more likely to have fragments interfering with the isolation. Additionally, one can observe the signal simulations being affected differently. The softer decline for the high m_0 and low $m_{1/2}$ Monte Carlo will have a negative impact on the efficiency of selecting its events.

The second isolation criterion deals with the spatial distance ΔR between jets which pass the object selection and muons. It is required to be at least 0.4 for each of the two muon candidates. Similarly to the combined relative isolation, this ensures that the muon has a reasonably clean trajectory to work with. Although in this case the emphasis is put on hadronic interferences instead of taking a combination of all of them.

Further restrictions are placed upon both the impact parameters. The CMS muon physics object group suggests tightening the *transverse* one to $|d_{xy}| < 0.2\,\text{mm}$. By reducing it by one order of magnitude, vertices cosmic muons are suppressed more effectively. When comparing the *longitudinal* impact parameters d_z of both muons, the signal particles are expected to be very close to each other as the supersymmetric decays are effectively prompt. In figure 6.3, the difference between the impact parameters of the two candidates is visualized.

Almost no signal events can be observed past $\Delta d_{z,\mu\mu} \leq 0.8\,\text{mm}$. While one might consider tightening the requirement, it has been kept at 0.08mm to stay consistent with the 7 TeV analysis and provide a better comparison.

Only events with two muon candidates who suffice all listed requirements pass this stage of the selection.

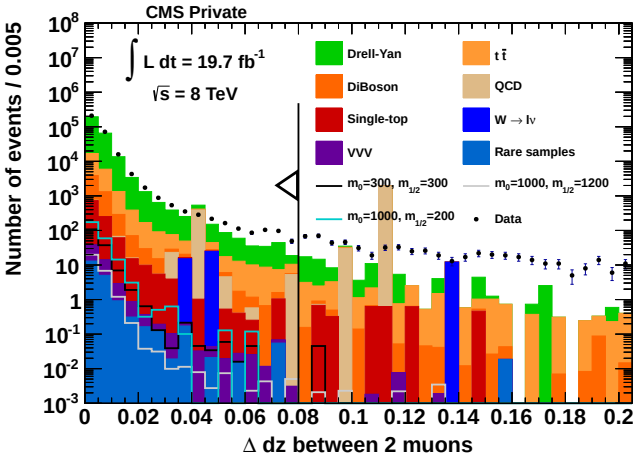

Figure 6.3.: Difference between the longitudinal impact parameters of the two muon candidates. This histogram is generated after the jet quality criteria, but before applying the muon quality criteria. Towards higher differences in z the agreement suffers from low statistics and the simulation of non-prompt muons.

6.5. Drell-Yan Normalization

After applying both the muon and jet quality criteria, the Drell-Yan background is the dominant one. However, upon closer inspection a discrepancy between data and simulation can be observed. To allow for better comparison between them, scaling factors f (Eq. (4.2)) can be employed. This is a reasonable choice, since this background does **not** contribute to the final distributions. Determining the ratio between the integrals of data and simulation yields the scale factors. The ranges that are being taken into account for the determination are $15-45\,\text{GeV}$ for the low mass sample covering 10 to 50 GeV and $80-120\,\text{GeV}$ for the high mass sample, which covers everything upwards of 50 GeV. Both values $f_{10-50} = 1.23$ and $f_{50-\infty} = 0.96$ are within the expected range. While the statistical errors on f are negligible, the systematic dependency on other requirements is estimated to be 5 %. The factors are applied throughout the entire analysis, including distributions preceding this section.

Strictly speaking, this is not part of the event selection. Nevertheless the Drell-Yan background is most relevant at this stage, therefore the adjustment is performed here as well. In figure 6.4a and 6.4b the invariant mass of both selected muons is shown before and after the scaling, respectively.

Comparing both the entries centered around the Z-peak and especially the ones for lower invariant masses, one can observe a noticeable improvement. With the general shape of the data being well described, the assumption that the difference can be accounted for by a scale factor, holds true.

The reasoning as to why one observes discrepancies is different for the two Drell-Yan samples. The first one ($10\,\text{GeV} < m_{ll} < 50\,\text{GeV}$) is only weighted with a leading order cross section, as higher order calculations are not available for this region. Thus a variation of $\mathcal{O}(10\%)$ is easily within the realm of possibilities, as a NLO calculation can have a similar impact. Since the second sample ($50\,\text{GeV} < m_{ll}$) is already weighted with a NNLO leading order cross section, a significantly lower correction is expected. The overprediction in that region is attributed to the multi-jet simulation, whose accuracy is limited.

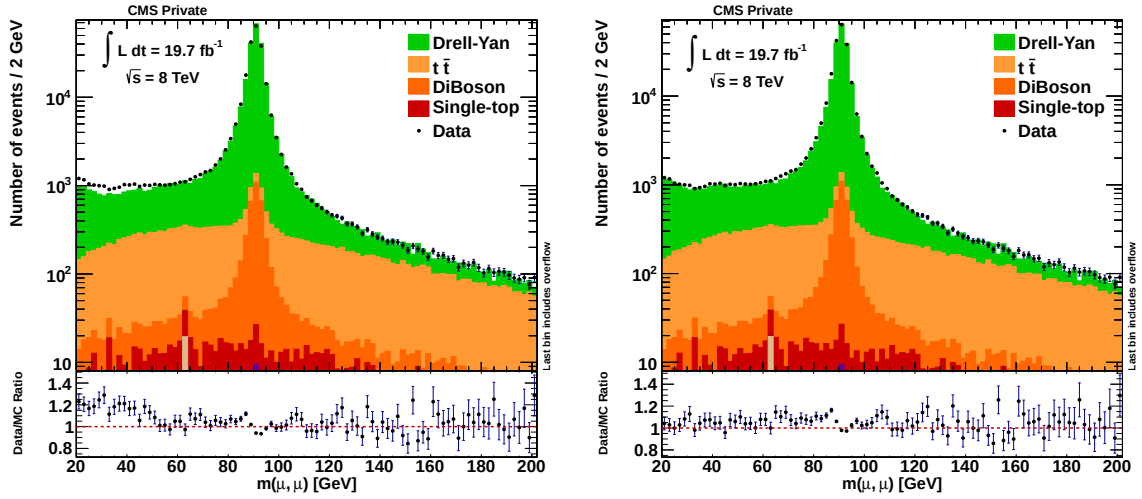

(a) (b)

Figure 6.4.: Invariant mass of the two selected muons. In histogram 6.4a the scaling factors for the Drell-Yan background are not applied, while in histogram 6.4b they are. The distributions are generated after the muon quality criteria and before the invariant dimuon mass requirement.

6.6. Invariant Dimuon Mass

Events with an invariant dimuon mass smaller than $m_{\mu\mu} < 15\,\text{GeV}$ are rejected to stay above quarkonian resonances.

6.7. Missing Transverse Energy

As discussed in chapter 3, *resonant* production of sleptons usually leads to low amounts of missing transverse energy in the final state. In this analysis, MET has been computed using the particle flow algorithm. The corresponding histogram is given in figure 6.5.

The distribution shows very good agreement up until roughly 230 GeV. Here one can see a slight systematic overprediction. The $t\bar{t}$ sample which dominates this region, has been generated with POWHEG. Since this generator does not include more than one hard jet on matrix element level, the increasing jet multiplicity towards higher energies poses more of a challenge. Therefore the discrepancy is comprehensible. One can also see that the majority of the expected signal contribution is concentrated in the region with very little MET. Once again, the shape of the signal varies between the different regions of the phase space. Compared to the other simulations, the selection efficiency for the high m_0, low $m_{1/2}$ point suffers a lot due to the softer decline. To optimize the signal to background ratio for the majority of SUSY parameter configurations, the threshold is set at $E_{\text{T}}^{\text{miss}} < 50\,\text{GeV}$.

To be able to judge the quality of the last steps of the event selection without consulting the final distributions, control regions are introduced. An orthogonal sample is generated by inverting the missing transverse energy requirement. Demanding values larger than 50 GeV, is the first step for every control region. They are subsequently divided by their corresponding requirement passing or rejecting events.

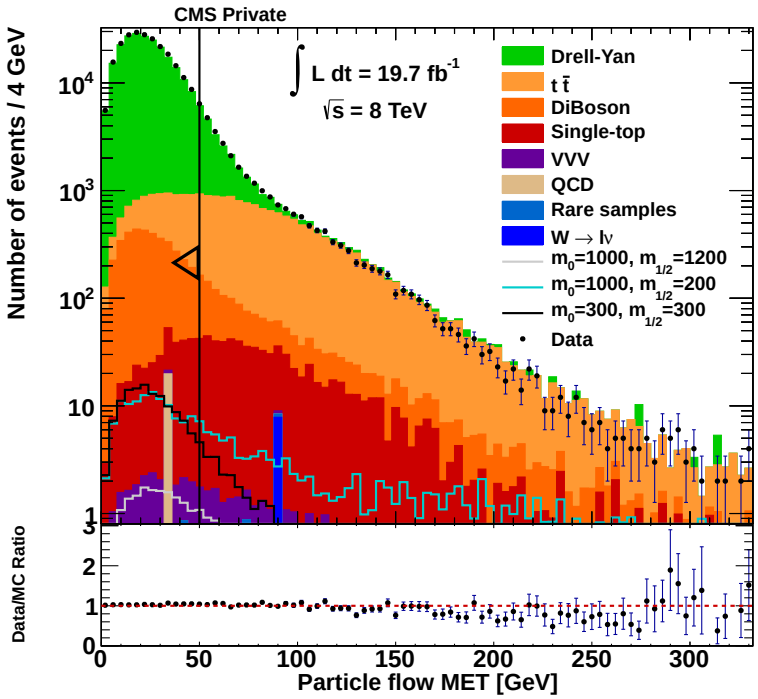

Figure 6.5.: Particle Flow missing transverse energy for events with two muons and at least two jets passing their respective quality criteria. The histogram is generated after the invariant dimuon mass requirement, but before applying the missing transverse energy requirement.

6.8. Jets from b-Quarks

The signal signature (Cf. chapter 3) only includes jets from the first generation of quarks. With the top quark backgrounds being amongst the dominant ones, a sizeable amount of jets will stem from bottom quarks (Fig. 4.1b). To reduce their contribution in the final distributions, the combined secondary vertex algorithm (**CSV**) [69] is used.

This very sophisticated algorithm combines a multitude of parameters to distinguish b-jets from non-b-jets. Its basis is the reconstruction of secondary vertices produced in the weak decay of bottom quarks. For that purpose the Trimmed Kalman Vertex Finder [70] is employed. Starting off with all tracks assigned to a jet, it isolates rogue ones. These are then used to reconstruct new vertices, which are sorted into three categories. For the first one, the vertex candidates have to suffice four criteria.

- The x-y-distance l_T between primary and secondary vertex has to be larger than 100 μm but within 2.5 cm.
- The significance $\frac{l_\mathrm{T}}{\sigma_{l_\mathrm{T}}}$ has to be larger than 3.
- The invariant mass of all charged particles must not be larger than 6.5 GeV.
- If there are two tracks with opposite charges, their mass must not be within 50 MeV of the K_S^0 mass $m_{K_S^0} = 497\,\mathrm{MeV}$.

If all requirements are met, the candidate is considered a reconstructed secondary vertex. Should they not be met, but there are still at least two tracks with the specified significance

higher than 2, a "pseudo-vertex" is created. This is the second category. If neither situation applies to the jet, it is placed in the third one.

Based on which category a jet belongs to, the criteria are tightened and/or expanded upon. Relevant variables for the identification of b-jets are the following ones.

- The invariant mass of all charged particles belonging to a secondary vertex can be compared to the one of charm quarks. If it is significantly higher, this can be used to veto against c-quarks.
- A high multiplicity of tracks is characteristic to b-jets, even compared to charm hadrons.
- Since bottom quarks have a comparatively long flight time, the significance $\frac{l_\mathrm{T}}{\sigma_{l_\mathrm{T}}}$ can be examined further.
- The energy fraction of all charged particles of the secondary vertex as well as the one of the entire jet can be compared to the hard fragmentation function of quarks.
- Due to the large mass of a bottom quark, the produced particles are on average less collimated than the ones of e.g. c-quarks. Therefore the differences in pseudorapidity between the particles with respect to the jet's axis can be used.
- Sorting the tracks by their impact parameter significance and determining their invariant mass can help against c-quarks as well. The first track exceeding the charm's mass threshold of 1.5 GeV[1] can be used to split them into two categories.

While all of them can be incorporated for the first category of vertices, the significances have to be excluded for the second one. The reason behind this is the lack of a geometrical fit for this type of vertex. For the third category no additional variables are used.

To derive a single value v for discrimination, all variables are combined into a likelihood function $\mathcal{L}$. Since light (u, d, s, c) and charm quarks lead to different parameter distributions, they are handled separately. v is then given by

$$v = f_\mathrm{BG}(c) \cdot \frac{\mathcal{L}^b}{\mathcal{L}^b + \mathcal{L}^c} + f_\mathrm{BG}(q) \cdot \frac{\mathcal{L}^b}{\mathcal{L}^b + \mathcal{L}^q} \quad \text{with} \quad \mathcal{L}^{b,c,q} = \mathcal{L}^{b,c,q}(\alpha, x_i) \tag{6.2}$$

The likelihoods $\mathcal{L}$ are a function of the vertex category denoted by α and the x_i, which denote the variables. Both b- and c-quark jets contain a certain amount of b-quarks. The ratios of likelihoods are weighted with the expected a-priori probabilities of the b-quarks in light quark $f_\mathrm{BG}(q)$ and charm quark $f_\mathrm{BG}(c)$ jets ($f_\mathrm{BG}(q) + f_\mathrm{BG}(c) = 1$).

The medium working point for the CSV (**CSVM**) has been chosen for this analysis to reduce the $t\bar{t}$-background. Its suggested discriminator value is $v > 0.679$ [71]. To make this choice, one can judge the algorithm's performance by consulting the distribution of the highest b-tag discriminator in every event shown in figure 6.6a. One can see the majority of the top pair background being cut off by the chosen threshold, while the signal has its lowest contribution in this region. It is quite apparent that there are discrepancies between data and MC, especially towards the lower discriminator values. They are being accounted for by adjusting the b-tag status of a fraction f of all jets[2] [72]. Depending on whether one needs

[1] This is only a rough estimate, since not all the right decay products will enter the calculation. In addition to that, neutral particles will also be missed.

[2] Once again b, c and light jets are treated separately.

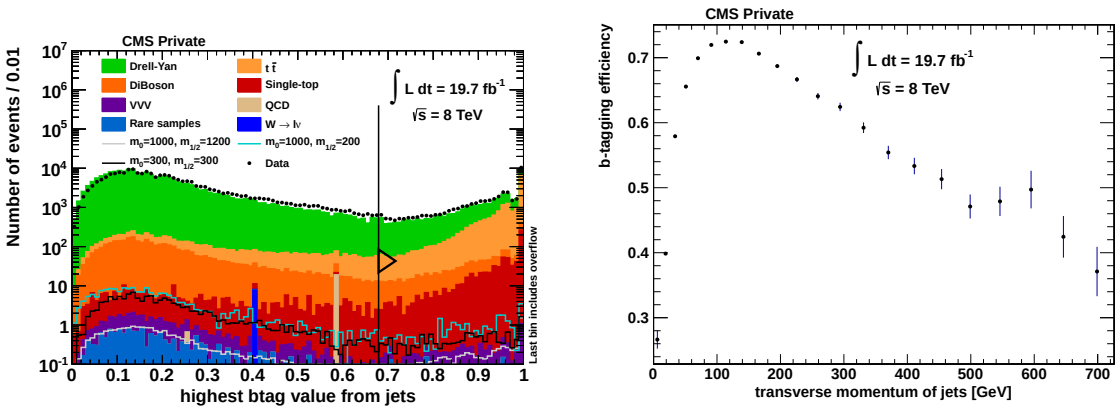

(a) (b)

Figure 6.6.: Highest b-tag discriminator of an event 6.6a and p_{T}-projection of the Monte Carlo b-tagging efficiency 6.6b. The discriminator distribution is generated after the missing transverse energy requirement, while the efficiency maps are generated using the $t\bar{t}$ sample after the trigger requirement, before any other event selection.

to upgrade a non-tagged or downgrade a tagged object, a different formula for determining f has to be used.

$$f = 1 - \mathrm{SF} \quad \text{for} \quad \mathrm{SF} < 1 \,(\text{downgrade}) \tag{6.3}$$

$$f = \frac{1 - \mathrm{SF}}{1 - 1/\varepsilon_{\mathrm{MC}}} \quad \text{for} \quad \mathrm{SF} > 1 \,(\text{upgrade}) \tag{6.4}$$

Here, $\varepsilon_{\mathrm{MC}}$ denotes the efficiency of the algorithm selecting bottom quark jets in the Monte Carlo simulation. The scale factors SF are defined by dividing the same efficiency measured in data by Monte Carlo one: $\mathrm{SF} = \varepsilon_{\mathrm{DATA}}/\varepsilon_{\mathrm{MC}}$.

While the scale factors are provided as p_{T} and η dependent functions on the CMS b-tagging TWiki [73], the Monte Carlo efficiency has to be determined individually for each analysis. This is due to its dependence on the relevant background samples and analysis requirements. To determine $\varepsilon_{\mathrm{MC}}$, the number of jets tagged as a certain flavour by the CSVM algorithm is divided by the number of jets which truly carry that flavour. A jet's true flavour can be retrieved by the jet flavour tool [74]. It uses Monte Carlo generator information to determine the origin of the jet.

Counting the numbers of tags for the denominator and true b-jets for the enumerator with respect to their p_{T} and η is done after adjusting the jet energy resolution of the Monte Carlo samples. The efficiency is only estimated using the $t\bar{t}$ background as it is the most relevant one for this requirement. Figure 6.6b shows the p_{T}-projection of the Monte Carlo efficiency map. For increasing η values the shape remains the same, with slightly decreasing efficiencies ($\mathcal{O}(5\%)$) for all bins. Towards higher energies, the number of entries and therefore the statistical uncertainty does not allow for a reasonable estimate of the efficiency anymore. The value of the last bin is used for any jet exceeding the energy maximum. To get a model prediction, rather than being influenced by a few single bins with abnormal values, the ROOT smoothing algorithm [75] has been employed. It estimates the contents of a bin by taking its neighbouring ones into account.

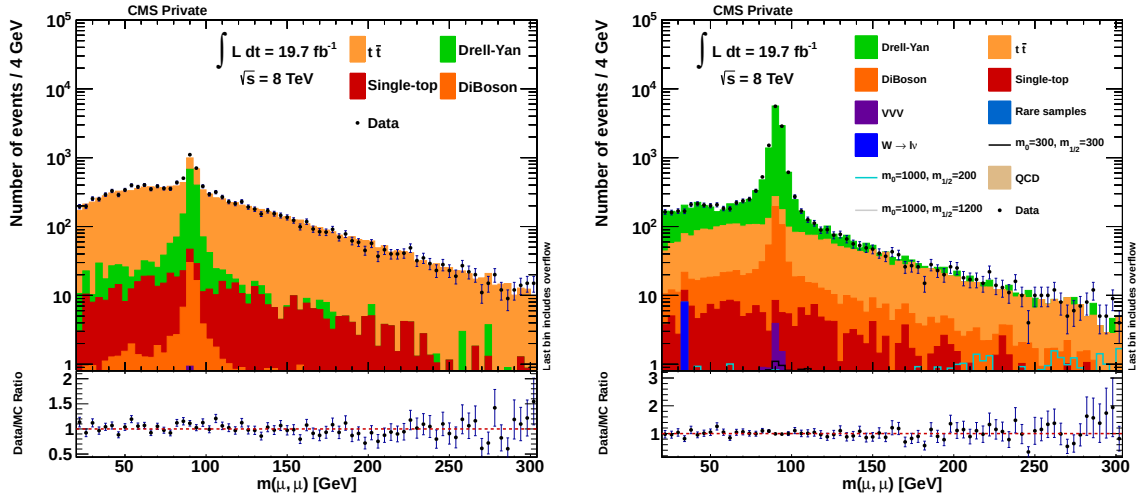

(a) (b)

Figure 6.7.: Control regions (MET $> 50\,\text{GeV}$), which include all requirements up to the b-quark stage, that display the effect of the b-tagging algorithm. On the left the b-tagged events 6.7a and on the right b-jet vetoed events 6.7b are shown.

With a set algorithm to tag b-jets, the control regions can be inspected to judge its performance. Figure 6.7a shows the $m_{\mu\mu}$ distribution in the control region with events that are tagged as b-jets and will therefore be rejected. Complementary to that, 6.7b displays the remainder of events after vetoing against b-jets. Both distributions show good agreement between data and simulation. Combined with the majority (roughly 80 %) of the rejected entries being from the top pair background, this entire method successfully reduces the bottom quark jet contribution in the final state.

6.9. Same Sign Charge Muons

At this stage of the analysis, there is still *at least* one order of magnitude between the number of events of the background prediction and a potential signal. As explained in the discussion of the signature in chapter 3, the charge of both prompt muons can be the same. Most of the background Monte Carlo events cannot lead to the same condition in the final state. As a result, this requirement is able to improve the signal to background ratio significantly.

The corresponding control region *adds* the charge restriction to the previously defined b-jet veto control region. Figure 6.8 shows the dimuon, smuon and gaugino mass distribution. The slepton mass is given by the invariant mass of the two muon and jet candidates, while the gaugino mass only takes the sub-leading muon and two jet candidates into the calculation. When comparing the invariant mass of the two muons in the same sign charge control region (Fig. 6.8a) to the b-jet veto control region (Fig. 6.7b), whose only difference is no charge-based requirement at all, one does see the drastic reduction of the background. However, the agreement between data and simulation appears to be worse throughout the entire mass spectrum in all charge control region distributions. When taking the unexpectedly large contributions of samples containing many jets like $t\bar{t}$ into account, this suggests that the background is not described accurately. One effect that contributes significantly to this phenomenon will be discussed in the upcoming chapter.

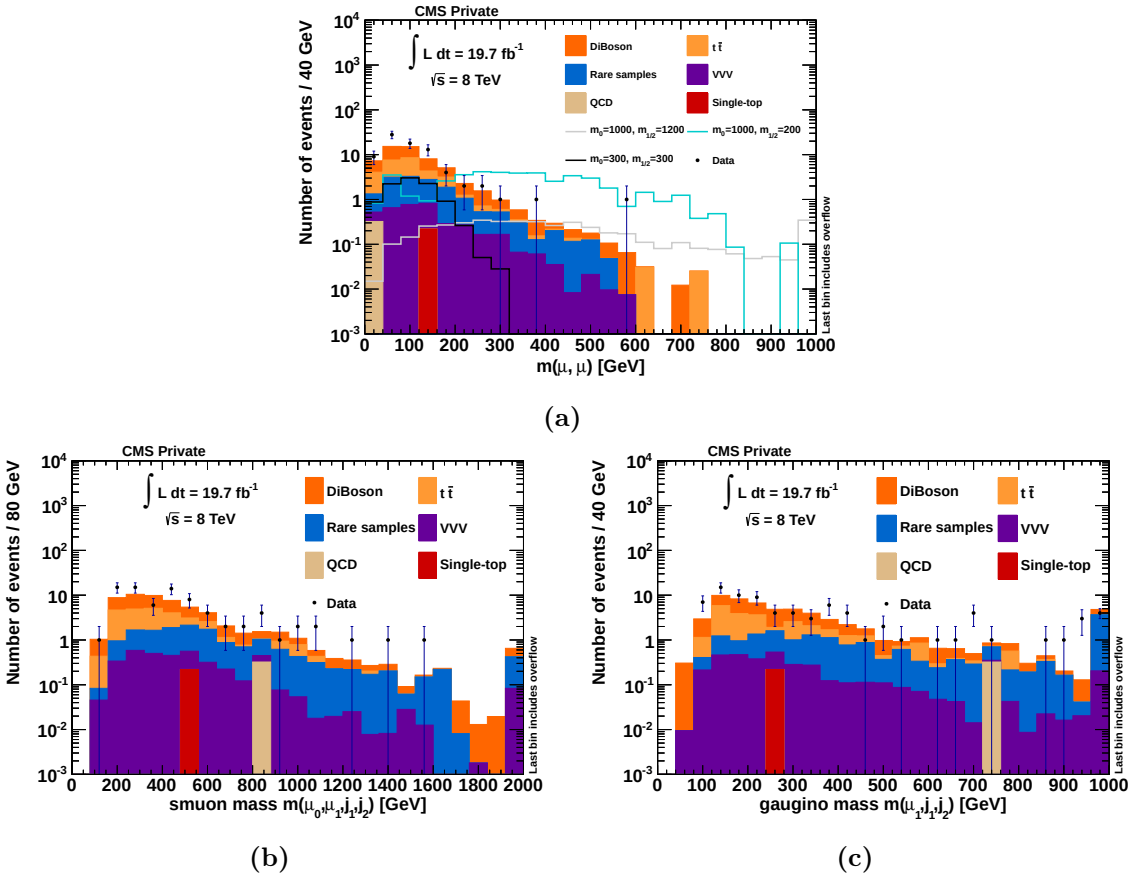

(a)

(b)

(c)

Figure 6.8.: Invariant mass of the two muon candidates 6.8a, mass of the gaugino 6.8c and mass of the smuon 6.8b from the b-jet veto plus charge control region. The gaugino mass is the invariant mass of both jets and the sub-leading muon candidate, while the smuon mass includes the leading muon as well. The latter two distributions will be expanded upon in the following chapter.

6.10. Control Region Overview

A short overview of all used control regions up to this point is given in figure 6.9. The inversion of the $E_{\mathrm{T}}^{\mathrm{miss}} < 50\,\mathrm{GeV}$ is the basis for all control regions. Afterwards, one differentiates between events with b-jet tags or a b-jet vetos. Continuing with the events that have the veto, one demands the charge of the muons to carry the same sign. Passing this requirement marks the final control region.

6.11. Selection Efficiencies of Requirements

To summarize the event selection, figure 6.10 shows the consecutive impacts of the requirements on the number of events. Table 6.1 translates these values into selection efficiencies relative to the number of events after requiring the chosen trigger. Focussing on the simulations of the signal models, one can once again see the varying impact of the requirements depending on the mass parameters m_0, $m_{1/2}$, which has been mentioned throughout this chapter. Most striking are the impacts of the jet and muon quality criteria, as well as the

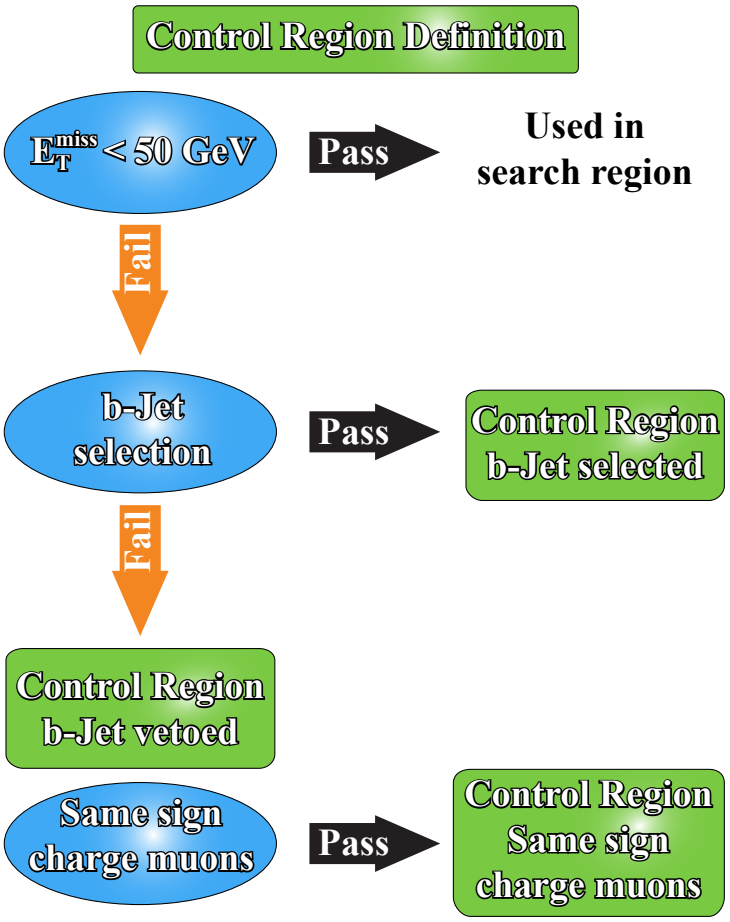

Figure 6.9.: Overview over the used control regions. Blue ellipses mark requirements, green boxes mark control regions and arrows indicate whether an event passes or fails a requirement.

missing transverse energy requirement.

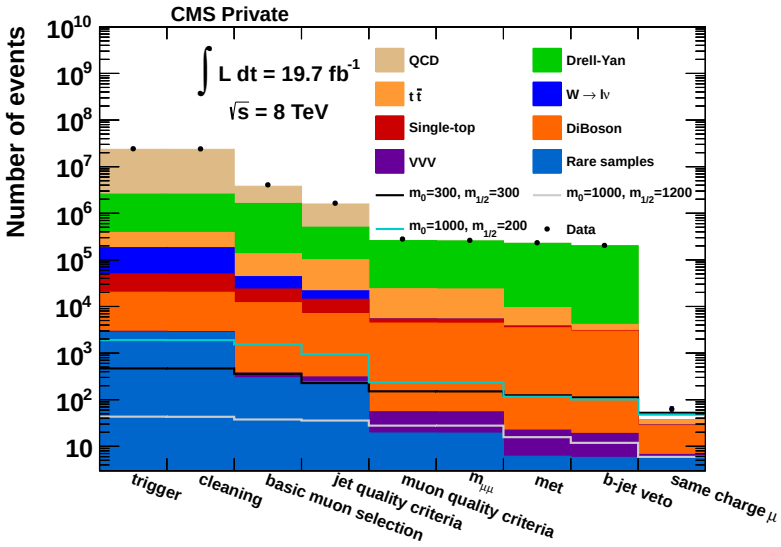

Figure 6.10.: Number of events after consecutively applying the different event selection requirements.

Sample Group	N_{Events}	Muon selection	Jet quality	Muon quality	$m_{\mu\mu}$	E_T^{miss}	b-jet veto	Same charge μ	N_{Events}
Drell-Yan	$2.2 \cdot 10^6$	67.9	18.3	10.7	10.5	9.9	9.0	0	0
QCD	$2.1 \cdot 10^7$	10.4	5.1	10^{-4}	10^{-6}	10^{-6}	10^{-6}	0	0
$t\bar{t}$	$2.0 \cdot 10^5$	45.0	38.6	9.1	9.0	2.8	0.5	0.004	7.32
$t\bar{t} + V$	$7.9 \cdot 10^2$	54.0	51.6	17.5	17.3	6.2	1.3	0.02	1.27
Single top	$3.0 \cdot 10^4$	39.0	24.2	3.3	3.3	1.0	0.3	0.001	0.8
Diboson	$1.5 \cdot 10^5$	21.1	9.4	2.9	2.9	2.3	2.0	0.01	21.0
VVV	$1.2 \cdot 10^2$	62.8	49.7	29.2	29.1	13.2	10.7	0.9	1.1
Rare samples	$1.1 \cdot 10^2$	45.2	31.4	17.5	17.4	5.6	5.3	5.1	5.6
m_0, $m_{1/2}$ [GeV]	Signal Models								
300, 300	$4.7 \cdot 10^2$	76.6	48.5	32.3	32.1	26.5	23.9	11.2	52.4
1000, 200	$1.9 \cdot 10^3$	80.6	50.1	12.4	12.3	6.1	5.3	2.5	47.8
1000, 1200	$4.3 \cdot 10^1$	86.9	82.4	64.1	64.1	36.3	27.4	13.7	5.9
Data	$2.4 \cdot 10^7$	16.8	6.8	1.2	1.1	1.0	0.8	0.001	63

Table 6.1.: Consecutive selection efficiencies given as percentages for different requirements discussed throughout the event selection. All efficiencies are given relative to the number of events remaining after requiring the HLT_Mu18_TkMu8 trigger. The second column shows the number of events after requiring the trigger and last column show the number of events after all requirements.

Chapter 7

Data-driven Background Estimation

One does observe a sizeable contribution from backgrounds like $t\bar{t}$ in the b-jet veto plus charge control region after the final step of the event selection (Cf. fig 6.8). This is the case despite them being unable to produce two prompt same sign charge muons. That necessitates at least one of the two leptons to be misreconstructed. Muons from jets or other secondary interactions could be falsely associated with the vertex in question. Another possibility are punch-through particles traversing the HCAL and leaving tracks in the muon system. For example fragments from a hadronic interaction, like a charged pion or kaon, could yield enough hits in the chambers, given enough energy. As a result, this particle may be misidentified as a muon, if a coincidentally matching trajectory can be found in the tracker. Both cases lead to a "fake muon". Obviously only the latter is a *true* fake muon, but both occurrences are usually handled the same way. The corresponding selection requirements are isolation for the secondary interaction case and the trajectory quality criteria for the punch-through one. However, preventing either scenario from happening by tightening their thresholds is unlikely to impossible. The poor agreement between data and prediction can be improved by utilizing a portion of the measurement, which is orthogonal to the signal region. To estimate the contribution of misreconstructed muons from data, the "fake rate method" is employed.

7.1. Fake Rate Method

The "fake rate method" will replace the dominant Monte Carlo samples with the data-driven estimate of multi-jet contributions. This encompasses the following backgrounds (Cf. tab. 7.1): $W+$ jets, production of single tops, top pairs and top pairs with real photons as well as the entirety of the multi-jet samples. On the other hand the Drell-Yan processes, two and three vector boson backgrounds, top pair production with additional vector bosons, $W + \gamma$ and rare samples will be taken from simulation.

The general idea of the fake rate method is to estimate the contributions of misreconstructed particles by comparing one tightly and one loosely selected muon sample. It should be noted that the *loose* muon selection is only used in the data-driven background estimation, while the ones used in the analysis are denoted as *tight*[1] ones. Two criteria are used to separate the samples from one another. First and foremost, the combined relative isolation criterion is being raised from $I_{\text{rel}} < 0.12$ to $I_{\text{rel}} < 0.5$. This adds a sizeable contribution from

[1] The dimuon criteria are not applied for the data-driven background estimate.

Monte Carlo samples	Replaced
Drell-Yan	No
QCD	Yes
Single-top	Yes
$t\bar{t}$	Yes
$t\bar{t} + V$	No
$W \to l\nu$	Yes
DiBoson	No
VVV	No
Rare Samples	No

Table 7.1.: Overview over which Monte Carlo samples are and which aren't replaced by the data-driven background estimation. Table 4.3 lists the samples which are combined under a single label.

backgrounds such as QCD and $t\bar{t}$ with muons stemming from secondary interactions. Additionally, the transverse impact parameter requirement has been loosened from $|d_{xy}| < 0.2\,\text{mm}$ to $|d_{xy}| < 2\,\text{mm}$. This allows for more displaced vertices to enter the selection.

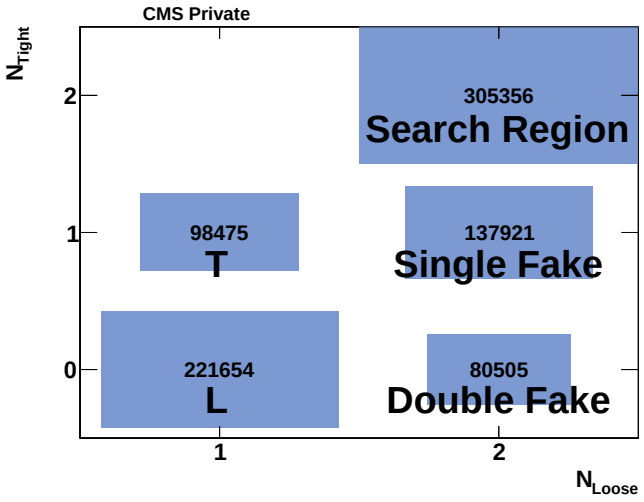

Figure 7.1.: Number of loose versus number of tight muons measured in data. This histogram is generated before applying the muon quality criteria. The samples names indicate their application: T - Tight, L - Loose, Single-fake, Double-fake, Search region.

To measure the tight-to-loose ratio independently from the final distributions, an orthogonal sample needs to be constructed. Much like the control regions are defined by an inverted MET requirement, the number of loose muons N_{Loose} in an event can be used. Disjointed from the analysis sample ($N_{\text{Loose}} = 1$ in figure 7.1), the fraction of tight to loose muons $F_R = \frac{T}{T+L}$ [2] can be determined. To account for possible dependencies introduced by the detector, it is measured as a function of η and p_{T}.

Using F_R, the number of tight muons N_{Tight} can be predicted from the number of loose (but not tight) ones $N_{\text{Loose(!T)}}$. The definition of loose muons also includes all tight ones. Therefore, to stay in line with the independence of samples, one has to ensure that amongst

[2] This is often confusingly called the "fake rate", thus naming the method.

the number of loose muons $N_{\text{Loose(!T)}}$, there are *no* tight ones. The resulting formula is given below.

$$N_{\text{Tight}} = f \cdot N_{\text{Loose(!N)}} = \frac{F_R}{1 - F_R} \cdot N_{\text{Loose(!T)}} \tag{7.1}$$

When looking for two prompt muons, either one or both of them can be misidentified. Depending on whether or not the specific background can produce a prompt muon, one of the two cases will be prevalent. For "single-fakes", $W+$ jets or top pair production are prime examples. To predict the number of single-fakes from an orthogonal sample, one of the analysis' tight muons is replaced with a loose (but *not* tight) muon (Cf. fig. 7.1). The sum over the resulting number of events having one tight t and one loose muon l and applying the weight f, yields the number of single-fakes $N_{\text{Single-Fakes}}$.

$$N_{\text{Single-Fakes}} = \sum_{tl} f = \sum_{tl} \frac{F_R^1}{1 - F_R^1} \tag{7.2}$$

The additional index i of the tight-to-loose ratio F_R^i represents the dependency on the transverse momentum and pseudorapidity of the specific muon.

If both muons are misidentified, "double-fakes", the scenario has to be adjusted. Prime examples for this case are interactions dominated by hadronic activity, primarily the multi-jet background. Demanding two loose muons (which are *not* tight) serves the purpose of splitting the sample from the analysis' one in this case (Cf. fig. 7.1). The event weight f is now composed of individual weights $f^i(p_{\text{T}}^j, \eta^j)$ for each of the $j = 1, 2$ muons.

$$N_{\text{Double-Fakes}} = \sum_{ll} f = \sum_{ll} f^1 f^2 = \sum_{ll} \frac{F_R^1}{1 - F_R^1} \cdot \frac{F_R^2}{1 - F_R^2} \tag{7.3}$$

One would naively expect the sum of both cases to be the overall amount of fakes. However, the double-fake scenario is also embedded in the single-fake one. If the tight muon of the latter case has been faked, it becomes the double-fake scenario (Eq. 7.3). Since either of the two loose leptons of the double-fake case is able to fake the tight one, it is contributing *twice* to the single-fake case (Eq. 7.2).

$$N_{\text{Background estimate}} = N_{\text{Single-Fakes}} - N_{\text{Double-Fakes}} = \sum_{tl} \frac{F_R^1}{1 - F_R^1} - \sum_{ll} \frac{F_R^1}{1 - F_R^1} \cdot \frac{F_R^2}{1 - F_R^2} \tag{7.4}$$

7.2. Measurement

Estimating the background starts off by measuring the tight-to-loose ratio F_R. For that, the definition and selection of tight T and loose muons L is the first step. This is done after the event cleaning (Sec. 6.1), but before the basic muon selection (Sec. 6.2). Therefore events with any number of muons, specifically ones with less than two muons passing the object selection, can be included. For the *tight* subset, almost all of the muon quality criteria (Sec. 6.4) are applied. The only exceptions are the distance to the next jet and the distance between two muons. These requirements are only meant for selecting the two muon candidates of the analysis. They may otherwise introduce a bias towards the specific final state, thus limiting the prediction. As already stated before, *loose* muons are defined by the same rules, but only

have to abide $I_{\text{rel}} < 0.5$ and $|d_{xy}| < 2\,\text{mm}$.

Demanding exactly one loose muon (Fig. 7.2a) yields an independent sample. Since the prediction of fakes is strongly correlated to the amount of QCD multi-jet events, various kinematic and topologic requirements can be applied to isolate these. Requiring two jets (Fig. 7.2b) ensures a minimum amount of hadronic activity per event. With each jet's transverse momentum exceeding 50 GeV (Fig. 7.2c), the Drell-Yan background is being suppressed. After setting the minimum transverse momentum of the first muon to 20 GeV and all remaining ones to at least 10 GeV(Fig. 7.2d), the Z-peak can be eliminated for the same purpose. Thus the invariant mass of two muons[3] closest to the Z-mass, is restricted to a window from 10 GeV to 80 GeV (Fig. 7.2e). By setting an upper bound of 40 GeV for the missing transverse energy (Fig. 7.2f), the top-quark and W-Boson backgrounds are being discriminated, as QCD processes generally do not contain a lot of E_T^{miss}. By using the transverse mass hypothesis for a leptonically decaying W boson, it is also possible to reduce the same backgrounds. Requiring the value of the transverse mass of the loose muon[4] and the missing transverse energy to be less than 40 GeV (Fig. 7.2g) decreases the contribution of top and W backgrounds as well, while passing QCD multi-jet events.

$$m_{\text{T}} = \sqrt{2 \cdot p_{\text{T},\mu} E_{\text{T}}^{\text{miss}} \cdot (1 - \cos\Delta\phi(\mu, \vec{E}_{\text{T}}^{\text{miss}})} < 40\,\text{GeV} \tag{7.5}$$

Also, motivating a QCD-like back-to-back topology can be achieved through limiting the azimuth angle between the leading jet and loose muon to $\Delta\phi > 1$ (Fig. 7.2h).

In general, one can observe reasonable agreement between data and simulation in the $n-1$ distributions. In particular with regards to the electroweak processes. However in QCD dominated histograms, there is a noticeable deficit of QCD contributions towards higher energies. One major reason are the leading order cross sections used for these samples. Additionally, only a fraction of the hadronic activity can be simulated adequately. The large event weights given in table 4.2, are a testament to that. As a result, the statistical uncertainties for QCD multi-jet events are also large.

Counting the number of tight and loose muons in the resulting enriched sample, can be used to predict the hadronic activity leading to possible misidentifications. From the two dimensional tight and loose muon histograms containing the measured data, one has to statistically subtract all background samples which are taken from Monte Carlo (Tab. 7.1). The results are shown in figure 7.3.

The one dimensional version visualizes various tight-to-loose ratios as a function of p_{T}. While the prediction is depicted by the data points, from which the backgrounds have been subtracted, additional exemplary Monte Carlo samples show the general evolution of the hadronic activity for a few selected backgrounds. Once again, the decreasing statistics towards higher energies and leading order cross sections of QCD processes have to be kept in mind. As the data-driven estimate is meant to describe QCD multi-jet events, comparing the evolutions of the respective entries reveals that the data behaves differently than the prediction provided by the simulated QCD multi-jet events. This difference has to be kept in mind when determining the uncertainties of this procedure (Sec. 8.3.1).

For the actual prediction, F_R is used as a function of p_{T} and η (Fig 7.3b). Here, the smoothing algorithm [75] that has been introduced in the b-tagging section (Sec. 6.8), has

[3] The two muons encompass the one loose muon as well as one muon which passes the ID, but does not qualify as a loose muon.

[4] One expects the *loose* muon to stem from a secondary decay, which is why it is the subject of this requirement.

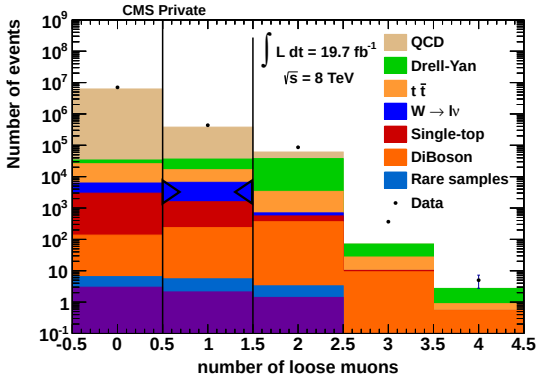

(a) Number of loose muons

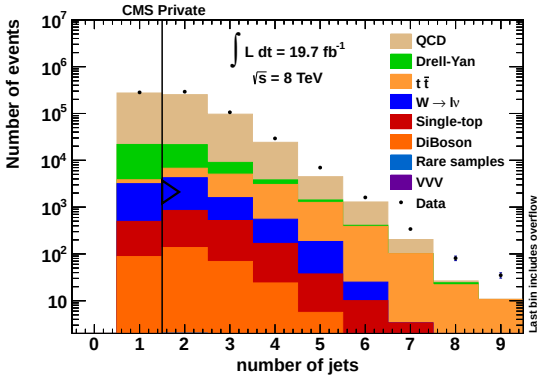

(b) Number of jets

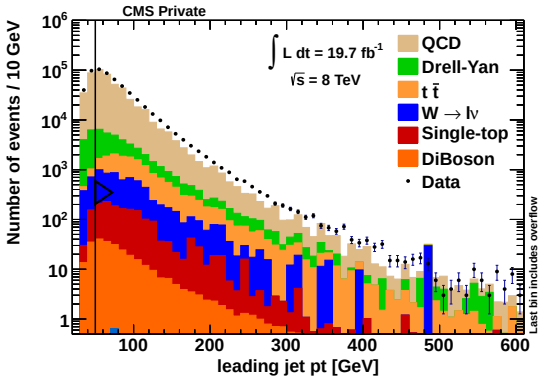

(c) Transverse momentum of jets

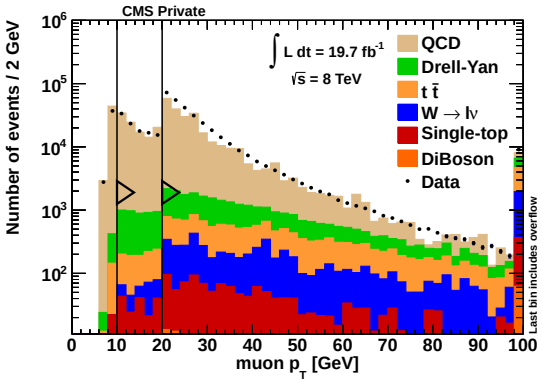

(d) Transverse momentum of muons

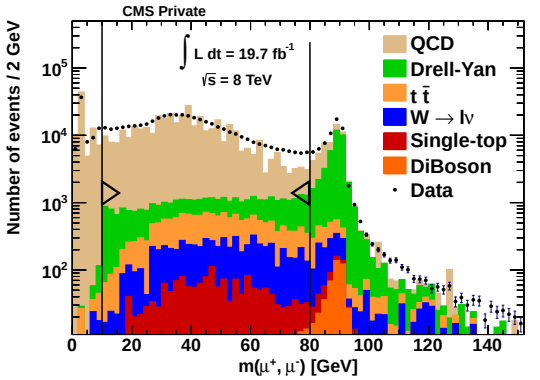

(e) Invariant dimuon mass closest to Z-mass

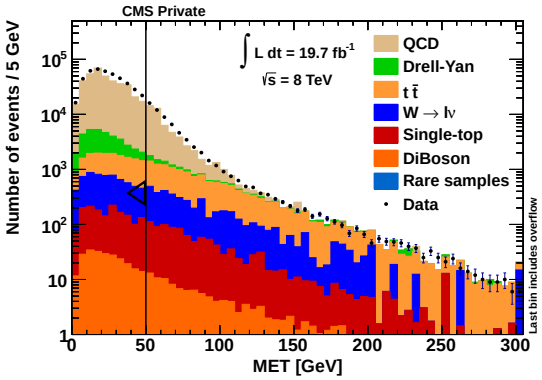

(f) Transverse missing energy $E_{\mathrm{T}}^{\mathrm{miss}}$

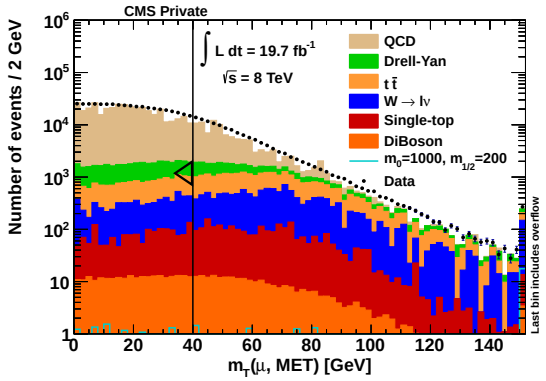

(g) Transverse mass of loose μ and $E_{\mathrm{T}}^{\mathrm{miss}}$

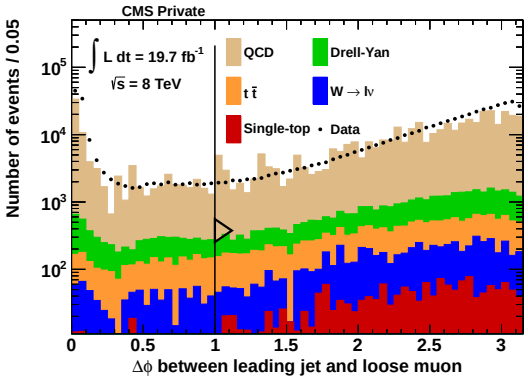

(h) $\Delta\phi$ between loose muon and leading jet

Figure 7.2.: $n-1$ distributions of the fake rate determiniation, generated before the basic muon selection. Requirements are indicated by arrows.

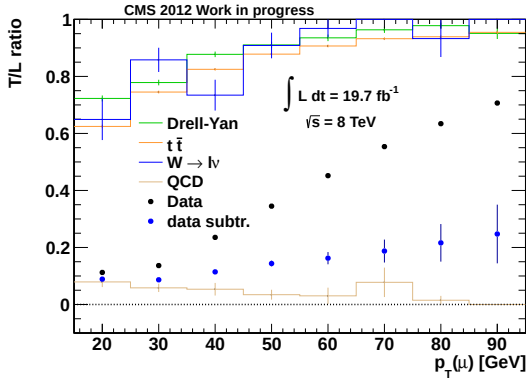

(a)

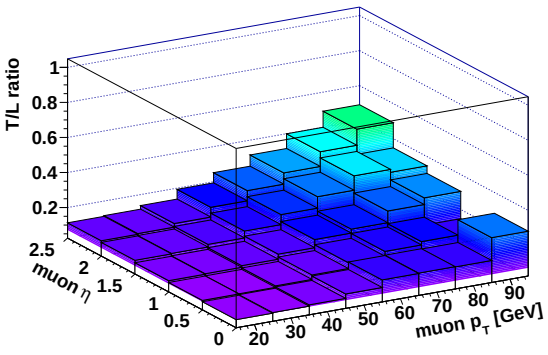

(b)

Figure 7.3.: Ratio of tight to loose muons for the calculation of F_R, as a function of p_{T} (7.3a) and as a function of both p_{T} and η (7.3b). Both histograms are generated after applying the multi-jet enrichment requirements of the data-driven background method.

been employed once more. This allows one to avoid rogue values in bins with a low amount of entries. Should any muon exceed the maximum transverse momentum for which this histogram can provide a reasonable estimate, the value of the corresponding last bin is used.

7.3. Prediction

With the tight-to-loose ratio F_R determined, the analysis can be rerun to determine the background estimate. As mentioned in section 7.1, the selection process of the two muons (Sec. 6.4) has to be altered to be working on an orthogonal sample. Instead of demanding the two tight leptons, one or both of them are replaced by loose muons, which are not tight ones. In combination with the respective event weights, this yields single- and double-fake estimates. Figure 7.4 shows the distributions for both estimates.

One can see that the data exceeds the simulated backgrounds, including QCD multi-jet production. This supports the hypothesis, that the contribution of fake muons is not well modelled and has an influence on the final state in question. Re-examining the b-jet veto

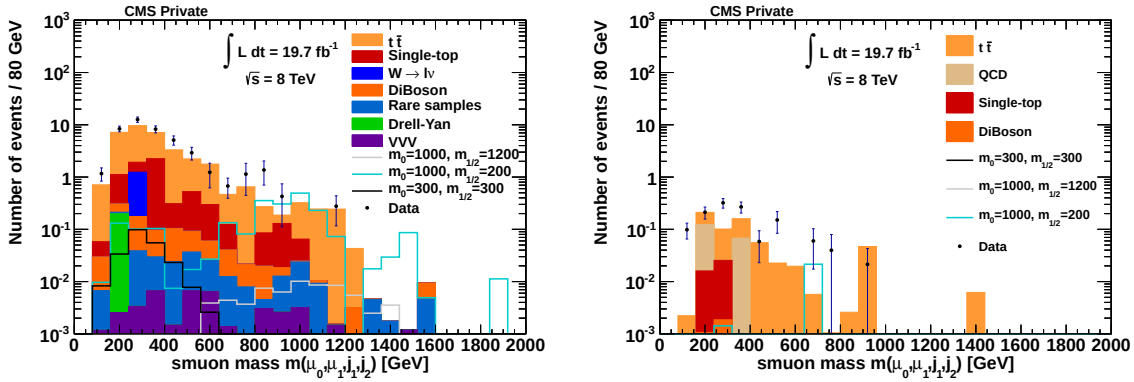

(a) (b)

Figure 7.4.: Single- (7.4a) and double-fake estimate (7.4b) for the smuon mass of the b-jet veto plus charge control region. The distribution before the fake estimate can be seen in figure 6.8.

plus charge control region previously discussed in section 6.9, yields the distributions shown in figure 7.5.

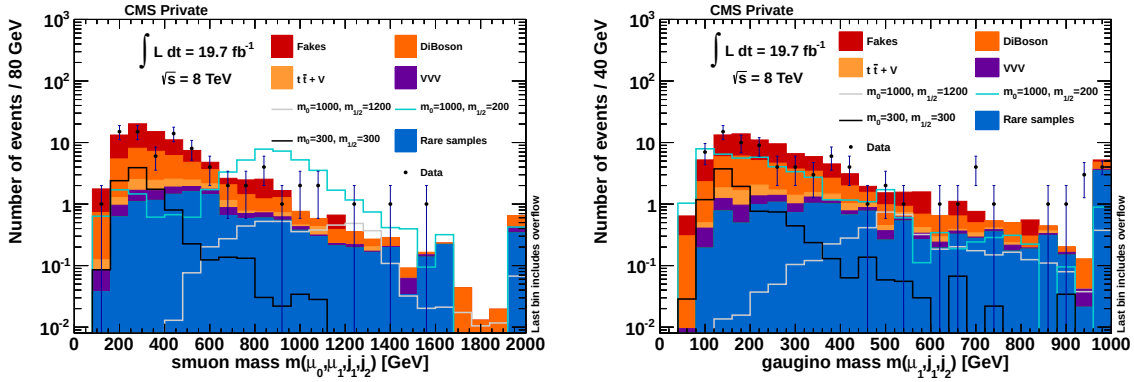

(a) (b)

Figure 7.5.: Smuon mass and gaugino mass of the b-jet veto plus charge control region, including the data-driven background estimate (Cf. fig 6.8).

With the inclusion of the fake rate method's prediction, the background describes the data significantly better. For a simple quantification of this statement, one can regard the entire distribution as a single bin and compare the number of entries. This yields the following values for the smuon mass distribution: $N_{\mathrm{MC}} = 86.6 \pm 3.0\,(\mathrm{stat.})$ and $N_{\mathrm{Data}} = 79.0$. A $-0.8\,\sigma$ deviation showing good agreement between data and background prediction.

Chapter 8

Systematic Uncertainties

Before unveiling the final distribution(s), the various systematic uncertainties have to be taken into consideration. These types of uncertainties describe an additional uncertainty or a possible bias that the methods of the analysis themselves introduce to a measurement or a prediction. To account for them, the parameters of the procedures are usually varied in a way that both over- and underestimations are covered. The relevant uncertainties can be split into two categories. On the one hand there are those that affect the analysis on a global scale, while on the other hand some only concern specific types of objects. Unless stated otherwise, all of the uncertainties are determined using the smuon mass distribution at the final stage of the analysis.

For the signal samples, the systematic uncertainties are estimated from the impact of each individual procedure on the three shown points in the RPV supersymmetry phase space. In most cases, the points with lower values of the universal mass parameters are experiencing the largest relative influence.

The systematic uncertainty of the data-driven background prediction is evaluated separately. Therefore the global and object uncertainties are only given for Monte Carlo samples which are *not* replaced by the estimate.

8.1. Object Uncertainties

8.1.1. Jet Energy Resolution

The procedure discussed in section 4.5 describes the adjustment of the jet energy resolution already. It remains the same for estimating its systematic uncertainty. As for the variation of its parameters, the core resolution factors (Tab. 4.4) are scaled according to their uncertainties. Both the statistical and systematic upper and lower bound are added quadratically and applied to the mean value. While this applies to both cases of matched and no matched gen-jets, the latter can only worsen the resolution. As a result, a core resolution factor is not expected to be less or equal to 1. With the width of the Gaussian distribution used for smearing given by $\sigma = \sqrt{\mathbf{c^2 - 1}} \cdot \sigma_{\mathrm{MC}}$, values below that threshold have to be adjusted. This is only the case for the lower bound of the $0 < |\eta| < 0.5$ range. Here instead of 0.990, 1.001 is used.

While the statistical error of the energy resolution in the Monte Carlo samples σ_{MC} is negligible, the fitting procedure is subject to systematic uncertainties such as the range it considers. To account for that and the slight dependence on the jet's transverse momentum

and η, the value of σ_{MC} has been varied separately from the core resolution scaling factors by $\pm 20\,\%$. The effect has been found to be below $0.1\,\%$.

For the background Monte Carlo samples, the overall effect for an upward deviation then amounts to $-0.1\,\%$ while for the downward one it is $+0.6\,\%$. For the signal prediction, it varies between $1.2\,\%$ and $3.4\,\%$.

8.1.2. Jet Energy Scale

For the jet energy scale (**JES**), there are a variety of factors which influence the measurement. A collection of all relevant values is being provided by the JetMET working group on their dedicated website [76]. It encompasses the following effects: Absolute scale uncertainty, high transverse momentum extrapolation, single pion influence, jet flavour extrapolation, time dependencies, pileup as well as a statistical uncertainty, resolution dependency and central fit dependency which are given relative to the p_{T} of jets. The quadrature of all contributions yields the total uncertainty. From the recommended set of uncertainty sources, `Summer13_V4_DATA_UncertaintySources_AK5PFchs` is used in this analysis.

Similarly to the jet energy resolution, the effect of scaling the jet energy has also been propagated to $E_{\mathrm{T}}^{\mathrm{miss}}$. Shifting the energies of all jets up and down affects the number of events by $+3.6\,\%$ and $-2.9\,\%$, respectively. The signal is affected by up to $7.8\,\%$.

8.1.3. Muon Momentum Resolution & Scale

The systematic uncertainties for the muon momentum resolution and scale have been determined by the Muon POG [31]. For muons with less than 200 GeV transverse momentum, the general recommendations are a $0.2\,\%$ uncertainty on the value of the scale and $0.6\,\%$ on the resolution. Should the particle exceed that p_{T} threshold, the uncertainty on the scale increases with $5\,\%\cdot p_{\mathrm{T}}/\mathrm{TeV}$. As studies with cosmic are used for measuring the uncertainty on the resolution, the signal topology is not described accurately. By assuming a continuous $30\,\%$ relative uncertainty on the resolution, based off the $0.6\,\%$ for $p_{\mathrm{T}} < 200\,\mathrm{GeV}$, the remainder of the spectrum [77] is estimated over three regions. The values used for smearing are $1.1\,\%$ for $p_{\mathrm{T}} < 350\,\mathrm{GeV}$, $1.65\,\%$ for $p_{\mathrm{T}} < 500\,\mathrm{GeV}$ and $3.1\,\%$ beyond that transverse momentum.

Applying the resolution uncertainties is performed similarly to the smearing of the jet energy scale in case of no matched gen-jets. Random numbers following a Gaussian distribution are generated, with the width being given by the listed percentages. The energies of muons on the other hand, are shifted by the respective amount to estimate the impact of the muon momentum scale. Once again, all effects are being propagated to $E_{\mathrm{T}}^{\mathrm{miss}}$.

For the resolution, the result is a $0.2\,\%$ difference. Varying the scale yields a $+0.2\,\%$ and $-0.2\,\%$ difference for the up- and downward direction, respectively. In case of the signal Monte Carlo, the impact for the resolution goes up to $3.0\,\%$, while it only goes up to $1.0\,\%$ for the scale.

8.1.4. Muon ID Efficiency

Possible discrepancies between data and simulation when applying the tight muon ID have been researched by the Muon POG. The scale factors have been determined on the 2012 re-reconstructed datasets, which are also used in this analysis. They are below $1\,\%$ throughout the entire η-range for muons beyond the $p_{\mathrm{T}} > 20\,\mathrm{GeV}$ threshold [78].

To compensate for not scaling the number of events accordingly, a conservative $1\,\%$ systematic uncertainty for both the background as well as the signal is assumed here.

8.1.5. B-Tagging

To estimate the systematic uncertainty for the b-tagging algorithm described in section 6.8, its scale factor functions are shifted up and down. These variations are taken from the same text files linked on the corresponding website [73].

Shifting the efficiency maps only yields minor corrections. As (pseudo-)randomly generated numbers are used to determine when to up- or downgrade a jet, the statistical uncertainty overshadows the systematic one. Especially for points in the p_{T}-η-parameter space with a very low number of entries, the statistical variance is large. For these reasons, their small impact is neglected.

The effect on the smuon mass distribution is $-0.6\,\%$ for the upward variation and $+0.2\,\%$ for the downward one. Its impact on the signal lies in between $0.2\,\%$ and $1.4\,\%$.

8.2. Global Uncertainties

8.2.1. Luminosity

The offline estimate of the luminosity uses the information provided by the pixel detector. Since the high granularity allows for a very accurate measurement of the pixel clusters on which the estimate is based on, the uncertainty is comparatively low. For the 2012 datasets, it is $2.6\,\%$ [79]. It applies directly to all backgrounds as they scale linearly with it.

8.2.2. Cross sections

When determining the cross section of a process, there are two main contributions to the uncertainty of the scale: The factorization and renormalization scale. By convention, these are varied up and down by a factor of two to estimate their individual uncertainties. They are also assumed to be fully correlated.

The scale uncertainties have been provided alongside their cross sections for a sizeable portion of Monte Carlo samples. For the remainder, a conservative $50\,\%$ and $5\,\%$ uncertainty are assumed for leading order and higher order cross sections, respectively.

For all signal Monte Carlo samples, the estimates given by the authors of the cross section calculation tool are used. They amount to $5\,\%$ from the scale uncertainty and an additional $7\,\%$ from supersymmetric QCD processes [55].

8.2.3. Parton Distribution Functions

With the LHC being a *hadron* collider, the particles it accelerates have a substructure. The constituents of a proton collide and only a fraction $x_i\,(i = 1, 2)$ of the centre-of-mass energy s enters the interaction: $\hat{s} = x_1 x_2 \cdot s$. A significant part of an accurate Monte Carlo simulation is a precise description of these "partons", as the constituents are called. To obtain the cross section σ for a selected process, one has to sum over all possible partons and integrate over the energy fractions they can carry.

$$\sigma = \sum_{ij} \int_0^1 \int_0^1 \mathrm{d}x_1 \mathrm{d}x_2 f(x_1, Q^2) f(x_2, Q^2) \hat{\sigma}_{ij}(\hat{s}) \tag{8.1}$$

Here $\hat{\sigma}_{ij}$ denotes the cross section for the interaction of the partons i and j at their centre-of-mass energy $\hat{s}$. The parton density functions (**PDFs**) $f(x_i, Q^2)$ describe the probability to

find a particular parton with a certain energy fraction x_i. This likelihood also depends on the energy scale Q^2, at which the function is evaluated. PDFs have to be determined experimentally, as it is not possible to predict them from theory alone. Measurements from different experiments and different methods to estimate the evolution of the functions have been used to generate multiple sets of parton distribution functions for the LHC and other experiments. The following three are considered in this analysis to calculate the systematic uncertainty introduced by choosing a particular one [80]. Both MSTW2008 [81, 82] and CT10 [83] are optimizing their PDF fit by minimizing a log-likelihood function, while NNPDF 2.3 [84, 85] uses a template method to determine the closest match to the measurement. Exemplary distributions of MSTW2008 for two energy scales are given in figure 8.1.

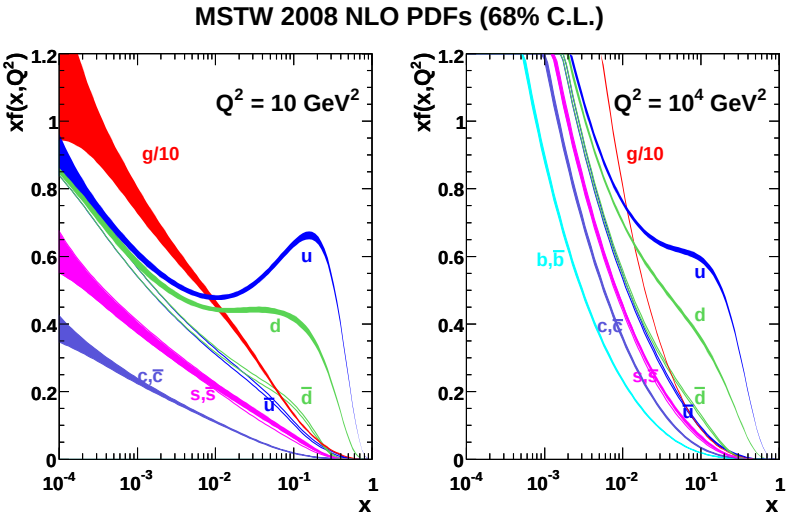

Figure 8.1.: Parton distribution functions of the MSTW2008 set at two different energy scales Q^2. The width of the bands represent the $\pm 1\sigma$-confidence intervals. The graphs are taken from the "Parton distribution functions for the LHC" publication [80].

As for theoretical uncertainties contributing to the PDFs, the dominant one stems from the strong coupling constant α_s. Due to being linked directly to the PDFs, the uncertainties on both quantities are handled similarly. For a fixed PDF, the value of α_s is varied and vice versa. The overall uncertainty is given by adding the two individual ones quadratically.

The actual application of this procedure, follows the PDF4LHC recipe for a practical implementation [86]. It is based on the general recommendations provided by the LHC4PDF Working Group [87]. The general idea is to reweight the distribution of the observable in question, as if the Monte Carlo samples were generated using a different PDF set. From the resulting deviation, one can estimate the systematic uncertainty introduced by choosing a certain set.

For the purpose of reweighting, there are numerous “members” stored in single PDF set. While the first one represents the central value, the others are variations in α_s or the PDF estimate. They are used to determine the up- and downward deviations of each member in respect to the central value. Adding the PDF and α_s variations in quadrature, yields the overall deviation in each direction. When reweighting the events for the observable, it has to be relative to the PDF set with which the sample has been generated. All Monte Carlo simulations have been created using CTEQ6L1 [88], except for the $t\bar{t}$ one. There the NLO MC generator POWHEG has been employed, which uses CT10 as its basis. Estimating the

uncertainty is done relative to the best fit, which is given by the combination of all PDF sets. Figure 8.2 shows the PDF uncertainties for all Monte Carlo samples in the smuon mass distribution at the final stage of the analysis.

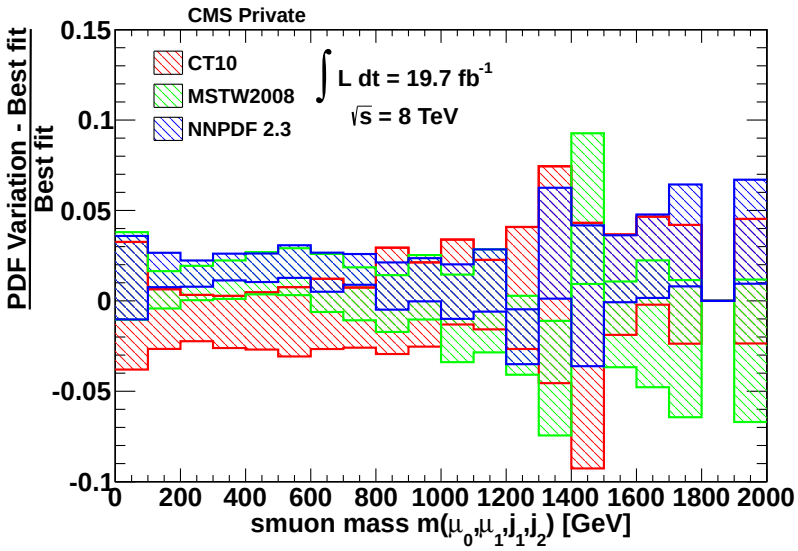

Figure 8.2.: PDF uncertainties for all background Monte Carlo samples for the smuon mass. They are given relative to the best fit calculated from the three PDF sets. The distribution is generated at the final stage of the analysis.

Towards higher masses ($\geq 1000\,\text{GeV}$) the distribution lacks the necessary number of entries to yield statistically significant results. Taking this into account, the overall systematic uncertainty introduced by PDFs is estimated to be a flat $\pm 6\,\%$.

For the signal Monte Carlo, the authors of the cross section calculation tool estimate a $5\,\%$ uncertainty [55], which is being used in this analysis.

8.2.4. Pileup

For the pileup reweighting procedure, there are mainly two systematic uncertainties that contribute to determining the number of interactions [89]. The measurement of the bunch luminosity and the total inelastic cross section. The latter has been determined through the comparing the number of vertices in $Z \to \mu\mu$ events between simulation and measurement. A $3.9\,\%$ uncertainty is attributed to this procedure. The $2.6\,\%$ error on the luminosity has already been discussed in section 8.2.1.

Additional uncertainties arise from possible shifts in the reweighting and pileup modelling processes, as well as potential beam size variations over time. They are expected to be small, but are taken into account by shifting the number of interactions by an overall amount of $\pm 5\,\%$. The impact of this shift amounts to $-1.1\,\%$ and $+1.5\%$. For the signal Monte Carlos, the effect lies between $0.3\,\%$ and $0.8\,\%$.

8.2.5. Trigger Efficiency

The performance of the trigger may vary between data and simulation. To account for this, trigger efficiency scale factors, which are the ratio between the efficiencies in Monte Carlo

and data, are determined. Figure 8.3 shows a comparison of the "turn on" curves in 2012 jet data and the $t\bar{t}$ Monte Carlo.

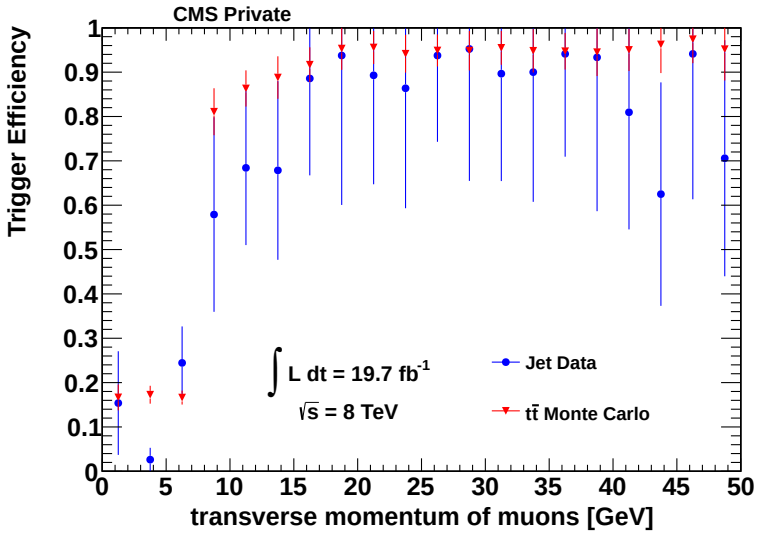

Figure 8.3.: Trigger efficiencies for 2012 jet data and $t\bar{t}$ Monte Carlo [90]. The resulting scale factor is used to account for the discrepancy. Both distributions are generated before the application of the same sign requirement, to retain a sufficiently high number of events.

Both distributions are created right before the application of the same sign charge requirement. By including the latter, one would reduce the already low statistics to a point where the result is dominated by its statistical errors. Due to the nature of this analysis, implementing scale factors for muons depending on their transverse momentum can lead to moderately complex individual event weights. To avoid this issue, keeping the transverse momentum threshold of 15 GeV for the sub-leading muon in mind, a conservative 5 % systematic uncertainty is assumed as compensation.

8.3. Fake Rate Uncertainties

Determining the tight-to-loose ratio F_R varies depending on the chosen requirements for the QCD multi-jet enrichment of the sample. To estimate the systematic uncertainty introduced by this method, a single quantity is varied, while the others are kept constant. As opposed to the previously discussed systematic uncertainties, the impact on the number of events can be within the expected statistical variation. Should this be the case, it cannot be considered a systematic uncertainty. Calculating the variation is based on how the relative systematic uncertainty σ_{sys} is determined. With the number of events from the default method as a reference N_{def} and the one from the variation denoted by N_{var}, it is given by

$$\sigma_{\text{sys}} = \frac{N_{\text{var}} - N_{\text{def}}}{N_{\text{def}}}. \tag{8.2}$$

The statistical uncertainty then follows as

$$\sigma_{\text{stat}} = \frac{\sqrt{\sigma_{\text{var}}^2 - \sigma_{\text{def}}^2}}{N_{\text{def}}}. \tag{8.3}$$

Note that one would usually expect the σ to be *added* in quadrature. However, this uncertainty would correspond to the number of events instead of the method itself. Since these values are strongly correlated, they are required to be subtracted.

Table 8.1 shows the results of the variations.

Quantity	Variation	Impact on estimate [%]
Comb. Rel. Iso.	0.2	3.7 ± 21.7
(default $< 0.5\,\text{GeV}$)	0.4	1.7 ± 4.6
	0.8	4.0 ± 4.9
	1.0	5.1 ± 5.4
$p_{\text{T, jet}}$	40	7.6 ± 3.9
(default $> 50\,\text{GeV}$)	60	-5.8 ± 3.1
	70	-9.3 ± 3.6
$E_{\text{T}}^{\text{miss}}$	40	0.6 ± 0.5
(default $< 50\,\text{GeV}$)	60	-0.9 ± 1.4
	70	-2.1 ± 2.1
$m_{\text{T}}(\mu, E_{\text{T}}^{\text{miss}})$	30	-3.8 ± 2.4
(default $< 40\,\text{GeV}$)	50	8.6 ± 4.3
	60	14.2 ± 5.9

Table 8.1.: Parameter variations to determine the systematic uncertainties of determining the fake rate F_R. Only one requirement is varied at a time. The expected statistical deviation has to be kept in mind.

Only the listed quantities are examined. All of the other ones are motivated by trigger thresholds or analysis requirements. For example the transverse momenta thresholds for muons are restricted by the choice of the trigger and the dimuon mass window is limited by low mass resonances and the Z-peak. For the overall impact, the variations of the transverse momentum of jets and the transverse mass hypothesis are considered. For a given quantity, the average is taken and added in quadrature to the overall sum. With the combined relative isolation and missing transverse energy only yielding impacts which are within the expected variation, they do not contribute.

8.3.1. Closure Test

To quantify the difference between the tight-to-loose ratio F_R of the recorded data and the Monte Carlo prediction of the ratio given by the QCD multi-jet background (Fig. 7.3), a "closure test" is used. It provides a test of concept for the data-driven background method, as well as being an indicator for the accuracy of the MC prediction. The general idea is to apply the tight-to-loose ratio F_R to a chosen background and compare the result to its Monte Carlo prediction. A comparison between the tight-to-loose ratios measured in data and the QCD multi-jet counterpart it is meant to be similar to, yields the aforementioned quality estimate for the method itself. Since the $t\bar{t}$ background is the most prominent one in the final stage of the analysis, it is used as the benchmark process in this test. Figure 8.4 shows both the proof of concept on the left, as well as the actual comparison on the right.

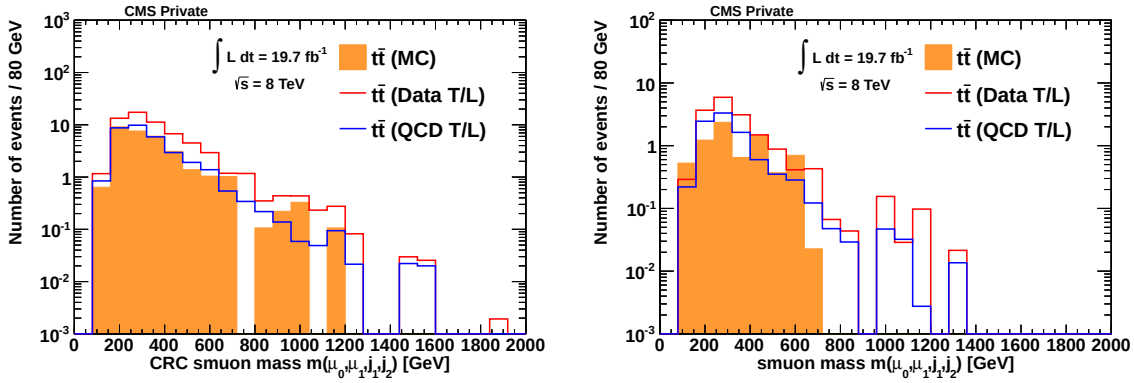

(a) (b)

Figure 8.4.: Proof of concept provided by the closure test (8.4a) and comparison between QCD multi-jet and data tight-to-loose ratios F_R in the smuon mass distribution (8.4b). Both distributions show the Monte Carlo prediction, as well as both the QCD multi-jet and the data tight-to-loose ratio applied to it. While the right distribution was filled at the final stage, the left one is filled at charge control region, without a b-jet veto.

To provide a proof of concept for the fake rate method, the charge control region is being used. Aside from the typical inverted $E_{\mathrm{T}}^{\mathrm{miss}}$ requirement, it is characterised by not applying the b-jet veto while requiring the same charge one. For the proof, the QCD multi-jet tight-to-loose ratio is measured and applied to the $t\bar{t}$ background. It is shown alongside the corresponding $t\bar{t}$ Monte Carlo. Note that the ratio measured in data cannot be used here, as the previously observed difference to the Monte Carlo tight-to-loose ratio already implies a differing result. The good agreement between the QCD multi-jet F_R and MC prediction that can be seen in figure 8.4a, is an indication for the quality of the method itself.

The actual comparison of the results of applying both the data and the QCD multi-jet tight-to-loose ratio to the $t\bar{t}$ background is shown in figure 8.4b. Since one initially expected comparable results from both predictions, their disagreement of 45 % in the number of events is taken as a systematic uncertainty.

While all previously discussed uncertainties apply to the Monte Carlo samples that are used for the statistical subtraction, their overall impact is reduced significantly. As they affect *both* the number of tight and loose muons, calculating the ratio absorbs a large portion of this impact. Since the relative contributions of the individual uncertainties to the tight and loose subsets are similar, they only play a comparatively minor role.

Taking the second order effects from the Monte Carlo subtraction and the luminosity uncertainty for the *data*-driven estimate into account, a 47 % systematic uncertainty is assumed for the fake rate method.

8.4. Summary

In table 8.2, the systematic uncertainties on the overall number of events are summarized. From the individual impacts of the up- and downward variations, the larger value has been taken to remain conservative.

Source of sys. uncertainty	Background Impact [%]	Signal Impact [%]
Jet Energy Resolution	0.6	2.6
Jet Energy Scale	3.6	7.8
Muon Momentum Resolution	0.2	1.0
Muon Momentum Scale	0.2	3.0
Muon ID Efficiency	1.0	1.0
B-Tagging	0.6	1.4
Luminosity	2.6	2.6
Parton Distribution Functions	6.0	5.0
Cross sections	17.3	8.6
Pileup	1.5	0.8
Trigger Efficiency	5.0	5.0
$\sum$	19.6	14.6
Data-driven Background Estimate	47.0	N/A

Table 8.2.: Summary of all systematic uncertainties. The cross section uncertainties are either listed in table 4.2 or assumed to be 5 and 50 percent for a higher order and a LO calculation, respectively. Here, the average impact of the cross section uncertainties on the smuon distribution is given.

Chapter 9

Results

9.1. Candidate Event

To summarize the event selection, an event that has been recorded by the CMS detector is being shown in figure 9.1. Muons below the minimum transverse momentum of 20 GeV and jets below the minimum energy of 30 GeV have been removed. The event passed all selection requirements and visualizes the most important aspects of it. Both muons are highly energetic and well isolated, as they are reasonably separated from the various jets. The number of jets exceeds the minimum of two, while the highest two jet energies also surpasses the threshold by quite a margin. With the low amount of missing transverse energy that is needed to pass the upper limit of 50 GeV, the red arrow representing this quantity is barely noticeable. The two muon and two jet candidates result in an invariant mass of 229 ± 19 GeV corresponding to the smuon $m_{\tilde{\mu}}$. Removing the leading muon from this invariant mass calculation yields 186 ± 18 GeV, which is the gaugino mass $m_{\tilde{\chi}_1^0}$. To determine the uncertainties on the masses, the muon and jet Lorentz-vectors have been shifted by the respective uncertainties of the momentum scale and resolution.

9.2. Final Distribution

Having accounted for the systematic uncertainties, one can examine the final distribution(s). This encompasses the mass of the gaugino and smuon. In case of the smuon, the selected two jets and the two muons enter the invariant mass calculation. Removing the leading muon from this composition yields the gaugino case. All event selection requirements are applied and in relation to the b-jet veto plus charge control region, only the missing transverse energy requirement is reversed to be $E_{\mathrm{T}}^{\mathrm{miss}} < 50$ GeV again. Figure 9.2 shows both distributions including the data-driven background estimate.
Table 9.1 resolves each group of processes into its individual background components. The importance of the data-driven background estimate is shown by its large contribution. It is roughly twice as high as the biggest Monte Carlo sample contribution given by the $WZ \to 3l\nu$ process. Together, they amount to more than 80 % of the entire background prediction.

The statistical uncertainties for the Monte Carlo predictions stem from the generated number of events, which limit the accuracy of the prediction. While the fake estimate has been determined from data, the method itself inherits statistical uncertainties from the background samples which are subtracted from the data when determining the tight-to-loose ratio. Adding the uncertainties for every bin of the single- and double-fake estimates in quadrature

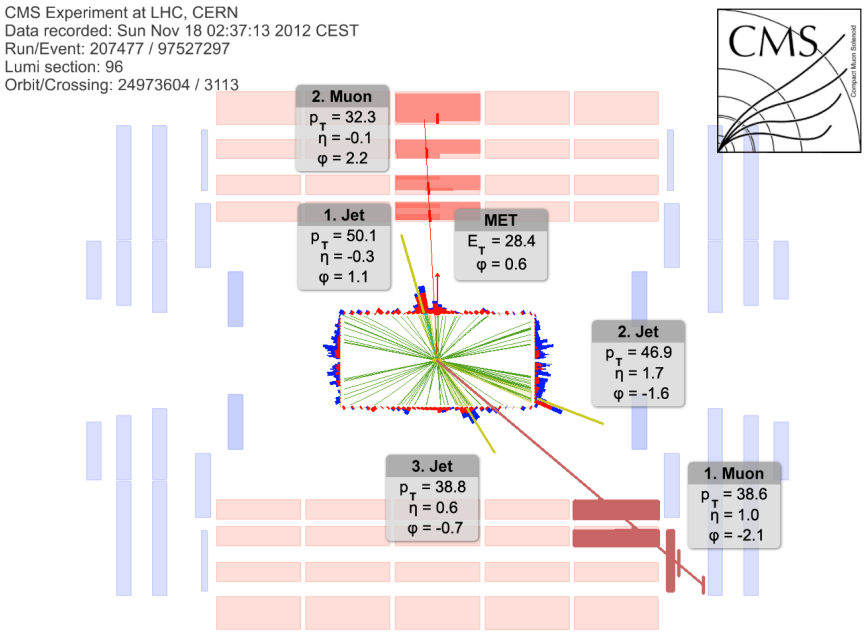

(a)

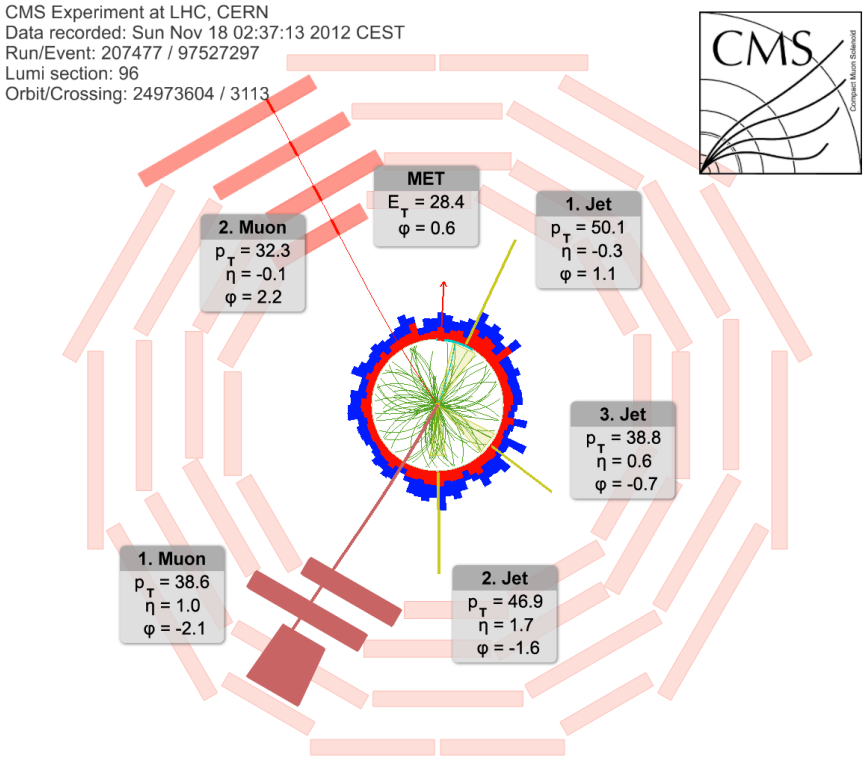

(b)

Figure 9.1.: Signal-like event candidate detected by the CMS. Shown are both the η-z- (9.1a) and the ϕ-r-plane (9.1b).

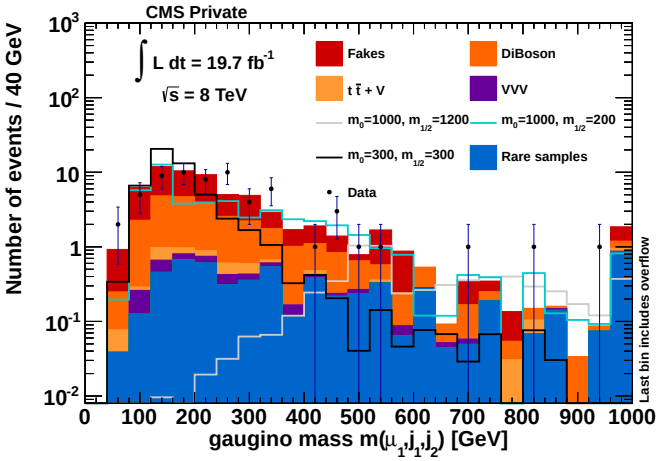

(a)

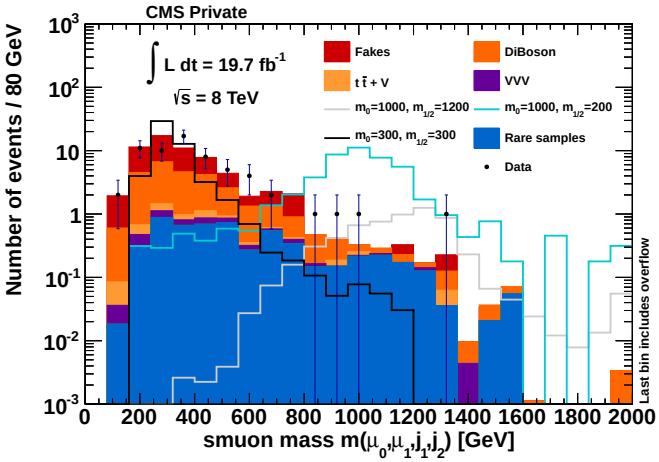

(b)

Figure 9.2.: Mass of the gaugino (9.2a) and smuon (9.2b) after all selection requirements. Both are calculated from the invariant masses of the selected two jets and two muons in the smuon case, as well as two jets and the sub leading muon for the gaugino. The distributions include the data-driven background estimate.

and propagating them according to equation (7.4), yields the statistical uncertainty for this case. All systematic uncertainties are taken from the summary table (Tab. 8.2). Individual cross section uncertainties are included in accordance to the table's description as well. Overall one can observe an excellent agreement of measurement and SM simulation.

Taking the signal point with $m_0 = 1000\,\text{GeV}$ and $m_{1/2} = 200\,\text{GeV}$ in figure 9.2 as an example, one can see that while the distributions coincide in the gaugino mass distribution, they do not in the smuon one. A two-dimensional visualization of the two exemplary signal contributions in the gaugino-smuon mass distribution is shown in figure 9.3. In general, the dominant search region for a RPV SUSY signal depends on the values of m_0 and $m_{1/2}$. To improve the sensitivity of the limit setting procedure, a multi-bin approach is being employed. For that purpose the two-dimensional gaugino-smuon mass distribution is divided into six regions SR 1-6. Figure 9.4 shows the two-dimensional, final distribution of the smuon and

Sample	N_{Events}	Uncertainties	
		stat.	sys.
Data-driven background estimate	33.5	2.4	16.0
Monte Carlo			
$W\gamma \to l\nu 2\mu$	1.35	0.45	0.69
$WZ \to 3l\nu$	17.1	0.5	1.9
$WZ \to 2ql\nu$	0.026	0.026	0.003
$ZZ \to 2l2q$	0.044	0.030	0.0044
$ZZ \to 4l$	2.55	0.05	0.27
$t\bar{t} + W$	1.00	0.16	0.30
$t\bar{t} + WW$	0.0163	0.0019	0.0083
$t\bar{t} + Z$	0.258	0.070	0.038
WWW	0.842	0.081	0.085
WWZ	0.186	0.034	0.02
WZZ	0.186	0.013	0.001
ZZZ	0.0554	0.0018	0.0005
W^-W^-	1.38	0.17	0.7
W^+W^+	3.97	0.48	2.02
WW Double-parton	0.24	0.07	0.12
$\sum$ Background estimate	62.5	2.6	22.1
Data	63	-	-

Table 9.1.: Detailed number of events for each background in the distributions at the final stage of the analysis.

gaugino mass.
While the the smuon mass axis extends further than 1.4 TeV, only a portion is shown to avoid cluttering in the low mass region. Most entries are centered around one diagonal line, as a opposed to the previously shown signal samples. While some of the data points seem to stray quite far from the diagonal, they are not significant. This can be seen by examining the contents of each of the six regions, which are summarized in table 9.2.

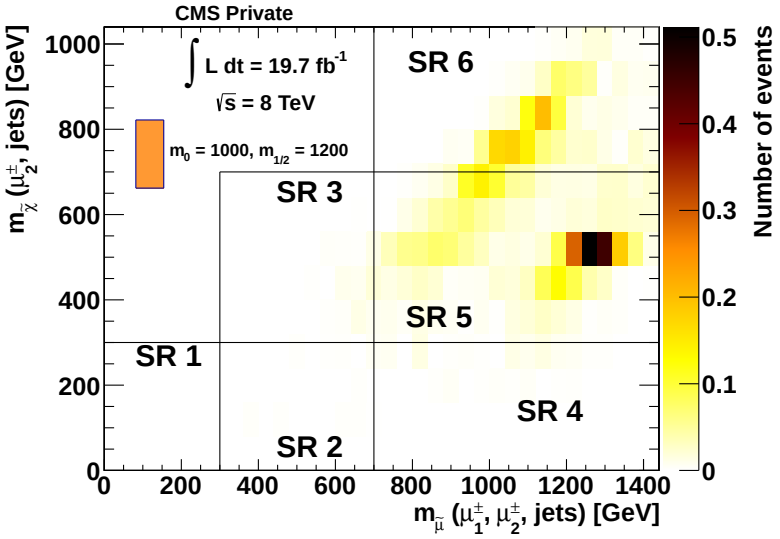

(a)

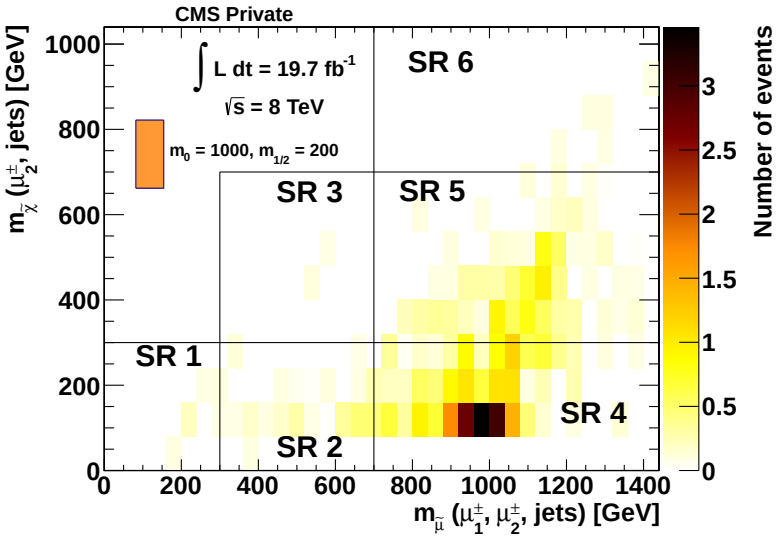

(b)

Figure 9.3.: Two-dimensional smuon and gaugino mass distribution. Only the listed signal is shown. One can see that m_0 and $m_{1/2}$ determine which out of the six search regions SR 1-6 is the dominant one. The black lines represent the borders of the individual search regions.

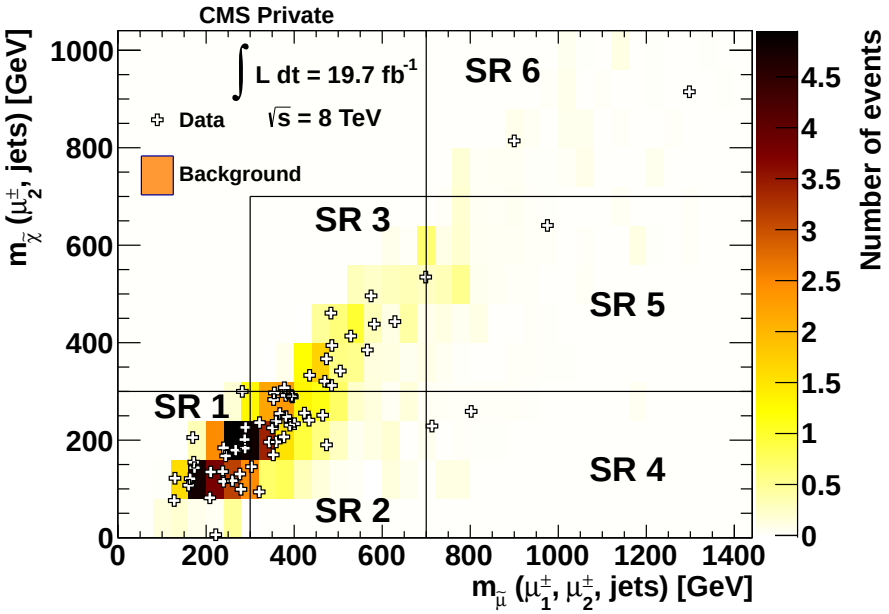

Figure 9.4.: Background estimate and CMS data of the two-dimensional smuon and gaugino mass distribution. All backgrounds are summed up and are shown as coloured search regions, while the data points are shown individually. The six bins are regarded as separate search regions SR 1-6 to improve the results of this analysis. The black lines represent the borders of the individual search regions.

Process group	SR 1		SR 2		SR 3	
Fake Estimate	16.0	± 7.8	10.7	± 5.3	5.00	± 2.58
$tt + V$	0.47	± 0.16	0.49	± 0.17	0.187	± 0.089
VV	8.46	± 1.22	7.1	± 1.1	4.01	± 0.62
VVV	0.374	± 0.064	0.392	± 0.066	0.209	± 0.045
Rare	1.04	± 0.57	1.33	± 0.72	1.65	± 0.88
$\sum$	26.4	± 9.6	20.0	± 7.1	11.1	± 4.0
Data	19		25		13	
Process group	SR 4		SR 5		SR 6	
Fakes Estimate	0.23	± 0.20	1.15	± 0.89	0.33	± 0.25
$tt + V$	< 0.001		0.032	± 0.029	0.094	± 0.062
VV	0.106	± 0.034	1.07	± 0.16	0.277	± 0.062
VVV	0.0062	± 0.0048	0.090	± 0.027	0.028	± 0.014
Rare	0.102	± 0.089	0.65	± 0.38	0.80	± 0.46
$\sum$	0.45	± 0.25	3.0	± 1.3	1.5	± 0.7
Data	2		1		3	

Table 9.2.: Summary of the six regions displayed in figure 9.4. They are numbered starting on the left and progressing upwards from the lowest bin. Statistical and systematic uncertainties are added in quadrature.

9.3. Calculation of Limits

As any excess of data is too small to be considered statistically significant, the result is translated into limits onto two quantities. The cross section of a R-parity violating supersymmetry model and its model parameter λ'_{211}. To calculate these, one method commonly used in the CMS experiment will be utilized. Details are given in the upcoming section.

9.3.1. CLs Method

The CL_s method [91, 92] is a modified frequentist analysis. Simple hypothesis tests may exclude possible (small) signal contributions based on downward fluctuations of the measurement in cases with low statistics. The CL_s method, however, yields meaningful results in these circumstances. Its general idea is to compare two hypotheses to a measurement.

For most analyses in high energy particle physics, there are two cases to be covered. The null hypotheses H_0 being the Standard Model prediction by itself and a combination of the proposed signal and the Standard Model prediction as the second hypothesis H_1. In the most simple case, one expects the number of events n to follow a Poisson distribution.

$$\mathcal{L}(x;n) = \frac{x^n}{n!}e^{-x} \tag{9.1}$$

These likelihoods $\mathcal{L}_x$ are the basis for this method. Here, x denotes the background-only scenario for $x = b$ and the background plus signal one for $x = s + b$. The distributions are ultimately a function of the cross section of the relevant processes, as it is proportional to the number of selected events n.

Using the two likelihood functions, a test statistic Q can be defined. It is called the *likelihood-ratio* and is used to judge how well a hypothesis describes the measurement. In the simplest case, it is given by

$$Q = -2\ln\frac{\mathcal{L}(s+b;n)}{\mathcal{L}(b;n)}. \tag{9.2}$$

Large values of Q correspond to a better agreement with H_1, while small ones to a better agreement with H_0. For a result of an actual experiment, the observed number of events n_{obs} yields a set likelihood-ratio Q_{obs}. The confidence level for an hypothesis is defined as the probability P to find a test statistic Q, which is less or equal to Q_{obs}.

$$CL_x = P(Q \leq Q_{obs}). \tag{9.3}$$

To determine this probability P, one has to integrate over all possible Qs up to Q_{obs}.

$$CL_x = \int_{-\infty}^{Q_{\text{obs}}} \frac{df_x(Q)}{dQ}\mathrm{d}Q \tag{9.4}$$

The probability distribution functions are denoted by $f_x(Q)$ and are determined through pseudo-experiments. For a very well understood background hypothesis, a confidence level in the null hypothesis close to one $CL_b(Q_{\text{obs}}) \approx 1$ is necessary to claim a discovery. The specific thresholds for the claim are given on $1 - CL_b(Q_{\text{obs}})$ and have been derived from standard deviations of the Gaussian distribution. This means $2.7 \cdot 10^{-3}$ corresponds to $3\,\sigma$, which is considered "evidence", and $5.7 \cdot 10^{-5}$ corresponding to $5\,\sigma$, a discovery.

Excluding the signal (plus background) hypothesis uses the eponymous CL_s quantity instead of CL_{s+b}. It is defined as a ratio:

$$CL_s = \frac{CL_{s+b}}{CL_b}. \tag{9.5}$$

While CL_{s+b} may lead to unphysical results in certain cases, CL_s does not. A prime example is a signal hypothesis that is dominated by its background. Slight fluctuations towards lower values of the latter would lead to a very low CL_{s+b}, yielding a strong exclusion limit. As CL_s is not a confidence limit, but a ratio of those, fluctuations like these cancel themselves out.

A signal can be excluded at a confidence level CL, when the following relation is fulfilled.

$$1 - CL_s \leq CL \tag{9.6}$$

9.4. Modifications

Following the recommendations by the CMS and ATLAS collaborations [93], a modified test statistic is employed for the CL_s method. To scale the signal strength, a parameter μ is introduced to the formula. It is used to in- or decrease the cross section of the signal prediction while the branching ratios remain constant. Additionally, both the signal and background simulation are subject to a number of uncertainties. In this analysis, the systematic uncertainties discussed in chapter 8 are considered. These include detector based uncertainties, such as the energy resolution of jets, theoretical uncertainties, for example the accuracy of cross section calculations, and physics object identification uncertainties, like the ability to accurately determine the flavour of a jet. Additionally, the accuracy of the Monte Carlo simulation, which is limited by its simulated number of events, is also taken into consideration. To account for those in the limit calculation, a set of nuisance parameters θ is introduced.

$$Q = -2 \ln \frac{\mathcal{L}(\mu s + b; n, \hat{\theta})_\mu}{\mathcal{L}(\hat{\mu} \cdot s + b; n, \hat{\theta})} \quad \text{with} \quad 0 \leq \hat{\mu} \leq \mu \tag{9.7}$$

Here, the pair of parameters $\hat{\mu}$ and $\hat{\theta}$ are evaluated at the global maximum of the likelihood. On the other hand, $\hat{\theta}_\mu$ denotes the conditional maximum likelihood estimator of θ, which also depends on the choice of μ. The lower constraint $0 < \hat{\mu}$ ensures that the signal has a positive contribution[1]. To prevent upward fluctuations of the measurement ($\hat{\mu} > \mu$) to be considered evidence *against* the signal hypothesis, the upper constraint $\hat{\mu} < \mu$ is set.

To improve the limits, the search region is subdivided into multiple search regions. When combining the results for the individual regions, the respective likelihoods have to be multiplied and the overall value is given by

$$\mathcal{L} = \prod_i \mathcal{L}_i. \tag{9.8}$$

This enhances the sensitivity, as the influence of large deviations in one region is increased.

[1] While certain signals can lead to a negative interference, these are not covered by the CL_s method.

9.5. Limit Graphs

The actual calculation of limits is performed by the HiggsCombine tool [93, 94]. It employs the RooStats package [95] which is part of the statistical analysis framework ROOT. In line with most CMS publications, the exclusion ranges are calculated at a 95 % confidence level as an upper limit on the cross section ($CL_s \leq 0.05$). The necessary scaling of the signal strength to reach this CL can be achieved through varying the previously introduced modifier μ. This has to be done for each of the individual points in the RPV SUSY phase space.

While the result of the calculation is a limit on the signal cross section σ, it can be translated into a limit onto the model parameter λ'_{211}. As the former scales quadratically with the latter, the following formula has to be used.

$$\sigma \propto \lambda'^2_{211} \Rightarrow \lambda'_{211}(95\,\%\,CL) = \lambda'_{211} \cdot \sqrt{\frac{\sigma(95\,\%\,CL)}{\sigma}} \tag{9.9}$$

The respective 95 % CL multi-bin upper cross section limits, which have been translated into limits on the model parameter λ'_{211} are displayed as a function of m_0 and $m_{1/2}$ in figure 9.5 and as a function of $m_{\tilde{\mu}}$ and $m_{\tilde{\chi}^0}$ in this RPV model in figure 9.6. One should note that, while $m_{\tilde{\chi}^0}$ corresponds to the LSP right before its RPV decay, $m_{\tilde{\mu}}$ represents the initial supersymmetric particle. Consequently, the sneutrino case $m_{\tilde{\nu}}$ is also included. As explained in the signal study (Cha. 3), the LSP might be the product of prior RPC decays from the smuon, instead of being a direct decay product. With this in mind, one has to be careful when interpreting the latter two limit graphs.

9.6. Discussion and Interpretation

Comparing the shown limits to the analyses of 2011 RPV SUSY by CMS (Fig. 1.11b) and the D0 predecessor (Fig. 1.11a), the phase space that is being covered has been expanded considerably. As mentioned in section 1.2.5, the ATLAS collaboration has not published any comparable limits. Their search for long-lived, heavy particles with a muon and a displaced vertex [22] is sensitive to lower values of λ'_{2ij}. Due to their simplified model approach, it is difficult to compare their results to the ones of this analysis.

The excluded values of λ'_{211} are roughly a factor of 10 better than the ones presented by D0 [19, 21], and around a factor of 1.8 in regards to the 2011 analysis [20]. This marks these results as the world's best collider-based limits on the R-parity violating supersymmetry scenario with a single coupling dominance of the λ'_{211} parameter.

In general, the exclusion limits get progressively weaker towards higher values of m_0. As shown in figure 4.3, the cross section for the interesting processes decreases in this region. However, there is also a drop in selection efficiency for the high mass signal points. This is due to changes in the particle properties and composition of the decay chain. These differences have been mentioned and illustrated in the event selection (Fig. 6.1), by providing three exemplary signal points as a comparison in the various distributions.

By taking one dimensional slices out of the m_0-$m_{1/2}$ plane of the limits, one can see the evolution of the limits with regards to their uncertainties (Fig. 9.7). There are no rogue values deviating too much from the expectation, but certain structures can be observed. These are the product of the universal mass parameters leading to certain smuon and gaugino masses, corresponding to one or two of the search regions. Using the phase space point with $m_0 = 1000\,\text{GeV}, m_{1/2} = 1200\,\text{GeV}$ as an example, one can see in figure 9.3a that its

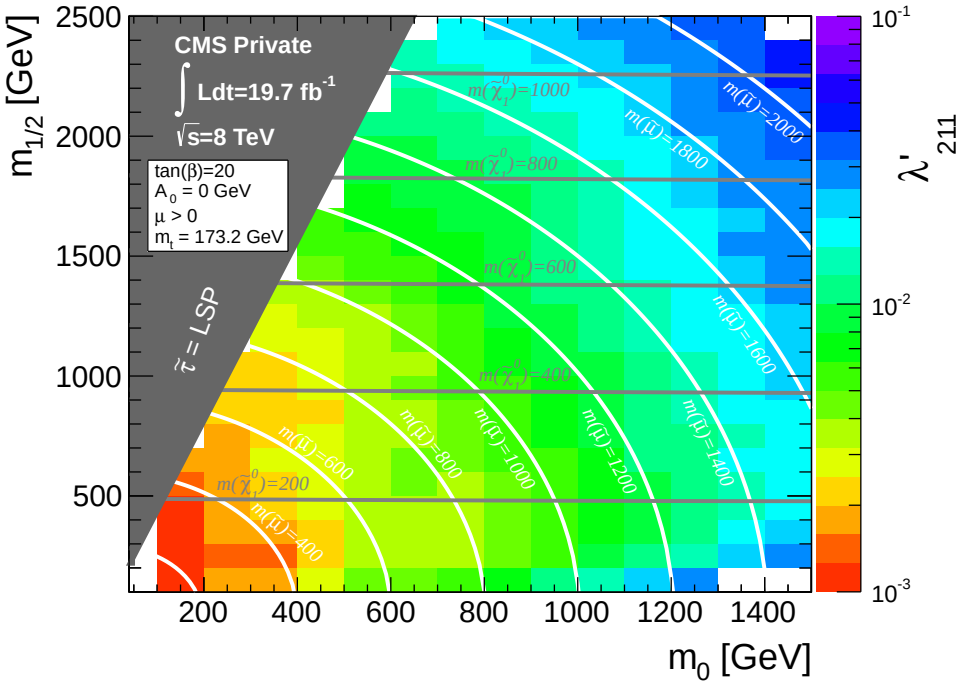

(a)

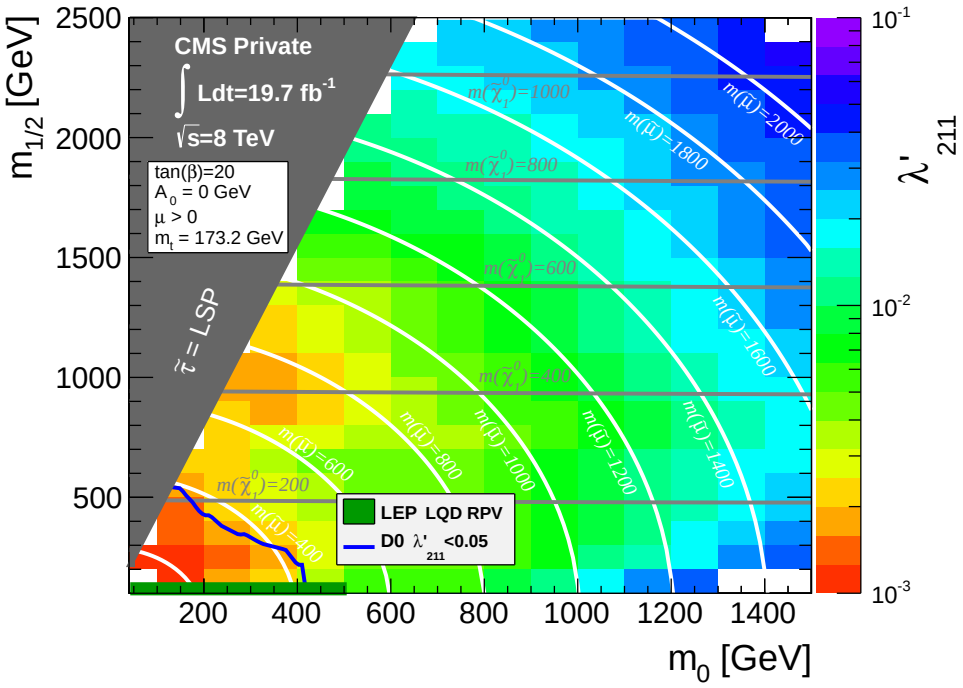

(b)

Figure 9.5.: Expected (9.5a) and observed (9.5b) 95 % CL upper limits on the λ'_{211} coupling. They are given as a function of m_0 and $m_{1/2}$, while the parameters $A_0 = 0\,\text{GeV}$, $\text{sgn}(\mu) = +1$ and $\tan\beta = 20$ are fixed. The white regions to the left are part of the $\tilde{\tau}$-LSP phase space, to which this analysis is not sensitive. In the white regions on the bottom, the model has non-converging RGEs, no electroweak symmetry breaking or tachyonic solutions.

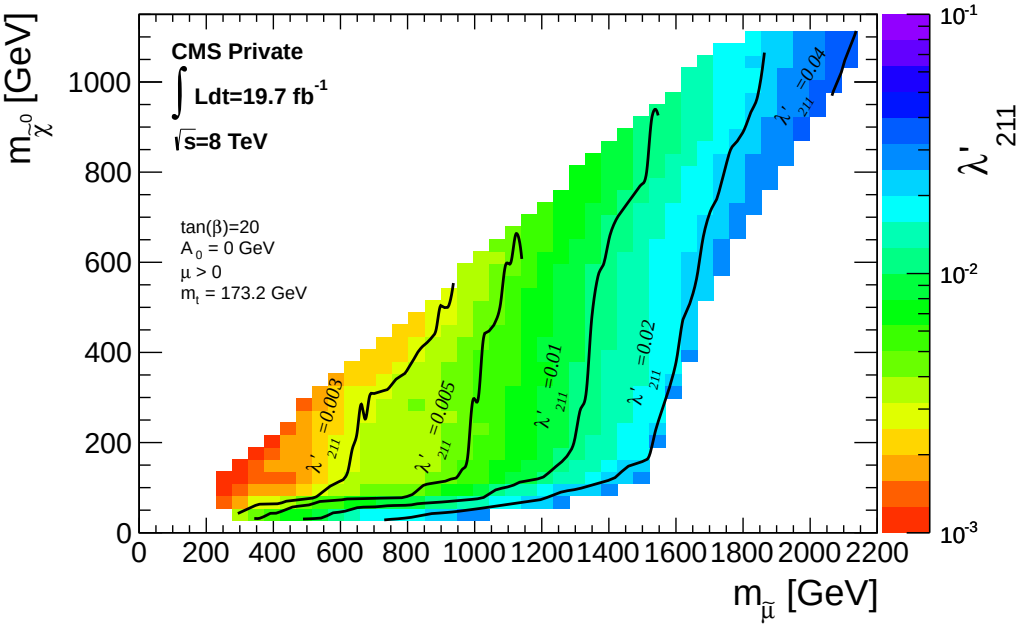

(a)

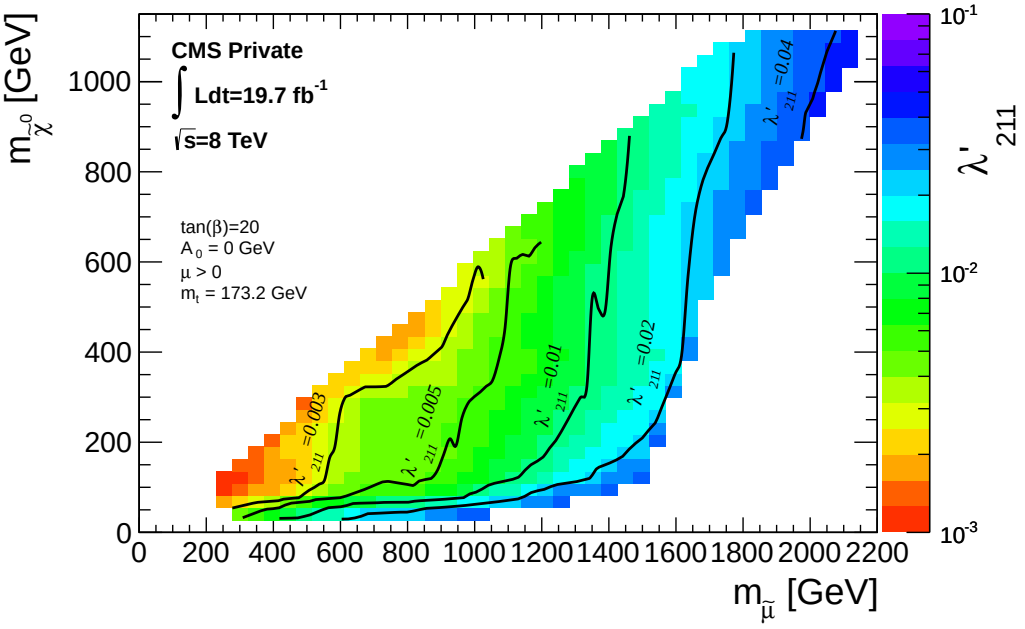

(b)

Figure 9.6.: Expected (9.6a) and observed (9.6b) 95 % CL upper limits on the λ'_{211} coupling. They are given as a function of $m_{\tilde{\mu}}$ and $m_{\tilde{\chi}^0}$, while the parameters $A_0 = 0\,\text{GeV}$, $\text{sgn}(\mu) = +1$ and $\tan\beta = 20$ are fixed.

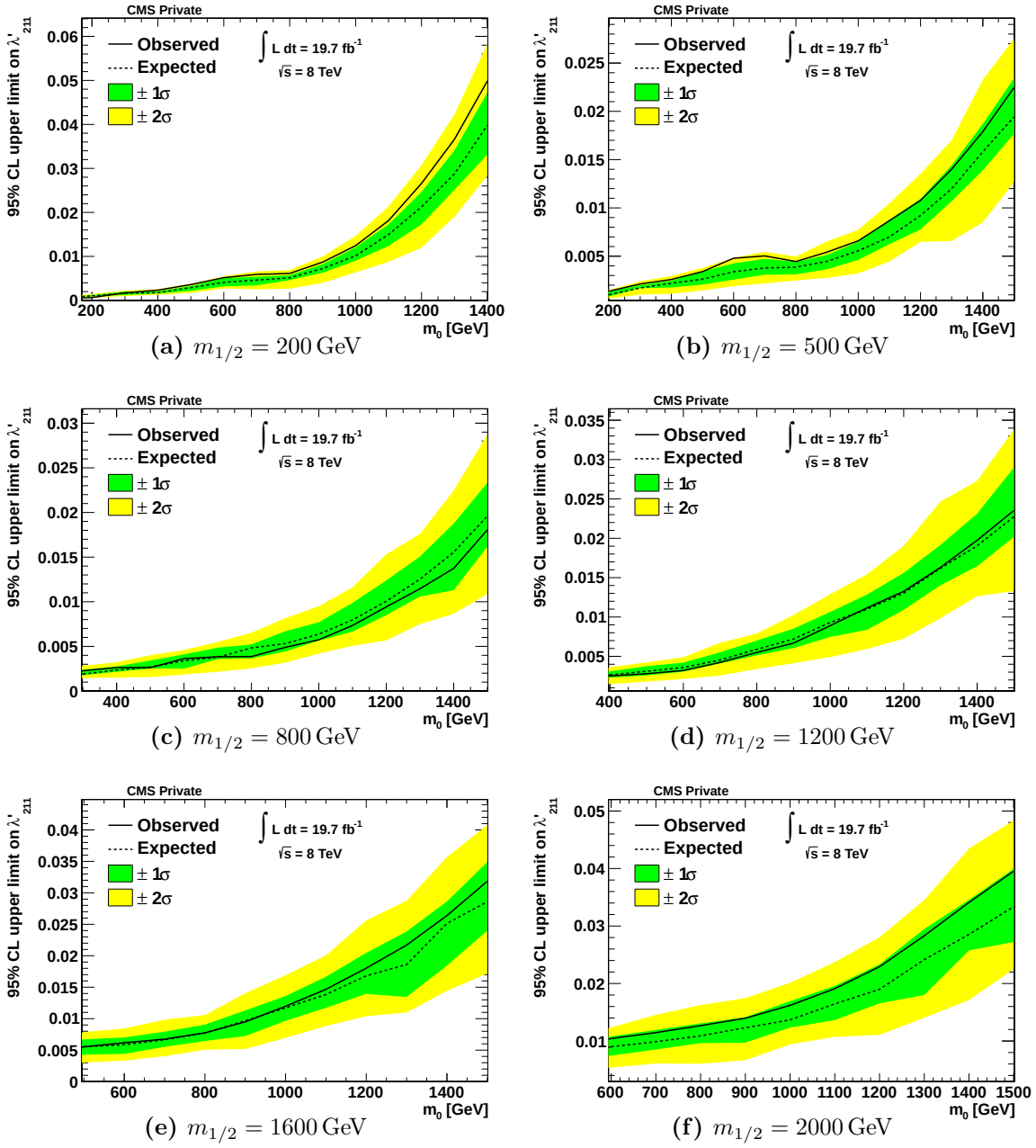

(a) $m_{1/2} = 200\,\text{GeV}$ (b) $m_{1/2} = 500\,\text{GeV}$

(c) $m_{1/2} = 800\,\text{GeV}$ (d) $m_{1/2} = 1200\,\text{GeV}$

(e) $m_{1/2} = 1600\,\text{GeV}$ (f) $m_{1/2} = 2000\,\text{GeV}$

Figure 9.7.: One dimensional slices of the two-dimensional limits given in figure 9.5 for fixed values of $m_{1/2}$. The one and two sigma bands include both statistical and systematic uncertainties.

distribution has its main contribution in the SR 5, where data and MC are in reasonable agreement. Hence, the observed and expected limit (Fig. 9.7d) are very close to each other. For $m_0 = 1000\,\text{GeV}, m_{1/2} = 200\,\text{GeV}$ on the other hand, the slight excess of data in the corresponding SR 4 leads to an observed limit that is a worse than the expectation, but still within 2σ (Fig. 9.7a).

9.7. Conclusion and Outlook

A search for resonant production of second generation sleptons via single coupling dominance of the λ'_{211} parameter has been presented. For this purpose, the full $\mathcal{L} = 19.7\,\text{fb}^{-1}$ of double muon events recorded by the CMS experiment at proton-proton collisions with a centre-of-mass energy of $\sqrt{s} = 8\,\text{TeV}$, is being used. The final state in question is composed of two well isolated, same-sign muons and at least two jets. An additional characteristic of the signature is a low amount of missing transverse energy, which is atypical for common SUSY events. As no significant excess of data has been observed in comparison to the Standard Model's prediction, the best limits to date have been set on the model parameter λ'_{211} down to values of 10^{-3}. They cover a range of up to 2.5 TeV for the universal mass parameter of scalar particles m_0 and up to 1.5 TeV for the universal mass parameter of fermionic particles $m_{1/2}$. A complementary expression through the mass of the smuon $m_{\tilde{\mu}}$ and gaugino $m_{\tilde{\chi}^0}$ in this model has also been provided.

For future efforts in this particular search, an improved selection efficiency for the signal could be achieved through taking the varying signature distributions of different RPV SUSY phase space points into account. This would require either fully flexible or individually adjusted thresholds for specific regions of the m_0-$m_{1/2}$-phase space.

In addition, results allowing for a broader interpretation beyond the cMSSM using "simplified models", based on the knowledge gained about the most important decay channels, are also possible and being investigated.

Acknowledgements

I offer my sincerest gratitude to both my family and my institute. Amongst the many people who helped me along the way, there are some which I would like to highlight. First of all, Professor Thomas Hebbeker, who enabled me to develop my thesis at his institute. Martin Weber, who supervised me throughout most of my work and introduced me to my new best friend "Emacs". Sebastian Thüer, who vigorously endured my constant nagging and questioning. Arnd Meyer, the voice of wisdom in times of need. Lars Sonnenschein, who was always eager to push for results. Andreas Güth, miracle worker at the monstrosity called Monte Carlo generators. Daniel Teyssier, at efficiently working on efficiencies. My parents for allowing me to get this far and their omnipresent all around support. And everyone working at the institute, who all contribute to the work-oriented and yet relaxing atmosphere, allowing for an enjoyable experience throughout my time there.

Appendix A
Paths of Monte Carlo Samples

Monte Carlo Samples	N_{Events}
DYJetsToLL_M-10To50filter_8TeV-madgraph_Summer12_DR53X-PU_S10_START53_V7A-v1SIM	7132223
DYJetsToLL_M-50_TuneZ2Star_8TeV-madgraph-tarball_Summer12_DR53X-PU_S10_START53_V7A-v1SIM	30459503
QCD_Pt-15to20_MuEnrichedPt5_TuneZ2star_8TeV_pythia6_Summer12_DR53X-PU_S10_START53_V7A-v2SIM	1722681
QCD_Pt-20to30_MuEnrichedPt5_TuneZ2star_8TeV_pythia6_Summer12_DR53X-PU_S10_START53_V7A-v1SIM	8486904
QCD_Pt-30to50_MuEnrichedPt5_TuneZ2star_8TeV_pythia6_Summer12_DR53X-PU_S10_START53_V7A-v1SIM	9560265
QCD_Pt-50to80_MuEnrichedPt5_TuneZ2star_8TeV_pythia6_Summer12_DR53X-PU_S10_START53_V7A-v1SIM	10365230
QCD_Pt-80to120_MuEnrichedPt5_TuneZ2star_8TeV_pythia6_Summer12_DR53X-PU_S10_START53_V7A-v1SIM	9238642
QCD_Pt-120to170_MuEnrichedPt5_TuneZ2star_8TeV_pythia6_Summer12_DR53X-PU_S10_START53_V7A-v1SIM	8501935
QCD_Pt-170to300_MuEnrichedPt5_TuneZ2star_8TeV_pythia6_Summer12_DR53X-PU_S10_START53_V7A-v1SIM	7669947
QCD_Pt-300to470_MuEnrichedPt5_TuneZ2star_8TeV_pythia6_Summer12_DR53X-PU_S10_START53_V7A-v1SIM	7832261
QCD_Pt-470to600_MuEnrichedPt5_TuneZ2star_8TeV_pythia6_Summer12_DR53X-PU_S10_START53_V7A-v1SIM	3783069
QCD_Pt-600to800_MuEnrichedPt5_TuneZ2star_8TeV_pythia6_Summer12_DR53X-PU_S10_START53_V7A-v1SIM	4119000
QCD_Pt-800to1000_MuEnrichedPt5_TuneZ2star_8TeV_pythia6_Summer12_DR53X-PU_S10_START53_V7A-v1SIM	4107853
QCD_Pt-1000_MuEnrichedPt5_TuneZ2star_8TeV_pythia6_Summer12_DR53X-PU_S10_START53_V7A-v1SIM	3873970
Tbar_s-channel_TuneZ2star_8TeV-powheg-tauola_Summer12_DR53X-PU_S10_START53_V7A-v1SIM	139974
T_s-channel_TuneZ2star_8TeV-powheg-tauola_Summer12_DR53X-PU_S10_START53_V7A-v1SIM	259961
Tbar_t-channel_TuneZ2star_8TeV-powheg-tauola_Summer12_DR53X-PU_S10_START53_V7A-v1SIM	1935072
T_t-channel_TuneZ2star_8TeV-powheg-tauola_Summer12_DR53X-PU_S10_START53_V7A-v3SIM	99876
Tbar_tW-channel-DR_TuneZ2star_8TeV-powheg-tauola_Summer12_DR53X-PU_S10_START53_V7A-v1SIM	493460
T_tW-channel-DR_TuneZ2star_8TeV-powheg-tauola_Summer12_DR53X-PU_S10_START53_V7A-v1SIM	497658
TT_CT10_TuneZ2star_8TeV-powheg-tauola_Summer12_DR53X-PU_S10_START53_V7A-v2SIM	21675970
TTWJets_8TeV-madgraph_Summer12_DR53X-PU_S10_START53_V7A-v1SIM	217820
TTWWJets_8TeV-madgraph_Summer12_DR53X-PU_S10_START53_V7A-v1SIM	217820
TTZJets_8TeV-madgraph_v2_Summer12_DR53X-PU_S10_START53_V7A-v1SIM	210160

Monte Carlo Samples	N_{Events}
WJetsToLNu_TuneZ2Star_8TeV-madgraph-tarball_Summer12_DR53X-PU_S10_START53_V7A-v2SIM	57709905
WGstarToLNu2Mu_TuneZ2star_7TeV-madgraph-tauola_Summer12_DR53X-PU_S10_START53_V7A-v1SIM	299973
WWJetsTo2L2Nu_TuneZ2star_8TeV-madgraph-tauola_Summer12_DR53X-PU_S10_START53_V7A-v1SIM	1933235
WZJetsTo2L2Q_TuneZ2star_8TeV-madgraph-tauola_Summer12_DR53X-PU_S10_START53_V7A-v1SIM	3215990
WZJetsTo3LNu_TuneZ2_8TeV-madgraph-tauola_Summer12_DR53X-PU_S10_START53_V7A-v1SIM	2017979
WZJetsTo2QLNu_8TeV-madgraph_Summer12_DR53X-PU_S10_START53_V7C-v1SIM	2908657
ZZJetsTo2L2Nu_TuneZ2star_8TeV-madgraph-tauola_Summer12_DR53X-PU_S10_START53_V7A-v3SIM	954911
ZZJetsTo2L2Q_TuneZ2star_8TeV-madgraph-tauola_Summer12_DR53X-PU_S10_START53_V7A-v1SIM	1936727
ZZJetsTo4L_TuneZ2star_8TeV-madgraph-tauola_Summer12_DR53X-PU_S10_START53_V7A-v1SIM	4787893
WWWJets_8TeV-madgraph_Summer12_DR53X-PU_S10_START53_V7A-v1SIM	220549
WWZNoGstarJets_8TeV-madgraph_Summer12_DR53X-PU_S10_START53_V7A-v1SIM	222234
WZZNoGstarJets_8TeV-madgraph_Summer12_DR53X-PU_S10_START53_V7A-v1SIM	219835
ZZZNoGstarJets_8TeV-madgraph_Summer12_DR53X-PU_S10_START53_V7A-v1SIM	224904
WmWmqq_8TeV-madgraph_Summer12_DR53X-PU_S10_START53_V7A-v1SIM	96392
WpWpqq_8TeV-madgraph_Summer12_DR53X-PU_S10_START53_V7A-v1SIM	99985
WW_DoubleScattering_8TeV-pythia8_Summer12_DR53X-PU_S10_START53_V7A-v1SIM	834040
/RPVsmuon_M0-100To2000_M12-100to2500_TuneZ2star_8TeV-calchep-pythia6-tauola/Summer12_DR53X-PU_S10_START53_V19-v1/AODSIM	7140403

Table A.1.: All paths of the Monte Carlo samples that are considered as backgrounds and signals for this analysis. The number of events that remain after skimming are given in the second column.

Bibliography

[1] D. Griffiths. *Introduction to Elementary Particles*. Physics textbook. Wiley, 2008. ISBN: 9783527406012.

[2] Original design by Wikipedia user MissMJ, modified by Crush. *Standard Model of Elementary Particles*. Graphic from Wikipedia article. Nov. 2013.

[3] J. Beringer et al. "Review of Particle Physics", *Phys. Rev. D* 86 (1 July 2012). Includes 2013 partial update for 2014 edition, p. 010001. DOI: 10.1103/PhysRevD.86.010001. URL: http://link.aps.org/doi/10.1103/PhysRevD.86.010001.

[4] Abdus Salam. *Elementary Particle Theory*. ed. N. Svartholm, 1969, p. 367.

[5] Steven Weinberg. "A Model of Leptons", *Phys. Rev. Lett.* 19 (21 Nov. 1967), pp. 1264–1266. DOI: 10.1103/PhysRevLett.19.1264. URL: http://link.aps.org/doi/10.1103/PhysRevLett.19.1264.

[6] Sheldon L. Glashow. "Partial-symmetries of weak interactions", *Nuclear Physics* 22.4 (1961), pp. 579–588. ISSN: 0029-5582. DOI: http://dx.doi.org/10.1016/0029-5582(61)90469-2. URL: http://www.sciencedirect.com/science/article/pii/0029558261904692.

[7] Luis Álvarez-Gaumé and John Ellis. "Eyes on a prize particle", *Nature Physics* 7 (2-3 2011). DOI: 10.1038/nphys1874. URL: http://www.nature.com/nphys/journal/v7/n1/full/nphys1874.html.

[8] F. Englert and R. Brout. "Broken Symmetry and the Mass of Gauge Vector Mesons", *Phys. Rev. Lett.* 13 (9 Aug. 1964), pp. 321–323. DOI: 10.1103/PhysRevLett.13.321. URL: http://link.aps.org/doi/10.1103/PhysRevLett.13.321.

[9] Peter W. Higgs. "Broken Symmetries and the Masses of Gauge Bosons", *Phys. Rev. Lett.* 13 (16 Oct. 1964), pp. 508–509. DOI: 10.1103/PhysRevLett.13.508. URL: http://link.aps.org/doi/10.1103/PhysRevLett.13.508.

[10] Serguei Chatrchyan et al. "Observation of a new boson at a mass of 125 GeV with the CMS experiment at the LHC", *Phys.Lett.* B716 (2012), pp. 30–61. DOI: 10.1016/j.physletb.2012.08.021. arXiv: 1207.7235 [hep-ex].

[11] Serguei Chatrchyan et al. "Study of the Mass and Spin-Parity of the Higgs Boson Candidate Via Its Decays to Z Boson Pairs", *Phys.Rev.Lett.* 110 (2013), p. 081803. DOI: 10.1103/PhysRevLett.110.081803. arXiv: 1212.6639 [hep-ex].

[12] Stephen P. Martin. "A Supersymmetry primer", (1997). arXiv: hep-ph/9709356 [hep-ph].

[13] Herbi K. Dreiner et al. "Baryon triality and neutrino masses from an anomalous flavor U(1)", *Nucl.Phys.* B774 (2007), pp. 127–167. DOI: 10.1016/j.nuclphysb.2007.03.028. arXiv: hep-ph/0610026 [hep-ph].

[14] Herbi K. Dreiner, Christoph Luhn, and Marc Thormeier. "What is the discrete gauge symmetry of the MSSM?", *Phys.Rev.* D73 (2006), p. 075007. DOI: 10.1103/PhysRevD.73.075007. arXiv: hep-ph/0512163 [hep-ph].

[15] P.A.R. Ade et al. "Planck 2013 results. I. Overview of products and scientific results", (2013). arXiv: 1303.5062 [astro-ph.CO].

[16] NASA, CXC, and M. Weiss. "Galaxy cluster 1E 0657-56". Overlay of an optical and x-ray image with a lensing map. Aug. 2006. URL: http://chandra.harvard.edu/photo/2006/1e0657/more.html.

[17] H. Nishino, S. Clark, et al. "Search for Proton Decay via $p \to e^+\pi^0$ and $p \to \mu^+\pi^0$ in a Large Water Cherenkov Detector", *Physical Review Letters* 102.14, 141801 (Apr. 2009), p. 141801. DOI: 10.1103/PhysRevLett.102.141801. arXiv: 0903.0676 [hep-ex].

[18] R. Barbier et al. "R-parity violating supersymmetry", *Phys.Rept.* 420 (2005), pp. 1–202. DOI: 10.1016/j.physrep.2005.08.006. arXiv: hep-ph/0406039 [hep-ph].

[19] Christian Autermann. "Resonant Second Generation Slepton Production at the Tevatron". PhD thesis. RWTH Aachen University, Dec. 2006.

[20] CMS Collaboration. *Search for RPV SUSY resonant second generation slepton production in same-sign dimuon events at sqrt(s) = 7 TeV*. CMS Physics Analysis Summary CMS-PAS-SUS-13-005. Geneva: CERN, 2013.

[21] D0 Collaboration. "Search for Resonant Second Generation Slepton Production at the Fermilab Tevatron", *Phys. Rev. Lett.* 97 (11 Sept. 2006), p. 111801. DOI: 10.1103/PhysRevLett.97.111801.

[22] The ATLAS Collaboration. *Search for long-lived, heavy particles in final states with a muon and a multi-track displaced vertex in proton-proton collisions at sqrt(s) = 8TeV with the ATLAS detector*. ATLAS CONF ATLAS-CONF-2013-092. Geneva: CERN, Aug. 2013.

[23] Lyndon Evans and Philip Bryant. "LHC Machine", *Journal of Instrumentation* 3.08 (2008), S08001. DOI: 10.1088/1748-0221/3/08/S08001. URL: http://stacks.iop.org/1748-0221/3/i=08/a=S08001.

[24] The CMS Collaboration. "CMS Luminosity - Public Results". TWiki Website. Sept. 2013. URL: https://twiki.cern.ch/twiki/bin/view/CMSPublic/LumiPublicResults.

[25] Christiane Lefèvre. "The CERN accelerator complex". Schematic picture of the LHC's injector chain. Dec. 2008.

[26] The ATLAS Collaboration. "The ATLAS Experiment at the CERN Large Hadron Collider", *Journal of Instrumentation* 3.08 (2008), S08003. DOI: 10.1088/1748-0221/3/08/S08003. URL: http://stacks.iop.org/1748-0221/3/i=08/a=S08003.

[27] The CMS Collaboration. "The CMS experiment at the CERN LHC", *Journal of Instrumentation* 3.08 (2008), S08004. DOI: 10.1088/1748-0221/3/08/S08004. URL: http://stacks.iop.org/1748-0221/3/i=08/a=S08004.

[28] The ALICE Collaboration. "The ALICE experiment at the CERN LHC", *Journal of Instrumentation* 3.08 (2008), S08002. DOI: 10.1088/1748-0221/3/08/S08002. URL: http://stacks.iop.org/1748-0221/3/i=08/a=S08002.

[29] The LHCb Collaboration. "The LHCb Detector at the LHC", *Journal of Instrumentation* 3.08 (2008), S08005. DOI: 10.1088/1748-0221/3/08/S08005. URL: http://stacks.iop.org/1748-0221/3/i=08/a=S08005.

[30] *The CMS hadron calorimeter project: Technical Design Report*. Technical Design Report CMS. Geneva: CERN, 1997.

[31] Serguei Chatrchyan, Vardan Khachatryan, Sirunyan, et al. "Performance of CMS muon reconstruction in pp collision events at $\sqrt{s} = 7\,\text{TeV}$", *Journal of Instrumentation* 7.CMS-MUO-10-004, CERN-PH-EP-2012-173 (Oct. 2012), 2P. DOI: 10.1088/1748-0221/7/10/P10002. eprint: 1206.4071.

[32] The CMS collaboration. "The performance of the CMS muon detector in proton-proton collisions at $\sqrt{s} = 7\,\text{TeV}$ at the LHC", *Journal of Instrumentation* 8.CMS-MUO-11-001, CERN-PH-EP-2013-072 (2013), P11002. arXiv: physics.ins-det/1306.6905 [physics.ins-det]. URL: http://stacks.iop.org/1748-0221/8/i=11/a=P11002.

[33] R. Frühwirth. "Application of Kalman filtering to track and vertex fitting", *Nuclear Instruments and Methods in Physics Research Section A: Accelerators, Spectrometers, Detectors and Associated Equipment* 262.2–3 (1987), pp. 444–450. ISSN: 0168-9002. DOI: http://dx.doi.org/10.1016/0168-9002(87)90887-4. URL: http://www.sciencedirect.com/science/article/pii/0168900287908874.

[34] Matteo Cacciari, Gavin P. Salam, and Gregory Soyez. "The anti-k_T jet clustering algorithm", *Journal of High Energy Physics* 2008.04 (2008), p. 063. DOI: http://dx.doi.org/10.1088/1126-6708/2008/04/063. URL: http://stacks.iop.org/1126-6708/2008/i=04/a=063.

[35] S. Baffioni et al. "Electron reconstruction in CMS", *Eur.Phys.J.* C49 (2007), pp. 1099–1116. DOI: 10.1140/epjc/s10052-006-0175-5.

[36] The CMS Collaboration. *Particle-Flow Event Reconstruction in CMS and Performance for Jets, Taus, and MET*. CMS Physics Analysis Summary CMS-PAS-PFT-09-001. 2009. Geneva: CERN, Apr. 2009. URL: http://cds.cern.ch/record/1194487.

[37] A. De Roeck et al. "Supersymmetric benchmarks with non-universal scalar masses or gravitino dark matter", *Eur.Phys.J.* C49 (2007), pp. 1041–1066. DOI: 10.1140/epjc/s10052-006-0182-6. arXiv: hep-ph/0508198 [hep-ph].

[38] The CMS Collaboration. *CMSSW Application Frameework*. TWiki website. 2012. URL: https://twiki.cern.ch/twiki/bin/view/CMSPublic/WorkBookCMSSWFramework.

[39] Carsten Magass et al. *Aachen 3A SUSY Analysis*. TWiki Website. 2011. URL: https://twiki.cern.ch/twiki/bin/viewauth/CMS/Aachen3ASusy.

[40] Rene Brun and Fons Rademakers. "ROOT - An Object Oriented Data Analysis Framework", *Nucl. Inst. & Meth. in Phys. Res.* 389 (1997), pp. 81–86. URL: http://root.cern.ch/.

[41] Martin Weber and Markus Radziej. *findsusyb3 - Aachen 3A Baryon Triality Supersymmetry searches*. TWiki Website. 2013. URL: https://twiki.cern.ch/twiki/bin/view/CMS/Aachen3ARPV.

[42] CMS Collaboration. *CMS Luminosity Based on Pixel Cluster Counting - Summer 2013 Update*. CMS Physics Analysis Summary CMS-PAS-LUM-13-001. Geneva: CERN, 2013.

[43] S. Agostinelli et al. "Geant4—a simulation toolkit", *Nuclear Instruments and Methods in Physics Research Section A: Accelerators, Spectrometers, Detectors and Associated Equipment* 506.3 (2003), pp. 250–303. ISSN: 0168-9002. DOI: http://dx.doi.org/10.1016/S0168-9002(03)01368-8. URL: http://www.sciencedirect.com/science/article/pii/S0168900203013688.

[44] J. Allison et al. "Geant4 developments and applications", *Nuclear Science, IEEE Transactions on* 53.1 (2006), pp. 270–278. ISSN: 0018-9499. DOI: 10.1109/TNS.2006.869826.

[45] Nikolaos Kidonakis. "Differential and total cross sections for top pair and single top production", (2012), pp. 831–834. DOI: 10.3204/DESY-PROC-2012-02/251. arXiv: 1205.3453 [hep-ph].

[46] Piergiulio Lenzi et al. *Standard Model Cross Sections for CMS at 8 TeV*. TWiki Website, retrieved Sep. 2013. URL: https://twiki.cern.ch/twiki/bin/viewauth/CMS/StandardModelCrossSectionsat8TeV.

[47] Torbjörn Sjöstrand, Stephen Mrenna, and Peter Skands. "PYTHIA 6.4 physics and manual", *Journal of High Energy Physics* 2006.05 (2006), p. 026. URL: http://stacks.iop.org/1126-6708/2006/i=05/a=026.

[48] Stefano Frixione, Paolo Nason, and Carlo Oleari. "Matching NLO QCD computations with Parton Shower simulations: the POWHEG method", *JHEP* 0711 (2007), p. 070. DOI: 10.1088/1126-6708/2007/11/070. arXiv: 0709.2092 [hep-ph].

[49] Emanuele Re. "Single-top Wt-channel production matched with parton showers using the POWHEG method", *Eur.Phys.J.* C71 (2011), p. 1547. DOI: 10.1140/epjc/s10052-011-1547-z. arXiv: 1009.2450 [hep-ph].

[50] Simone Alioli et al. "NLO single-top production matched with shower in POWHEG: s- and t-channel contributions", *JHEP* 0909 (2009), p. 111. DOI: 10.1007/JHEP02(2010)011,10.1088/1126-6708/2009/09/111. arXiv: 0907.4076 [hep-ph].

[51] Johan Alwall et al. "MadGraph 5 : Going Beyond", *JHEP* 1106 (2011), p. 128. DOI: 10.1007/JHEP06(2011)128. arXiv: 1106.0522 [hep-ph].

[52] B.C. Allanach. "SOFTSUSY: a program for calculating supersymmetric spectra", *Comput.Phys.Commun.* 143 (2002), pp. 305–331. DOI: 10.1016/S0010-4655(01)00460-X. arXiv: hep-ph/0104145 [hep-ph].

[53] Andreas Gueth and Lars Sonnenschein. *Private Communications*. 2013.

[54] Alexander Belyaev, Neil D. Christensen, and Alexander Pukhov. "CalcHEP 3.4 for collider physics within and beyond the Standard Model", *Comput.Phys.Commun.* 184 (2013), pp. 1729–1769. DOI: 10.1016/j.cpc.2013.01.014. arXiv: 1207.6082 [hep-ph].

[55] H. K. Dreiner et al. "Supersymmetric NLO QCD corrections to resonant slepton production and signals at the Fermilab Tevatron and the CERN LHC", *Phys. Rev. D* 75 (3 Feb. 2007), p. 035003. DOI: 10.1103/PhysRevD.75.035003. URL: http://link.aps.org/doi/10.1103/PhysRevD.75.035003.

[56] Michael Hildreth. *Utilities for Accessing Pileup Information for Data*. TWiki Website. Sept. 2013. URL: https://twiki.cern.ch/twiki/bin/viewauth/CMS/PileupJSONFileforData.

[57] Michael Hildreth. *Pileup Scenarios*. TWiki Website. Sept. 2013. URL: https://twiki.cern.ch/twiki/bin/view/CMS/Pileup_MC_Gen_Scenarios.

[58] Hartmut Stadie and Francesco Pandolfi. *Jet Energy Resolution Measurement*. TWiki Website. Sept. 2013. URL: https://twiki.cern.ch/twiki/bin/view/CMS/JetResolution.

[59] CMS Muon POG. *Baseline muon selections*. TWiki Website. Sept. 2013. URL: https://twiki.cern.ch/twiki/bin/view/CMSPublic/SWGuideMuonId.

[60] CMS Muon POG. *Performance of muon identification in pp collisions at* $\sqrt{s} = 7$ *TeV*. Tech. rep. CMS-PAS-MUO-10-002. 2010. Geneva: CERN, 2010.

[61] M. Mulders et al. "Muon Identification in CMS", *CMS Analysis Notes* (Nov. 2008). URL: http://cms.cern.ch/iCMS/jsp/openfile.jsp?tp=draft&files=AN2008_098_v1.pdf.

[62] CMS JME POG. *JetMET Physics Object Group (JME POG)*. TWiki Webiste. Sept. 2013. URL: https://twiki.cern.ch/twiki/bin/view/CMS/JetMET.

[63] A. Harel and P. Schieferdecker. *Jet Identification*. TWiki Website. Sept. 2013. URL: https://twiki.cern.ch/twiki/bin/viewauth/CMS/JetID.

[64] N. Saoulidou. *Particle Flow Jet Identification Criteria*. Tech. rep. CMS Note AN-2010/003. CERN, 2010.

[65] CMS Egamma POG. *Cut Based Electron ID*. TWiki Website. Sept. 2013. URL: https://twiki.cern.ch/twiki/bin/view/CMS/EgammaCutBasedIdentification.

[66] Kenichi Hatakeyama and Artur Apresyan. Approval Talk. Aug. 2012. URL: https://indico.cern.ch/getFile.py/access?subContId=1&contribId=4&resId=0&materialId=slides&confId=172431.

[67] Piet Verwilligen. *Double Muon Trigger - ReReco Results*. Moun POG Working Meeting. June 2013. URL: https://indico.cern.ch/getFile.py/access?contribId=1&resId=0&materialId=slides&confId=259309.

[68] CMS Muon POG. *Commissioning of the Particle-Flow reconstruction in Minimum-Bias and Jet Events from pp Collisions at 7 TeV*. CMS Physics Analysis Summary CMS-PAS-PFT-10-002. Geneva: CERN, 2010.

[69] Christian Weiser. *A Combined Secondary Vertex Based B-Tagging Algorithm in CMS*. Tech. rep. CMS-NOTE-2006-014. Geneva: CERN, Jan. 2006. URL: http://cds.cern.ch/record/927399.

[70] Thomas Speer et al. *Vertex Fitting in the CMS Tracker*. Tech. rep. CMS-NOTE-2006-032. Geneva: CERN, Feb. 2006. URL: http://cds.cern.ch/record/927395/.

[71] Jyothsna Rani Komaragiri and Victor Bazterra. *Operating Points for b-tagging Algorithms*. TWiki Website. Oct. 2013. URL: https://twiki.cern.ch/twiki/bin/viewauth/CMS/BTagPerformanceOP.

[72] Ulrich Heintz, Meenakshi Narain, and Michael Segala. *Jet-by-jet updating of the b-tagging status*. Method 2a). Oct. 2013. URL: https://twiki.cern.ch/twiki/bin/view/CMS/BTagSFMethods.

[73] CMS BTV POG. *b Tag & Vertexing Physics Object Group*. TWiki Website. Oct. 2013. URL: https://twiki.cern.ch/twiki/bin/viewauth/CMS/BtagPOG.

[74] Thomas Speer. *Jet Flavour identification (MC truth)*. TWiki Website. Oct. 2013. URL: https://twiki.cern.ch/twiki/bin/view/CMSPublic/SWGuideBTagMCTools.

[75] David McKee and Rene Brun. *Kernel Smoothing ROOT implementation*. 2008. URL: http://root.cern.ch/root/html/src/TH2.cxx.html#lD_u6B.

[76] Hartmut Stadie, Mikko Voutilainen, and Henning Kirschenmann. *Jet energy scale uncertainty sources*. TWiki Website. Oct. 2013. URL: https://twiki.cern.ch/twiki/bin/view/CMS/JECUncertaintySources.

[77] Jordan Tucker. *Muon momentum resolution using cosmic muons – update*. Presentation in a Muon POG Meeting. Apr. 2012. URL: https://indico.cern.ch/getFile.py/access?contribId=0&resId=1&materialId=slides&confId=184964.

[78] Carmen Albajar and Isabel Josa. *Muon ID and Iso efficiencies (2012 - 53x rereco)*. Muon POG Meeting. July 2013. URL: https://indico.cern.ch/getFile.py/access?contribId=1&resId=2&materialId=slides&confId=257630.

[79] *CMS Luminosity Based on Pixel Cluster Counting - Summer 2013 Update*. CMS Physics Analysis Summary CMS-PAS-LUM-13-001. Geneva: CERN, 2013.

[80] A.D. Martin et al. "Parton distributions for the LHC", *Eur.Phys.J.* C63 (2009), pp. 189–285. DOI: 10.1140/epjc/s10052-009-1072-5. arXiv: 0901.0002 [hep-ph].

[81] A.D. Martin et al. "Heavy-quark mass dependence in global PDF analyses and 3- and 4-flavour parton distributions", *Eur.Phys.J.* C70 (2010), pp. 51–72. DOI: 10.1140/epjc/s10052-010-1462-8. arXiv: 1007.2624 [hep-ph].

[82] A.D. Martin et al. "Uncertainties on alpha(S) in global PDF analyses and implications for predicted hadronic cross sections", *Eur.Phys.J.* C64 (2009), pp. 653–680. DOI: 10.1140/epjc/s10052-009-1164-2. arXiv: 0905.3531 [hep-ph].

[83] Hung-Liang Lai et al. "New parton distributions for collider physics", *Phys.Rev.* D82 (2010), p. 074024. DOI: 10.1103/PhysRevD.82.074024. arXiv: 1007.2241 [hep-ph].

[84] Richard D. Ball et al. "Unbiased global determination of parton distributions and their uncertainties at NNLO and at LO", *Nucl.Phys.* B855 (2012), pp. 153–221. DOI: 10.1016/j.nuclphysb.2011.09.024. arXiv: 1107.2652 [hep-ph].

[85] Simone Lionetti et al. "Precision determination of α_s using an unbiased global NLO parton set", *Phys.Lett.* B701 (2011), pp. 346–352. DOI: 10.1016/j.physletb.2011.05.071. arXiv: 1103.2369 [hep-ph].

[86] Alessandro Vicini. *Practical implementation of the PDF4LHC recipe*. URL: http://www.hep.ucl.ac.uk/pdf4lhc/PDF4LHC_practical_guide.pdf.

[87] PDF4LHC Working Group. *PDF4LHC Recommendations*. URL: http://www.hep.ucl.ac.uk/pdf4lhc/PDF4LHCrecom.pdf.

[88] J. Pumplin et al. "New generation of parton distributions with uncertainties from global QCD analysis", *JHEP* 0207 (2002), p. 012. arXiv: hep-ph/0201195 [hep-ph].

[89] Micheal Hildreth. *Estimating Systematic Errors Due to Pileup Modeling*. TWiki Website. Nov. 2013. URL: https://twiki.cern.ch/twiki/bin/view/CMS/PileupSystematicErrors.

[90] Daniel F. Teyssier. *Private Communications*. 2014.

[91] A. L. Read. "Modified frequentist analysis of search results (the CL_s method)", *1st Workshop on Confidence Limits, CERN, Geneva* CERN-OPEN-2000-205j (Jan. 2000), pp. 81–101.

[92] A. L. Read. "Presentation of search results: the CL s technique", *Journal of Physics G: Nuclear and Particle Physics* 28.10 (2002), p. 2693. URL: http://stacks.iop.org/0954-3899/28/i=10/a=313.

[93] *Procedure for the LHC Higgs boson search combination in Summer 2011*. Tech. rep. CMS-NOTE-2011-005. ATL-PHYS-PUB-2011-11. Geneva: CERN, Aug. 2011.

[94] Giovanni Petrucciani. *Documentation of the RooStats-based statistics tools for Higgs PAG*. TWiki Website. Nov. 2013. URL: https://twiki.cern.ch/twiki/bin/viewauth/CMS/SWGuideHiggsAnalysisCombinedLimit.

[95] Kyle Cranmer et al. *HistFactory: A tool for creating statistical models for use with RooFit and RooStats*. Tech. rep. CERN-OPEN-2012-016. New York: New York U., Jan. 2012.